

# Transformation of Biological Networks into Images via Semantic Cartography for Visual Interpretation and Scalable Deep Analysis

**Sakib Mostafa<sup>1</sup>, Lei Xing<sup>1,\*</sup>, and Md Tauhidul Islam<sup>1,\*</sup>**

<sup>1</sup>Department of Radiation Oncology, Stanford University, Stanford, CA, USA

\*Correspondence: tauhid@stanford.edu, lei@stanford.edu

## ABSTRACT

Complex biological networks are fundamental to biomedical science, capturing interactions among molecules, cells, genes, and tissues. Deciphering these networks is critical for understanding health and disease, yet their scale and complexity represent a daunting challenge for current computational methods. Traditional biological network analysis methods, including deep learning approaches, while powerful, face inherent challenges such as limited scalability, oversmoothing long-range dependencies, difficulty in multimodal integration, expressivity bounds, and poor interpretability. We present Graph2Image, a framework that transforms large biological networks into sets of two-dimensional images by spatially arranging representative network nodes on a 2D grid. This transformation decouples the nodes as images, enabling the use of convolutional neural networks (CNNs) with global receptive fields and multi-scale pyramids, thus overcoming limitations of existing biological network analysis methods in scalability, memory efficiency, and long-range context capture. Graph2Image also facilitates seamless integration with other imaging and omics modalities and enhances interpretability through direct visualization of node-associated images. When applied to several large-scale biological network datasets, Graph2Image improved classification accuracy by up to 67.2% over existing methods and provided interpretable visualizations that revealed biologically coherent patterns. It also allows analysis of very large biological networks (nodes > 1 billion) on a personal computer. Graph2Image thus provides a scalable, interpretable, and multimodal-ready approach for biological network analysis, offering new opportunities for disease diagnosis and the study of complex biological systems.

## 1 Introduction

Complex biological networks are inherent components of biomedical science, representing the vast web of interactions among molecules, cells, genes, and tissues. Fundamentally, a biological network/graph consists of a set of nodes and the connections between them, known as edges, which represent the node-node relationships. From protein-protein interaction networks that orchestrate cellular function<sup>1,2</sup> and gene regulatory networks that guide cellular developmental processes<sup>3</sup>, to the immense architecture of neurons and their synaptic connections in the brain<sup>4,5</sup>, these biological graph-based models are critical for representing the mechanisms of health and disease<sup>6,7</sup>. Their applications are vast, spanning metabolic pathways that govern cellular energy<sup>8</sup>, microbial interaction networks within the microbiome that influence host health<sup>9</sup>, and epidemiological networks that model the spread of infectious diseases<sup>10</sup>. Even entire ecosystems can be understood through the structure of their food webs<sup>11</sup>. The ability to analyze these diverse and complex biological networks is therefore a prerequisite for advancing our understanding of biological systems<sup>12,13</sup>, identifying therapeutic targets in drug discovery<sup>14–16</sup>, and developing new diagnostic strategies<sup>17,18</sup>.

The advancement of high-throughput technologies such as single-cell RNA-seq, spatial transcriptomics, proteomics, and metabolomics has led to an explosion in the scale of biomedical data, generating biological networks of unprecedented size and complexity<sup>19</sup>. These biological graphs often contain hundreds of thousands to millions of nodes, accompanied by an even larger number of edges<sup>20</sup>. Analyzing data at this scale poses formidable challenges: the computational and memory demands of processing such massive biological graphs can exceed the capabilities of even state-of-the-art hardware<sup>21</sup>. As a result, these resource constraints create a critical bottleneck that impedes the translation of large-scale biological data into meaningful and actionable insights<sup>22</sup>.

To address the challenge of analyzing these large-scale biological networks, many analytical techniques and, more recently, deep learning models have been proposed. The analytical methods primarily rely on handcrafted features derived from graph theory for representing the data. These methods include spectral approaches that use the graph Laplacian for community detection<sup>23–25</sup>, and kernel-based methods that measure similarity by counting predefined substructures like random walks, shortest paths, or graphlets<sup>26–29</sup>. While useful for certain tasks, these techniques are often simple and may fail to capture the

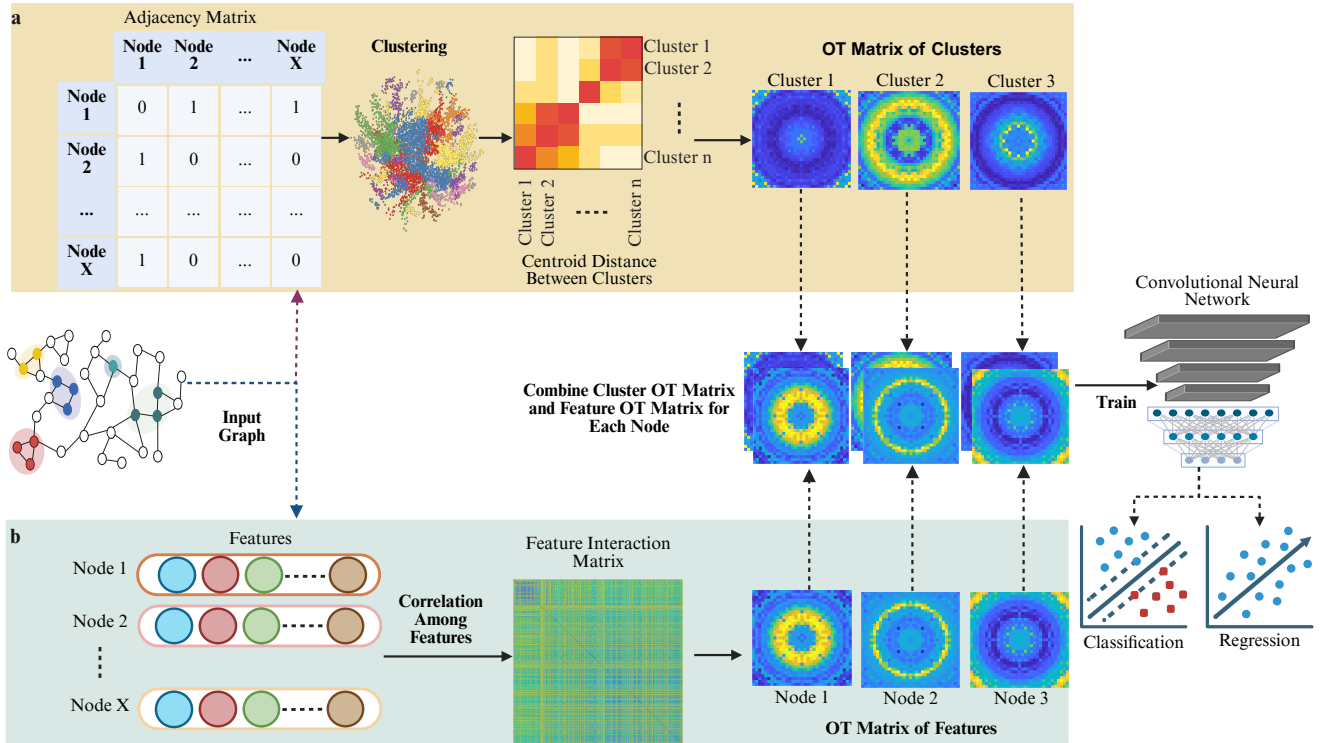


**Figure 1.** The Graph2Image framework for transforming attributed graphs into multi-channel images. The pipeline learns in two parallel paths. **a**, The structural path learns the graph's topology. It takes the Adjacency Matrix, uses **Clustering** to find communities, and maps the centroid distance between clusters on a 2D grid using the **Optimal Transport (OT)** algorithm to create a structural image. **b**, The feature path learns node feature relationships. It calculates a feature interaction matrix based on the **Correlation Among Features** and maps the features on a 2D grid using a different Optimal Transport algorithm to generate feature images. These two images are then combined into a final, multi-channel image for each node. This set of images is used to train a Convolutional Neural Network for downstream tasks like Classification and Regression.

complex, non-linear patterns inherent in biological data.

To overcome the reliance on engineered features, deep learning methods, specifically, Graph Neural Networks (GNN) have emerged as the dominant paradigm, learning node representations directly from biological network topology and node features through a flexible message-passing framework<sup>30–32</sup>. Early GNN models such as Graph Convolutional Networks (GCNs) generalize convolutions to biological graph data by operating in the spectral domain<sup>33,34</sup>. More flexible spatial methods that directly aggregate information from a node's neighbors have also been proposed. Among them, GraphSAGE, which introduce neighbor sampling to achieve scalability for massive biological graphs<sup>35,36</sup>, and Graph Attention Network (GAT), which learn to dynamically weigh the importance of different neighbors are the prominent ones<sup>37,38</sup>. Further advanced models, such as Graph Isomorphism Network (GIN)<sup>39,40</sup>, have been developed to improve the expressive power of GNNs.

There are several fundamental constraints of the existing biological network analysis methods. Classical methods are often limited by rigid mathematical assumptions that may not capture the full complexity of biological data. On the other hand, modern deep learning (DL) based graph analysis methods also have their limitations<sup>41,42</sup>. A primary limitation of the DL methods is scalability, as the recursive message-passing central to GNNs is computationally prohibitive for large biological graphs<sup>35</sup>. This recursive computation can also result in degraded analysis performance for two reasons: 1) oversmoothing, where the repeated averaging of neighbor information causes distinct nodes to become indistinguishable<sup>43</sup>, and 2) oversquashing, where important long-range dependencies are lost as information is compressed through informational bottlenecks<sup>44</sup>. Beyond these performance issues, GNNs are also limited by theoretical expressivity bounds, as they are inherently unable to distinguish certain fundamental graph structures, such as different regular graphs or simple cycles of varying lengths<sup>45,46</sup>. Perhaps most critically for scientific application, their "black box" nature severely limits interpretability, making it difficult to trust their predictions or use them to uncover new biological mechanisms<sup>47–49</sup>.

Here we present Graph2Image, a biological network cartography framework that overcomes these limitations by transforming the biological network analysis problem into an image interpretation task. Our approach reframes a large biological

network as a collection of two-dimensional semantically meaningful images, one for each node (Fig. 1). First, we deconstruct the biological network by clustering it into functional communities. We then employ an optimal transport (OT) algorithm to generate a "map" of these communities, arranging them on a 2D grid such that their spatial proximity reflects their interaction strength in the original network. This process yields a set of images that encode the relational information of the graph in their spatial layout, decoupling the network's complexity and enabling a linearly scalable solution. This transformation allows for the application of a Convolutional Neural Network (CNN) for biological network analysis. By leveraging properties like global receptive fields, CNN is not bound by the same local aggregation constraints as GNNs, offering a solution that is both memory-efficient and adept at capturing long-range context. Furthermore, the image-based representation provides a natural framework for multimodal biological data integration and enhances interpretability through direct visualization.

We demonstrate the efficacy of Graph2Image on a wide range of large-scale, multi-omics cancer datasets, showing that our approach consistently outperforms established GNN-based methods in complex classification tasks. The features learned by our model are biologically meaningful and result in interpretable, actionable insights. We also show that Graph2Image is highly scalable, capable of analyzing massive graphs that are infeasible for traditional GNNs. By providing a scalable, interpretable, and multimodal-ready solution, Graph2Image offers a new paradigm for network analysis, creating new opportunities for disease diagnosis and the study of complex biological systems.

## 2 Results

### 2.1 Graph2Image recovers tissue-of-expression programs in a pathway-derived interactome

To demonstrate the superior performance of the proposed Graph2Image method in comparison to existing approaches, we first analyzed pathway-derived protein–protein interaction networks from the PP-Pathways human interactome, which includes experimentally measured tissue labels<sup>50</sup>. PP-Pathways aggregates physical protein–protein interactions from multiple curated pathway resources into a large, heterogeneous network of human proteins, providing a systems-level view of signaling and metabolic pathways. For each node (gene), we constructed features from GTEx v8 bulk RNA-seq by averaging the Transcripts Per Million (TPM) across samples from the same tissue<sup>51,52</sup>. We then assigned a biologically interpretable label by taking the tissue in which that gene had the highest mean expression across the 54 GTEx tissues, yielding a 54-class tissue-of-expression prediction task (Table S1)<sup>51,53</sup>. We highlight eight well-sampled and physiologically distinct tissues, i.e., subcutaneous and visceral adipose tissue, adrenal gland, aorta, coronary and tibial arteries, small intestine (terminal ileum), and breast mammary tissue, in the SHAP heatmap and reduced confusion matrix in Fig. 2a,b, while the model is trained and evaluated on all 54 tissues (full confusion matrix in Supplementary Fig. S2; see also Supplementary Table S1 for class names, and Fig. S1 for class distribution)<sup>52</sup>. These tissues collectively span key cardiometabolic and endocrine axes: adipose depots act as metabolically active endocrine organs that secrete adipokines and regulate systemic energy balance<sup>54,55</sup>, the adrenal gland produces corticosteroids and catecholamines that coordinate stress and metabolic responses<sup>56</sup>, large arteries and coronary vessels represent central and peripheral components of the cardiovascular system<sup>57,58</sup>, the terminal ileum is a major site of nutrient and bile acid absorption<sup>59,60</sup>, and the mammary gland contains secretory epithelium specialized for milk production during lactation<sup>61,62</sup>.

As seen in Fig. 2c–e, Graph2Image achieved substantially higher classification performance on this 54-way tissue-of-expression task than all GNN baselines. Across accuracy, macro F1-score, precision, and recall, Graph2Image consistently outperformed GAT, GCN, GIN, and GraphSAGE by large margins. For example, Graph2Image reached an accuracy of 83.2% and a macro F1-score of 65.3% when distinguishing all 54 tissues, whereas the best-performing GNN baseline (GraphSAGE) reached 45.3% accuracy and 16.2% macro F1. The precision–recall and ROC curves in Fig. 2c,d further highlight this gap: the Graph2Image curves dominate those of all GNNs across almost the entire range of recall and false-positive rates, indicating more reliable decision boundaries for both high-precision and high-recall operating points. The confusion matrix for Graph2Image predictions in Fig. 2b shows a strong diagonal structure with only modest off-diagonal mass (full 54-tissue confusion matrix in Supplementary Fig. S4), suggesting that misclassifications are relatively rare and are largely concentrated between closely related tissues such as subcutaneous vs visceral adipose or between different arterial beds, which are known to share overlapping vascular gene-expression programs<sup>51,57</sup>.

Furthermore, as shown in Fig. 2a, we used SHapley Additive exPlanations (SHAP) on the node images to understand which tissue features drive each class decision. This stands in contrast to GNNs, where applying attribution methods remains a significant challenge<sup>48</sup>. While GNN-specific approaches like GNNExplainer have been developed, formally adapting principled methods like SHAP to the graph domain is an active and complex area of research, often requiring specialized approximations to remain computationally feasible<sup>48,63,64</sup>. In this setting, SHAP operates on the tissue-expression channel of the Graph2Image representation and yields per-tissue contribution scores for every gene<sup>65–67</sup>. For each class (dominant tissue-of-expression), Graph2Image learns a compact set of tissue features with high positive SHAP values that closely match the GTEx label definition (see Supplementary Fig. S3). Subcutaneous and visceral adipose genes are predominantly supported by their respective adipose tissue features, with secondary support from each other, consistent with the view that these depots share core

adipocyte programs but differ in inflammatory and endocrine signatures<sup>54,55</sup>. Artery-labeled genes (aorta, coronary, tibial) show the strongest SHAP contributions from the corresponding arterial tissues, again with cross-support among arterial beds, mirroring the shared smooth-muscle and endothelial expression programs that underpin systemic vascular function<sup>51,57</sup>. Genes whose dominant expression lies in the adrenal gland or terminal ileum are primarily driven by their matching tissues, reflecting the specialized endocrine role of the adrenal cortex and medulla in hormone production<sup>56,68</sup> and the role of the distal small intestine in nutrient and bile acid absorption<sup>59,60,69</sup>. Finally, breast mammary tissue genes are most strongly influenced by the mammary feature, consistent with the highly specialized transcriptional program of mammary epithelial cells for milk synthesis and secretion<sup>61,62</sup>.

To examine the broader structure of these feature contributions, we aggregated SHAP scores across all 54 GTEx tissues and performed hierarchical clustering on tissues and classes. The tissue-level dendrogram (Supplementary Fig. S4) reveals modules that closely track known organ systems from transcriptomic and proteomic atlases<sup>51,53</sup>: multiple brain regions cluster together, gastrointestinal tissues (stomach, small intestine, colon) form a coherent group, arterial tissues and heart chambers cluster along a cardiovascular branch, and adipose depots and the mammary gland are placed in close proximity, consistent with their shared involvement in lipid storage, endocrine signaling, and secretory function<sup>54,62,69</sup>. The SHAP clustermap of classes and tissues in supplementary Figs. S4, S5 further shows that genes assigned to different adipose depots, arteries, and gut tissues share partially overlapping but distinct SHAP profiles, capturing both shared pathway usage and tissue-specific refinements. Class-level hierarchical clustering based on SHAP profiles (Supplementary Fig. S5) yields a similar organization, separating vascular, adipose/endocrine, and neural modules in a manner that aligns with system-level patterns seen in GTEx and the Human Protein Atlas<sup>51,53</sup>. Together, these analyses indicate that Graph2Image not only predicts the dominant tissue-of-expression with high accuracy but also organizes proteins in a feature-importance space that recapitulates major physiological systems and their relationships across the human interactome.

## 2.2 Graph2Image recapitulates tissue programs in the HuRI human interactome

Next, to show the superior capability of Graph2Image compared to existing methods to recover physiologically meaningful tissue programs directly from a protein–protein interaction network, we analyzed the Human Reference Interactome (HuRI) annotated with GTEx v8 tissue expression. In this setting, nodes represent genes and edges correspond to experimentally supported human protein–protein interactions from HuRI<sup>70</sup>, and each node is associated with a GTEx gene expression profile across diverse normal tissues<sup>71,72</sup>. We assigned each gene a real biological label equal to its primary GTEx tissue of expression, defined as the tissue with maximal mean TPM across donors<sup>71,72</sup>, and restricted the analysis to nine tissues with sufficient support: whole blood, brain-cerebellum, brain-cerebellar hemisphere, skeletal muscle, thyroid, ovary, testis, EBV-transformed lymphoblastoid cell lines (EBV-LCLs), and cultured fibroblasts. These tissues span major physiological systems-hematopoietic and immune (blood and EBV-LCLs), neuronal (brain regions), contractile muscle, endocrine (thyroid), reproductive (ovary and testis) and stromal/mesenchymal compartments (fibroblasts)<sup>53,73,74</sup>. Graph2Image was trained to predict these tissue labels from two-channel images that jointly encode network structure and tissue expression, and we compared its performance against four GNN baselines (GAT, GCN, GIN and GraphSAGE) trained on the same HuRI graph.

As seen in Fig. 3e, Graph2Image achieved a classification accuracy of 90.5% and a macro F1-score of 84.5%, substantially outperforming all GNN baselines. The best-performing GNN, GraphSAGE, reached 75.4% accuracy and 65.0% macro F1, while GAT, GCN and GIN performed markedly worse, particularly on minority tissues. Consistent with these summary metrics, the precision–recall and ROC curves in Fig. 3c show that Graph2Image dominates the baselines across operating thresholds (see also Supplementary Fig. S11). The confusion matrix of Graph2Image predictions in Fig. 3d exhibits a strong diagonal structure with only limited off-diagonal mass (see Supplementary Fig. S7 for a detailed confusion matrix), and the remaining errors occur mainly between closely related brain regions or between immune compartments such as whole blood and EBV-LCLs, which are known to share overlapping transcriptional programs and lineage relationships in the hematopoietic system<sup>53,71,74,75</sup>.

To understand what Graph2Image learns from the HuRI interactome and how it uses tissue expression to make predictions, we applied SHAP to the node images, mapping pixel attributions back to GTEx tissues via the optimal-transport–derived layout. The resulting SHAP profiles reveal that Graph2Image has organized the HuRI genes along a set of physiologically meaningful tissue axes that match known systems biology<sup>53,71</sup>. The radial SHAP map in Fig. 3a shows that each primary tissue class is dominated by its corresponding GTEx tissue feature: whole blood for blood-labeled genes, skeletal muscle for muscle-labeled genes, and so on, consistent with the strong tissue specificity observed in GTEx and related atlases<sup>53,71,72</sup> (see Supplementary Fig. S9). At the same time, the model exploits systematic combinations of tissues rather than relying on single features. As shown in Fig. 3a (see Supplementary Figs. S9 for detailed SHAP heatmap), for genes whose primary label is whole blood, SHAP assigns high positive importance not only to whole blood but also to spleen and EBV-LCLs, reflecting the shared hematopoietic and immune origin of circulating blood cells, splenic immune populations, and EBV-transformed B lymphoblastoid cell lines<sup>74–76</sup>. Thyroid-labeled genes are supported by the thyroid feature together with minor salivary gland, ovary, and cortical brain regions, in line with reports that epithelial cells of the salivary gland and thyroid share immune and

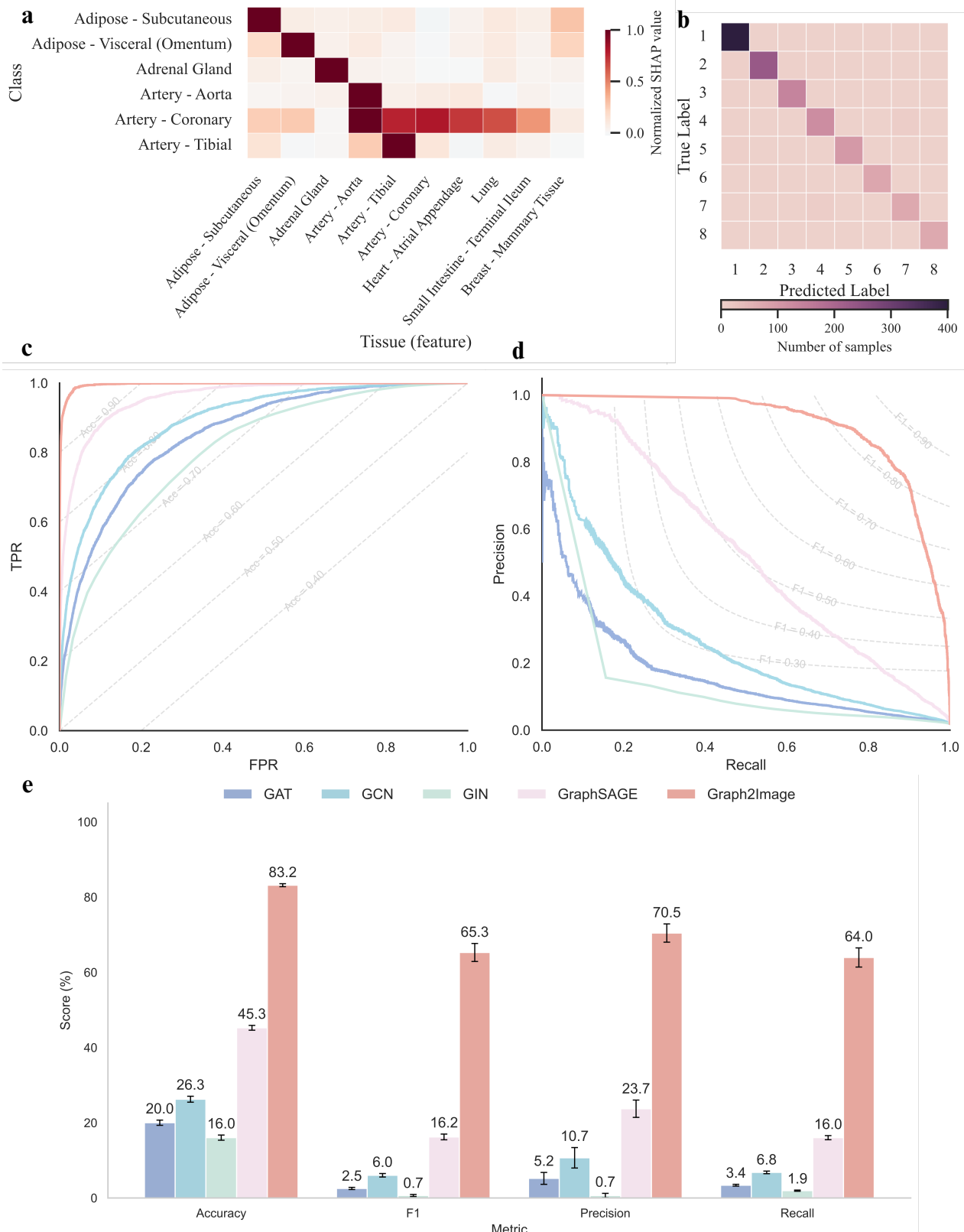


**Figure 2.** Performance and tissue-level interpretability on the PP-Pathways dataset. **a**, Class-averaged SHAP heatmap showing normalized contributions of selected GTEx tissues (features) to Graph2Image predictions for eight dominant-tissue classes (rows). **b**, Confusion matrix of Graph2Image predictions across the eight tissue classes (counts per cell). **c**, Macro-averaged ROC curves comparing Graph2Image with GNN baselines (GAT, GCN, GIN and GraphSAGE). **d**, Macro-averaged precision-recall curves for the same methods. **e**, Summary comparison of Accuracy, macro F1, Precision and Recall between Graph2Image and the GNN baselines. See Supplementary Figs. S2, S3, S4, and S5 for the full 54-tissue confusion matrix, SHAP clustermap, tissue-level SHAP dendograms, and class dendrogram.

antigen-presentation programs and that thyroid and reproductive tissues participate in common endocrine and autoimmune axes<sup>77–80</sup>. Genes labeled as ovary show strong SHAP contributions from ovary, cervix (ectocervix) and fallopian tube, capturing a coordinated female reproductive-tract program in which gene expression is shared across these tissues<sup>81–83</sup>. Testis-labeled genes receive additional support from the ovary, cerebellar tissues, and immune features, consistent with the tight coupling between the male reproductive tract and the immune system and the immune-privileged status of the testis<sup>84,85</sup>, as well as the broader endocrine and neuroendocrine crosstalk between gonadal and brain tissues<sup>53,72</sup>.

The chord diagram in Fig. 3b summarizes these relationships by linking each class to its most influential GTEx tissues. Brain-associated classes (cerebellum and cerebellar hemisphere) are predominantly connected to brain tissues, including cortex, frontal and cingulate cortex, and cerebellar regions, highlighting a coherent central nervous system module<sup>53,71</sup>. Muscle-labeled genes are anchored by skeletal muscle but also connect strongly to fibroblasts and vascular or immune tissues, consistent with the well-established role of fibroblasts and immune cells in providing stromal, vascular, and inflammatory support within muscle and other tissues<sup>73,76</sup>. Across classes, fibroblasts and lymphocyte-related features (EBV-LCL and whole blood) appear as recurrent high-SHAP channels, suggesting that Graph2Image uses a broadly expressed stromal and immune backbone as a reference frame against which more specialized tissue signatures are contrasted<sup>71,73,76</sup>.

To formally quantify this structure, we performed hierarchical clustering on the tissue-level SHAP profiles as shown in Supplementary Fig. S8. The tissue dendrogram groups central nervous system tissues together, clusters blood, spleen, and lymphocyte-derived samples into an immune super-group, and places muscle, fibroblast-rich, and epithelial/endocrine tissues into interconnected stromal and organ-specific branches<sup>53,71</sup>. A complementary SHAP clustermap in Supplementary Fig. S9 and class-level dendrogram in Supplementary Fig. S10 reveal that classes sharing similar SHAP signatures, e.g., the two cerebellar labels or the reproductive tissues, cluster closely in this importance space<sup>53,71,81,82</sup>. Thus, the HuRI analysis shows that Graph2Image not only achieves superior predictive performance on a realistic tissue-of-expression task, but also learns a structured, interpretable representation in which major tissue systems and their relationships emerge directly from the interactome.

### 2.3 Graph2Image accurately classifies diverse cell types in a whole-organism atlas

To demonstrate that our approach can analyze complex, large-scale biological systems with better accuracy and computational efficiency than existing methods, we applied Graph2Image to the Tabula Muris single-cell RNA-sequencing dataset. The resulting graph from the data comprises 54,864 nodes representing cells and over 3 billion edges, a scale that is intractable for standard GNNs. To create a manageable baseline, we were required to threshold the graph and reduce the number of edges by over 99% to approximately 5.1 million. The task was to classify the nodes representing single cells into 55 different cell types (See Fig. S1c for class distribution). As seen in Fig. 4d, compared to existing methods, Graph2Image, demonstrated a substantial improvement. Note that Graph2Image could operate on the complete graph, whereas the existing methods could be only applied on downsampled graphs. Graph2Image achieved a classification accuracy of 97.4% and a macro F1-score of 89.8%, significantly outperforming all benchmark GNNs by at least 4.3%. These classification results are also shown using the confusion matrix in Fig. 4b (for detailed confusion matrix see Fig. S12), where we can see a strong diagonal concentration, indicating minimal misclassification even among closely related cell types.

Beyond these summary metrics, inspection of the Graph2Image outputs confirms that the transformation produces class-specific visual signatures. From Fig. 4c we can see that all Alveolar Macrophages are mapped to images with a highly consistent textural pattern, whereas Epithelial Cells give rise to a clearly distinct pattern. Within each cell type, node-specific images are visually similar across samples, but between cell types they differ markedly in both the structural and feature channels, indicating that the learned spatial organization of the images reflects underlying cellular identity rather than an arbitrary encoding.

To show that our approach is more interpretable and to reveal the biological principles learned by the model, we used SHAP to quantify the contribution of each gene to the classification of each cell type on the constructed node images. Leveraging the straightforward applicability of SHAP to our framework, in Fig. 4a we found that the model learned a set of biologically meaningful gene expression signatures that correctly recapitulate the fundamental principles of cell lineage and identity (see Fig. S14 for a detailed heatmap). The most prominent clusters found in our study correspond to hematopoietic, epithelial, and mesenchymal lineages. The hematopoietic cluster, for instance, is known to have a high level of expression of PTPRC (encoding the pan-leukocyte marker CD45)<sup>86</sup>. Within this hematopoietic group, the model precisely recapitulated the fundamental lymphoid-myeloid dichotomy. Our SHAP analysis revealed that this was achieved by learning two distinct and opposing gene signatures that defined the two lineages. The B-cell lineage is shown to have high positive SHAP values for Vpreb3, Cd79a, and Cd79b, genes encoding critical components of the B-cell receptor complex<sup>87</sup>. Moreover, T-cells have higher SHAP values of hallmark genes like Cd3g, a subunit of the T-cell receptor<sup>88</sup>. The myeloid lineage is characterized by a distinct gene expression signature, which includes key markers such as Lyz1 for monocytes and Mpo for granulocytes<sup>89</sup>. The model also identified key regulators, such as the transcription factor Irf8, which showed high importance for dendritic cells and monocytes,

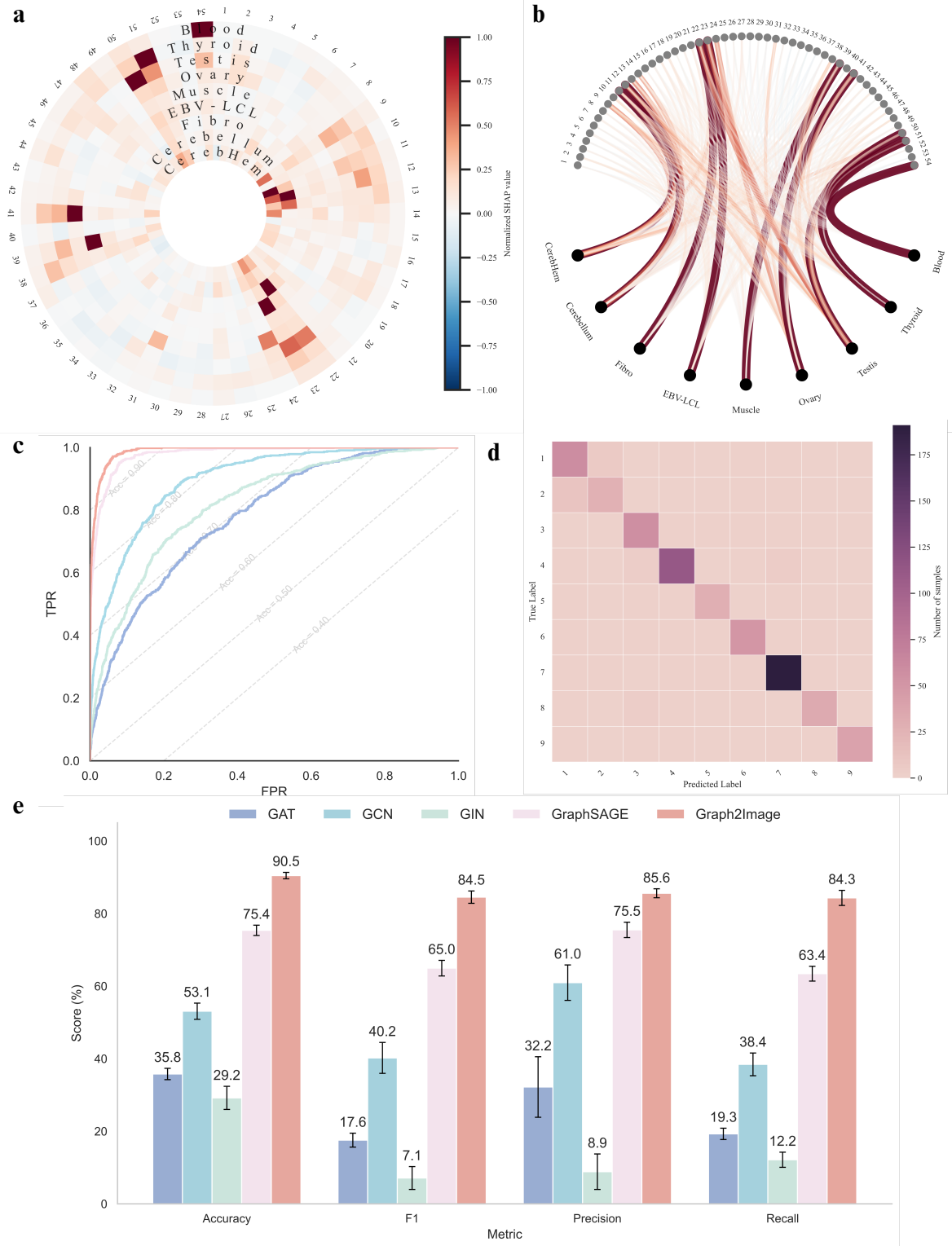


**Figure 3.** Performance and interpretability of Graph2Image on the HuRI + GTEx dataset. **a**, Radial SHAP map summarizing normalized SHAP values for each GTEx tissue feature across the nine primary tissue classes; concentric rings correspond to classes and angular positions to tissues. **b**, SHAP chord diagram highlighting the strongest positive links between tissue classes (bottom) and influential GTEx tissue features (top), illustrating shared and class-specific programs. **c**, Receiver operating characteristic (ROC) curves for Graph2Image and GNN baselines (GAT, GCN, GIN, GraphSAGE) in the nine-way tissue classification task. **d**, Confusion matrix of Graph2Image predictions across the nine primary tissues (counts in linear scale). **e**, Classification comparison (Accuracy, macro F1, macro Precision, macro Recall) between Graph2Image and GNN baselines; bars show mean scores with bootstrap confidence intervals. See Supplementary Figs. S7, S9, S8, and S10 for the full confusion matrix, SHAP clustermaps, and dendrograms.

consistent with its known role in myeloid development<sup>90</sup>. The model also robustly learned the distinction between epithelial and mesenchymal cells. The expression of Epcam, a classic epithelial adhesion molecule, was a powerful positive feature for epithelial cells<sup>91</sup>, while its absence was key for identifying mesenchymal cells like fibroblasts, which were instead defined by markers such as Vim (Vimentin)<sup>92</sup>.

Finally, the analysis highlights the model's ability to identify highly specific biomarkers for terminally differentiated cell types. The most striking example is the gene Alb (Albumin), whose expression was learned as an overwhelmingly powerful and exclusive positive predictor for hepatocytes, reflecting its primary role as the main protein produced by the liver<sup>93</sup>. Similarly, the model correctly identified Sftpc (Surfactant Protein C) as the definitive marker for type II pneumocytes, essential for lung function<sup>94</sup>. To formally assess this learned structure, we performed hierarchical clustering on the cell types based on their SHAP score profiles. The resulting dendrogram in Fig. S13 reveals a clear, high-level separation of major cell lineages that closely mirrors known developmental biology, demonstrating that the model's feature importance space is structured to reflect both broad, lineage-defining gene programs and the highly specific biomarkers that define terminal cell fates.

## 2.4 Multi-omic analysis in pan-cancer classification reveals diverse molecular drivers

To evaluate the ability of Graph2Image to integrate large-scale multi-omic profiles in a clinically heterogeneous setting, we applied it to the TCGA pan-cancer network, comprising 8,314 nodes connected by over 69 million edges. Whereas standard GNN baselines were only computationally manageable after aggressive edge down-sampling to 3.2 million edges, Graph2Image operated directly on the complete, unfiltered graph.

The task was to classify nodes into 32 distinct cancer types (see Fig. S1d for class distribution). As seen from Fig. 5e, our model again demonstrated superior performance. It achieved 96.9% accuracy and an F1-score of 91.7%. Our technique significantly outperformed the next-best GNN models (by 2.8% in accuracy and 2.9% in F1-score), which were trained on the sparse graph. These classification results are also depicted using the confusion matrix in Fig. 5c and Fig. S15. The matrix shows a strong diagonal concentration, indicating minimal misclassification even among histologically similar cancer types like Colon (COAD) and Rectal Adenocarcinoma (READ) (see Supplementary Table S8 for full name of the cancer type abbreviations).

To reveal the biological principles learned by our model, we used SHAP to analyze the most impactful mRNA features. We visualize these SHAP scores as a clustered heatmap in Fig. 5b (see Supplementary Fig. S16 for detailed heatmap). From Fig. 5b, we observe that the model's decisions are driven by distinct and biologically coherent gene signatures. The model's interpretability also extends to uncovering the biological relationships between the cancer types. To demonstrate this, we performed hierarchical clustering on the 32 cancers using their learned mRNA SHAP score profiles (Fig. S18). This analysis revealed that the model automatically grouped cancers according to their known developmental origins without any prior information. For example, the heatmap clearly shows a prominent cluster of all squamous cell carcinomas (HNSC, LUSC, CESC), which the model identified using a shared set of predictive genes. Similarly, the clustering correctly grouped cancers of neuroendocrine origin (PCPG, THYM) and gastrointestinal adenocarcinomas (COAD, READ, STAD). The resulting similarity relationships align well with established cancer phylogeny and tissue-of-origin patterns<sup>95</sup>.

In Fig. 5a we show that our framework can also deconstruct the contributions of different molecular modalities. We aggregated the total SHAP importance from all three omic layers, i.e., mRNA, copy number variation (CNV), and DNA methylation. This allowed us to quantify the relative contribution of each modality to the classification decisions (see Fig. S17 for detailed contribution map). This analysis reveals that the model learned to prioritize different modalities for different cancer types, reflecting their diverse biology. For example, mRNA expression was the dominant factor for cancers with a strong lineage-specific identity. The predictions for Liver Hepatocellular Carcinoma (LIHC), Prostate Adenocarcinoma (PRAD), and Thyroid Carcinoma (THCA) were almost entirely dependent on tissue-defining genes like ALB, KLK3 (PSA), and TG, respectively. In contrast, the model identified CNV as a major factor for cancers known for genomic instability. The classification of Ovarian Cancer (OV) and Uterine Carcinosarcoma (UCS) showed a high reliance on CNV features. This aligns with the known prevalence of gene amplifications and deletions in these diseases<sup>96</sup>. Furthermore, the model identified DNA methylation as a critical predictive layer for specific cancer types. As an example, the classification of Low-Grade Glioma (LGG) showed a substantial contribution from methylation features. This finding reflects the central role of the CpG Island Methylator Phenotype (G-CIMP), which is a defining characteristic of a major LGG subtype and is strongly associated with IDH1 mutations<sup>97</sup>.

Consistent with these modality-specific attributions, Graph2Image examples from the pan-cancer cohort display reproducible, class-specific visual patterns in Fig. 5d. Tumors of the same type give rise to highly similar multi-channel images, whereas tumors from different types exhibit noticeable differences in both the structural and feature channels. For instance, ACC and KIRC images show distinct arrangements of concentrated, ring-like signals versus more diffuse textures across channels, reflecting their divergent molecular architectures. This visual separability highlights that the Graph2Image representation encodes cancer-type-specific structure rather than arbitrary pixel patterns.

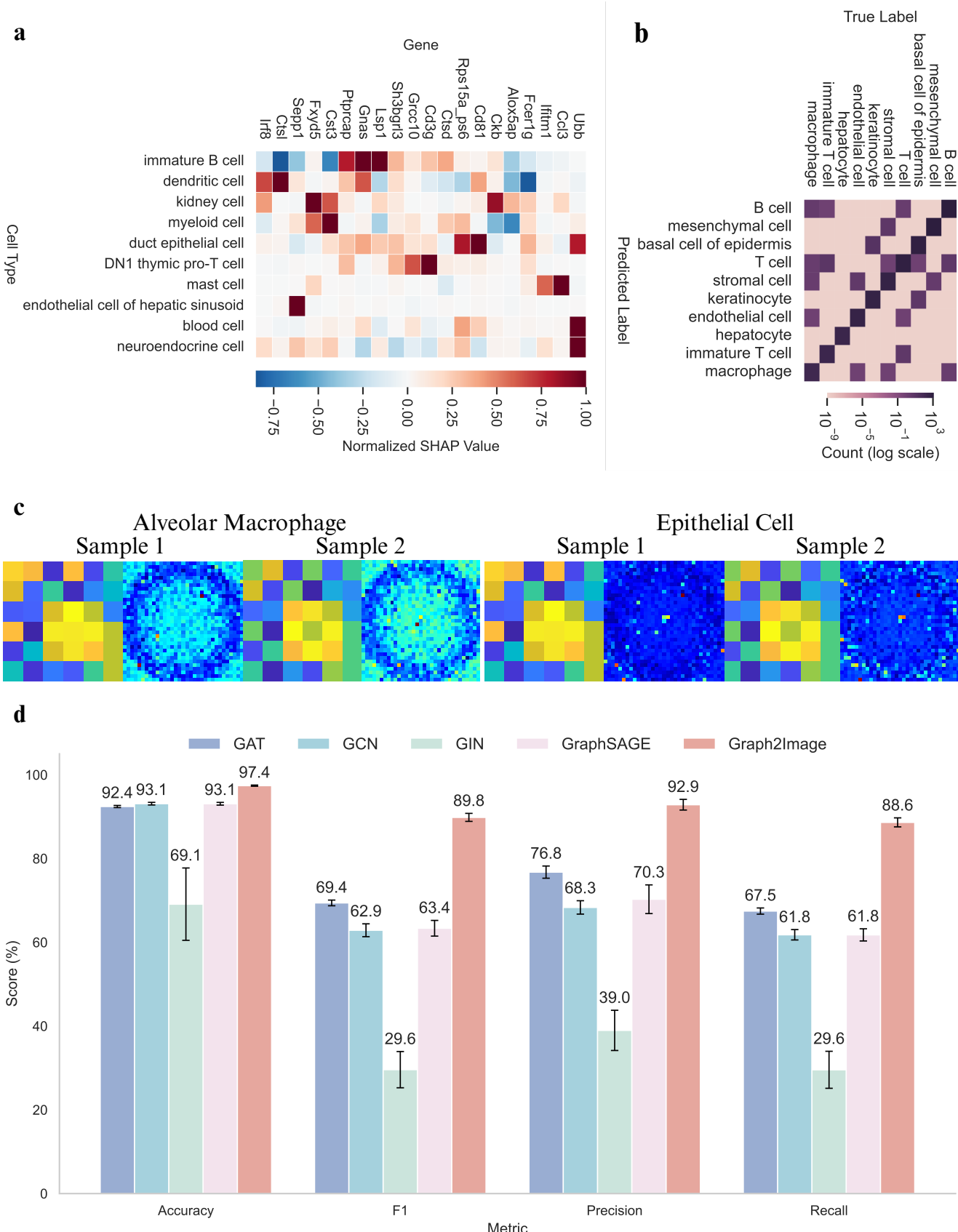


**Figure 4.** Performance and interpretability on the Tabula Muris dataset. **a**, Class-averaged SHAP heatmap for top marker genes across representative cell types; values are normalized SHAP scores. **b**, Confusion matrix of Graph2Image predictions across 55 cell types (counts in log scale). **c**, Representative Graph2Image outputs from Tabula Muris with samples from Alveolar Macrophage and Epithelial Cell. **d**, Classification comparison (Accuracy, F1, Precision, Recall) between Graph2Image and GNN baselines (GAT, GCN, GIN, GraphSAGE). See Supplementary Figs. S12, S13, and S14 for full-resolution confusion matrix, dendrogram and comprehensive heatmap.

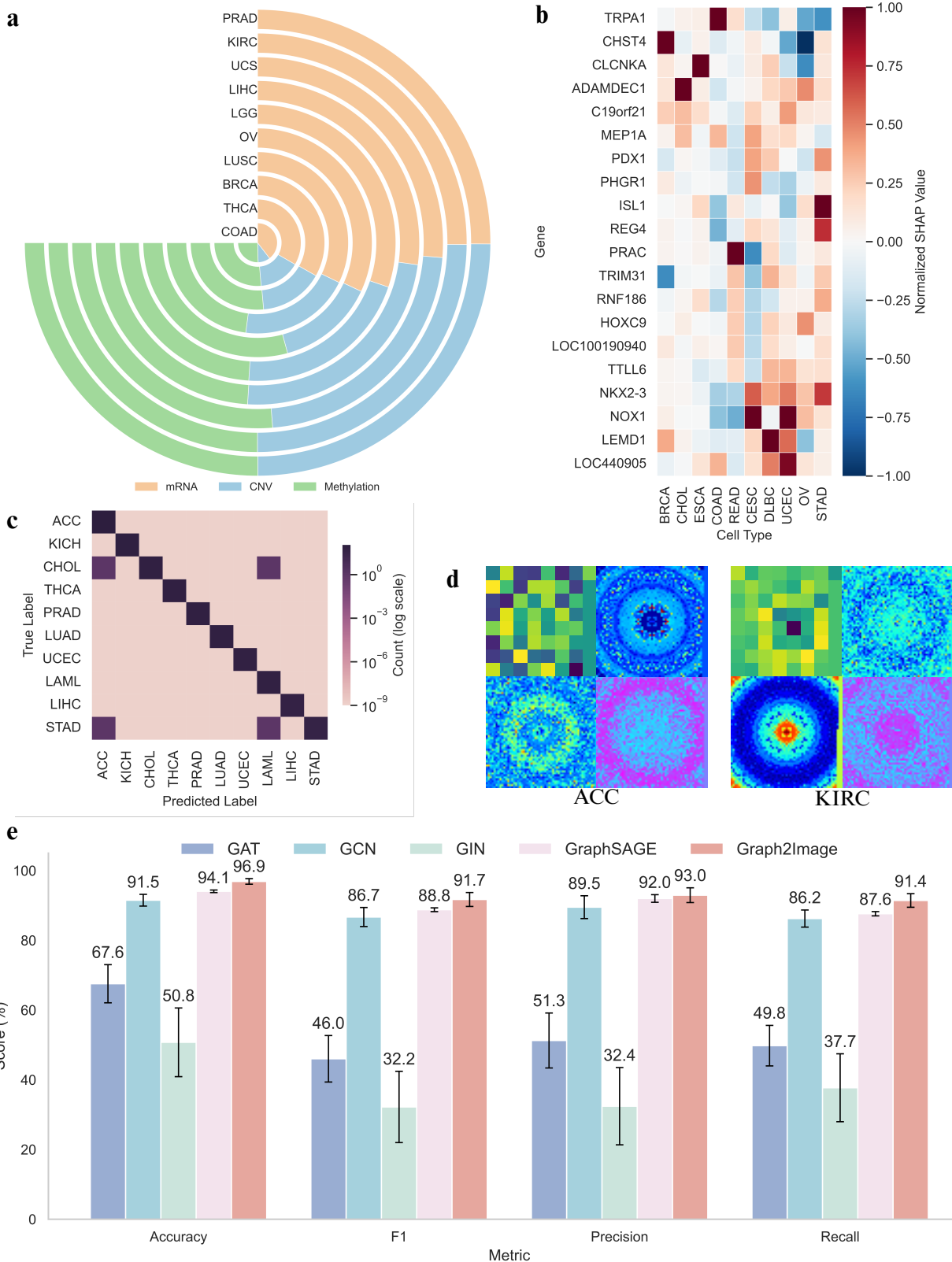


**Figure 5.** Performance and modality contributions on the pan-cancer cohort. **a**, Relative contribution of each omic layer (mRNA, CNV, DNA methylation) per cancer type, computed by aggregating SHAP importance. **b**, Class-averaged SHAP heatmap for top mRNA features across cancer types (normalized SHAP scores). **c**, Confusion matrix of Graph2Image predictions across 32 TCGA cancer types (log-scale counts). **d**, Representative Graph2Image outputs from the Pan Cancer dataset where images corresponds to different omics types of Adrenocortical carcinoma (ACC) and Kidney renal clear cell carcinoma (KIRC). **e**, Classification comparison (Accuracy, F1, Precision, Recall) between Graph2Image and GNN baselines. See Supplementary Figs. S15, S16, S17, and S18 for extended confusion matrices, heatmaps, modality breakdowns and clustering analyses. **10/65**

## 2.5 Graph2Image accurately classifies primary versus metastatic prostate cancer

To test our model's applicability in clinical settings, we applied it to the Prostate Cancer dataset. The task was to classify primary versus metastatic prostate cancer tumors. From Fig. 6d, Graph2Image achieved an accuracy of 99.0% and an F1-score of 98.8%, significantly outperforming benchmark GNNs. The second best method achieved an accuracy of 97.0% and F-1 score of 97.8%. The confusion matrix in Fig. 6a also shows the model's near-perfect classification, which establishes its robust capability to identify the molecular signatures that differentiate these two critical disease states. Again, we used SHAP analysis and in Fig. 6b showed that the model learned two distinct and biologically coherent molecular signatures corresponding to the different disease states (see Fig. S19 for detailed map). The features most predictive of metastatic classification point toward a phenotype of heightened metabolic activity, increased protein synthesis, and active tissue remodeling. These are all hallmarks of aggressive, invasive cancer<sup>98</sup>.

In Fig. 6b, Graph2Image's top-ranked feature was EEF1A1. This is a crucial translation elongation factor whose overexpression is essential to sustain the high rate of protein synthesis required by rapidly proliferating cancer cells<sup>99</sup>. This finding was supported by the high importance of other translation machinery components, such as EIF4A2 and multiple ribosomal proteins (e.g., RPL14, RPL7A). Furthermore, the model identified a signature of metabolic reprogramming. It heavily weighted genes involved in mitochondrial energy production (ATP5MG, COX7B) and altered lipid metabolism (APOC3)<sup>100</sup>. This anabolic signature was complemented by features essential for physical invasion, such as COL4A1. This gene is critical for remodeling the extracellular matrix during metastatic dissemination<sup>101</sup>. Conversely, the features predictive of primary, non-metastatic tumors reflected a more stable and differentiated cellular identity. The model correctly identified KLK3 as a key feature for this class. This gene encodes the Prostate-Specific Antigen (PSA) and is consistent with its role as the definitive clinical biomarker for prostate tissue<sup>102</sup>. This was reinforced by other markers of epithelial lineage, such as the cytokeratins KRT8 and KRT18. The model also associated a signature of stable cellular function with primary disease. It highlighted core "housekeeping" genes like RPS27 and RPS23. Their stable expression is indicative of a less transformed state, as these proteins are also involved in P53 tumor suppressor pathways<sup>103</sup>. Finally, the model highlighted the importance of GPX1, which encodes the antioxidant enzyme glutathione peroxidase 1<sup>104</sup>. This suggests the model learned that having a working system to manage oxidative stress is a key feature of less aggressive, localized tumors.

To formally assess whether the model organized these predictive genes into coherent biological group, we performed hierarchical clustering on the top predictive genes based on their SHAP profiles shown in Fig. S20. From Fig. S20, we see that the model groups genes into distinct functional modules. For example, the largest cluster was highly enriched for ribosomal proteins and translation factors. This demonstrates that the model's feature importance space is organized according to the biological functions that differentiate primary from metastatic disease.

Visual inspection of the Graph2Image outputs for the Prostate Cancer cohort further supports this separation. Primary tumors and metastatic lesions form two clearly distinct families of images: within each class, the structural channel and accompanying feature channels are highly consistent across patients, but the overall visual appearance differs sharply between the two disease states (Fig. 6c). Primary tumors exhibit a stable, symmetric pattern, whereas metastatic lesions display altered, more intense and spatially redistributed signals, mirroring the underlying shift toward a highly proliferative and invasive phenotype. These class-specific visual signatures provide an intuitive, image-based view of the molecular transition from localized to metastatic disease.

## 3 Discussion

In this work, we introduced Graph2Image, a biological graph cartography framework that overcomes the critical limitations of scalability and interpretability inherent in current biological network analysis methods. Our approach is highly scalable and have shown to be able to process the complete Tabula Muris cell atlas, a biological network with 54,865 nodes and over 3 billion edges, at a scale where leading GNN models failed. By reframing biological network analysis as an image recognition task, we achieve state-of-the-art performance across multiple biological contexts, including 99.0% accuracy in distinguishing metastatic from primary prostate cancer. More importantly, our results show that this transformation provides a powerful new lens for scientific discovery, as the model automatically recapitulated principles of developmental biology, acted as a "molecular pathologist" to identify cancer drivers, and learned the molecular signatures of tumor progression. Our model does more than just predict an outcome. It helps us understand the biology behind its decisions. This leads to new scientific discoveries.

In the two tissue-of-expression tasks, Graph2Image shows that the same cartographic machinery can recover stable tissue programs directly from pathway-derived and reference interactomes. On the PP-Pathways network, where nodes are proteins linked by curated pathway interactions and labeled by their dominant GTEx tissue-of-expression, the model accurately predicts the tissue label and, through SHAP, reconstructs a hierarchy of organ systems: adipose depots, arterial beds, adrenal gland, distal small intestine and mammary gland are each supported by coherent sets of tissue features, and their SHAP-based clustering recapitulates cardiovascular, endocrine and gastrointestinal modules that agree with transcriptomic and proteomic atlases<sup>51,53</sup>.

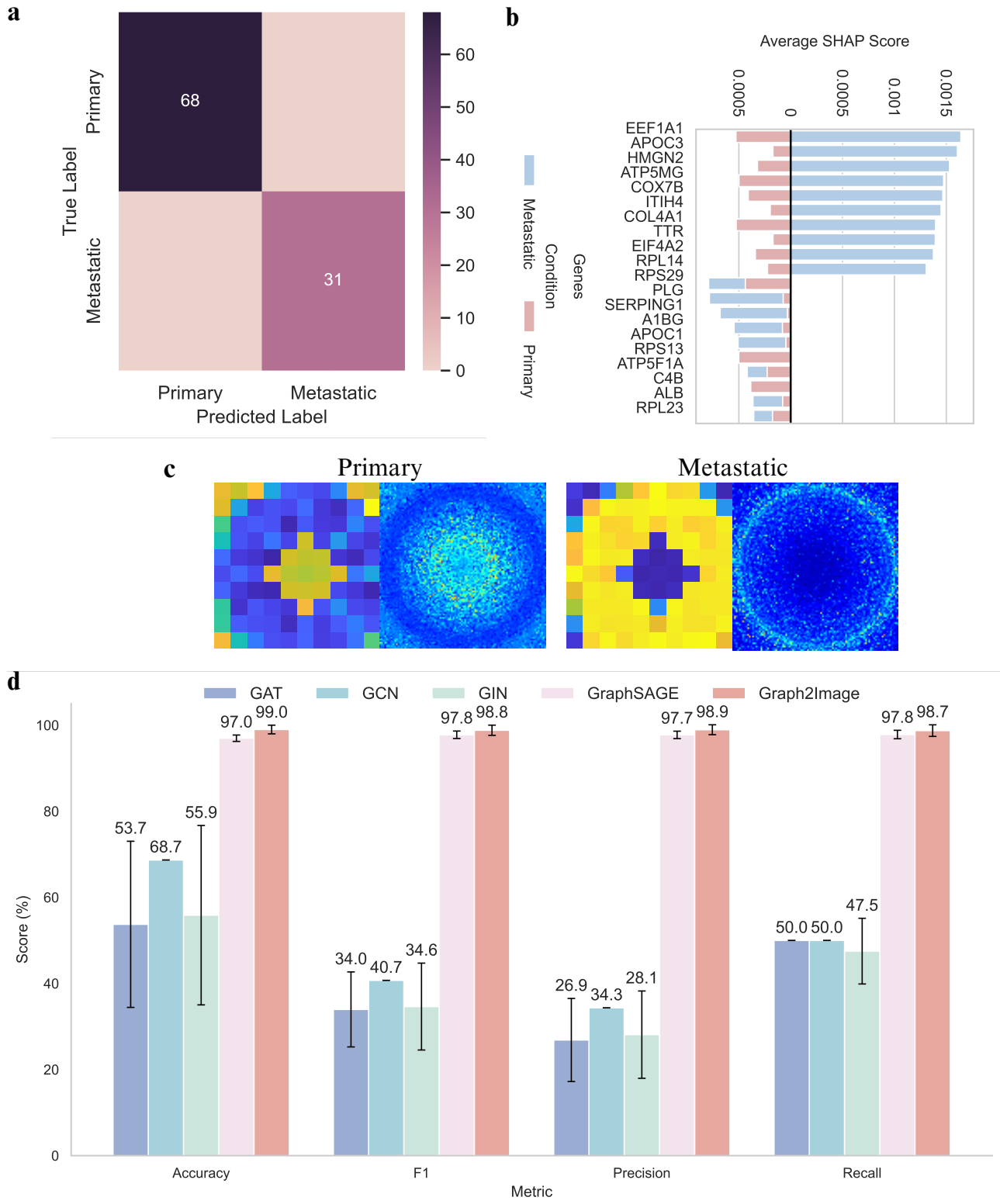


**Figure 6.** Primary versus metastatic prostate cancer classification and gene-level attributions. **a**, Confusion matrix for Graph2Image predictions on the Prostate Cancer cohort. **b**, Class-averaged SHAP scores for the most predictive genes, with directionality shown for metastatic (blue) and primary (red) classes. **c**, Representative Graph2Image outputs from the Prostate Cancer dataset where images corresponding to Primary and Metastatic tumors. **d**, Classification comparison (Accuracy, F1, Precision, Recall) between Graph2Image and GNN baselines. See Supplementary Figs. S19 and S20 for gene-level distributions and clustering of predictive features.

This shows that Graph2Image can use pathway connectivity plus bulk expression to rediscover large-scale physiological structure without being explicitly told about organ systems.

A complementary picture emerges from the HuRI interactome, which is constructed from high-throughput protein–protein interaction screens rather than pathway aggregation<sup>70</sup>. Here, Graph2Image again learns tissue-of-expression labels with high accuracy and organizes genes along interpretable tissue axes: immune- and blood-labeled genes are supported by a shared hematopoietic module, brain-labeled genes align with a central nervous system module, and reproductive tissues (ovary and testis) cluster with related endocrine and neuroendocrine features<sup>53, 71, 72</sup>. Across PP-Pathways and HuRI, the SHAP-based dendograms reveal consistent grouping of immune, stromal, neural, cardiovascular and endocrine tissues, suggesting that Graph2Image is capturing reproducible tissue programs that are robust to how the underlying interactome is constructed.

A key advantage of our framework is its inherent scalability and interpretability. As we have shown, GNNs often fail when faced with the massive, densely connected graphs typical of biological systems, requiring a significant loss of information through edge thresholding. Graph2Image bypasses this bottleneck by deconstructing the global biological graph analysis into a set of independent, fixed-size image classification problems—one for each node. This transformation makes the computational complexity linear with respect to the number of nodes and entirely sidesteps the recursive message-passing operations that constrain GNNs, enabling the analysis of biological networks at their true scale. Furthermore, our interpretability analysis of the Tabula Muris dataset in Fig. S13 demonstrates that the model’s learned feature space is hierarchically structured. This structure mirrors known developmental biology. The model learned to use broad, high-level markers like PTPRC to define an entire lineage, while also capturing fundamental sub-lineages, such as the lymphoid-myeloid dichotomy. Finally, it identified highly specific, exclusive markers for terminally differentiated cells, such as Alb for hepatocytes. The model organized the 55 cell types into coherent super-groups, correctly identifying canonical markers for the major hematopoietic, epithelial, and mesenchymal lineages, and recapitulating the lymphoid-myeloid dichotomy. The same machinery underlies the tissue hierarchies we observe in PP-Pathways and HuRI, indicating that Graph2Image learns a coherent taxonomy of both cell types and tissues from very different graphs. This ability to recover biologically meaningful structure from complex, whole-organism and whole-interactome data helps to validate the model’s internal logic and moves beyond traditional "black box" models by providing a clear framework for biological interpretation.

The analysis of the pan-cancer omics dataset further highlights the model’s systems-level understanding of cancer pathology. The model learned to dynamically weigh the importance of different molecular data types, i.e., gene expression, copy number variation, and DNA methylation, on a per-cancer basis, effectively learning the primary molecular driver for each disease. Its reliance on mRNA for functionally defined cancers like LIHC and PRAD, on CNV for genetically unstable cancers like OV, and on methylation for epigenetically driven cancers like LGG, demonstrates a subtle understanding that aligns with decades of cancer research. The prostate cancer analysis provides a powerful case study for the model’s ability to deconstruct the biology of tumor progression. Our model successfully distinguished primary from metastatic tumors with 99.0% accuracy by learning their opposing molecular signatures. It correctly identified primary tumors using markers of a stable, differentiated state, such as KLK3 (PSA). Conversely, it identified metastatic tumors by learning their signatures of heightened biosynthetic and metabolic activity, exemplified by genes like EEF1A1.

As seen from Figs. S21, S23, S25, S27, and S29, across all five datasets, we found that the embedding space learned by Graph2Image aligns more closely with the ground-truth labels than the embeddings produced by standard GNNs such as GCN, GAT, and GIN. From Table S13, Figs. S21 and S23, for the PP-Pathways and HuRI interactomes, respectively, Graph2Image is the only method that yields clearly non-trivial agreement between the embedding structure and the tissue labels, increasing ARI, NMI and silhouette scores over all GNN baselines and producing visibly tighter, more label-consistent clusters in t-SNE space. In Table S13 for the pan-cancer dataset, Graph2Image achieves an ARI of 0.87 and an NMI of 0.93, clearly outperforming the GNN baselines ( $ARI \approx 0.39\text{--}0.64$ ,  $NMI \approx 0.68\text{--}0.80$ ). This is reflected in the t-SNE plots in Fig. S27, where Graph2Image yields compact, well-separated clusters for each cancer type, whereas the GNN embeddings show elongated manifolds with partially overlapping classes. For the Tabula Muris dataset in Table S13, the ARI of Graph2Image is comparable to GCN and GAT, but the NMI and homogeneity are substantially higher (NMI 0.83 vs. 0.77–0.79; homogeneity 0.91 vs. 0.81), indicating that Graph2Image forms purer clusters whose label composition is closer to one-hot, consistent with the visually tighter CNN t-SNE clusters in Fig. S25. The advantage is most pronounced in the Prostate Cancer primary–metastasis cohort. In Table S13 Graph2Image attains an ARI of 0.67 and a very high silhouette score of 0.93, while all GNNs are near random ( $ARI \approx 0.05$  or even negative) and show heavy mixing of primary and metastatic samples in their t-SNE embeddings in Fig. S29. In contrast, the Graph2Image embedding separates primary tumors and metastases into clearly disjoint islands. Together, these quantitative metrics and qualitative visualizations show that Graph2Image learns a substantially more discriminative and label-consistent feature space than conventional GNN approaches.

While Graph2Image establishes a powerful new paradigm for graph analysis, it has certain limitations. The feature-mapping step is explicitly driven by how node features co-vary across the graph: it constructs a feature–feature association matrix from pairwise correlations and then uses this matrix to define the two-dimensional layout. Consequently, the approach works best for

modalities that exhibit rich, structured co-variation, such as gene expression or DNA methylation profiles, in which groups of features form coherent biological programs. In contrast, for feature sets that are extremely sparse or show little systematic correlation across nodes (for example, nearly binary mutation indicators), the resulting association matrix is less informative, and the corresponding feature maps may be less effective. Furthermore, the initial community detection step is critical; the quality of the structural embedding is sensitive to the number of communities chosen, and selecting a number that is too small or too large can distort the learned layout and adversely affect performance.

Graph2Image reframes biological network analysis as an image interpretation problem. This allows dense biological graphs to be processed end-to-end without aggressive sparsification while still providing direct access to feature attributions. We evaluated Graph2Image on two large human interactomes with tissue-of-expression labels, a whole-organism cell atlas, a pan-cancer multi-omics cohort, and a clinically relevant prostate cancer diagnosis task. In all five settings, the method achieved state-of-the-art classification performance. At the same time, it organized its decision space along known biological structures: it recovered established cell lineages in the atlas, captured tissue-of-origin relationships in interactomes and cancer, and identified coherent molecular programs that distinguish primary from metastatic disease. By standardizing biological graphs into multi-channel images, the framework aligns network biology with mature tools from computer vision and SHAP-based attribution, enabling scalable computation and transparent readouts at the level of genes and pathways. Taken together, these results position Graph2Image as a practical approach for analyzing large biological networks at their native scale, while coupling predictive performance with mechanistic interpretability.

## 4 Methods

Let us assume that a graph  $G = (V, E, F)$  represents the biological system that we want to analyze, where  $V$  is the set of vertices (nodes) with  $|V| = n$ ,  $E$  is the set of edges, and  $F \in \mathbb{R}^{n \times k}$  is the feature matrix. Graph2Image converts this attributed graph into a set of multi-channel images. First, we partition the  $n$  nodes into a set of  $P$  communities based on the graph's structure, where the number of communities  $P$  is determined by the number of node features  $k$ , such that  $P = \lceil \sqrt{k} \rceil$ . We then use these communities to create two distinct 2D embeddings, one for structure and one for features—which are combined into a final multi-channel image. As illustrated in Fig. 1, this transformation enables the graph's relational and feature information to be processed by CNNs.

### 4.1 Community Detection via Node Connectivity Profiles

Consider an undirected graph  $G = (V, E)$ , where  $V = \{v_1, v_2, \dots, v_n\}$  is the set of  $n$  vertices and  $E$  is the set of edges. The weighted adjacency matrix  $A$  of this graph is an  $n \times n$  matrix where each element  $A_{ij}$  is defined as:

$$A_{ij} = \begin{cases} w_{ij} & \text{if } \{v_i, v_j\} \in E \\ 0 & \text{if } \{v_i, v_j\} \notin E \end{cases} \quad (1)$$

where  $w_{ij}$  is the weight of the edge between vertex  $v_i$  and vertex  $v_j$ . In our experiments, we used graphs without any self-loops, so the diagonal elements  $A_{ii}$  are all 0. Since the graph is undirected, the adjacency matrix is symmetric, i.e.,  $A_{ij} = A_{ji}$  for all  $i, j$ .

Once we have the adjacency matrix, we identify the underlying community structure of the network by partitioning the nodes into  $P$  distinct groups, where  $P$  is set to  $\lceil \sqrt{k} \rceil$ . We treat the rows of the adjacency matrix  $A$  as a set of  $n$  vectors in an  $n$ -dimensional space,  $\{a_1, a_2, \dots, a_n\}$ , where each vector  $a_i$  represents the connectivity profile of node  $v_i$ .

The partitioning process is initialized by selecting  $P$  seed centroids using a probabilistic strategy designed to improve the quality of the final solution<sup>105</sup>. The initialization begins by choosing the first centroid,  $c_1$ , uniformly at random from the set of all node vectors. Subsequent centroids are then selected iteratively. For each node vector  $a_i$ , we compute the squared Euclidean distance  $D(a_i)^2 = \min_k \|a_i - c_k\|^2$  to the nearest existing centroid. A new centroid is then chosen from the set of all node vectors  $\{a_1, \dots, a_n\}$  with a probability proportional to this squared distance. This weighted selection, expressed as  $P(a_i) = D(a_i)^2 / \sum_{j=1}^n D(a_j)^2$ , is repeated until all  $P$  centroids have been seeded.

After initialization, the algorithm iteratively refines the cluster assignments and centroids to minimize the within-cluster sum of squares. Let  $S_k^{(t)}$  be the set of nodes belonging to cluster  $k$  at iteration  $t$ . In each iteration, an assignment step allocates each node vector  $a_i$  to the cluster  $S_k^{(t)}$  corresponding to its nearest centroid, based on the minimum squared Euclidean distance:

$$S_k^{(t)} = \{a_i : \|a_i - c_k^{(t)}\|^2 \leq \|a_i - c_j^{(t)}\|^2 \quad \forall j, 1 \leq j \leq P\}. \quad (2)$$

This partitions the  $n$  nodes into  $P$  clusters, defining the membership for each node  $v_i$ . Following the assignment, an update step recalculates the centroid of each cluster as the element-wise mean of all node vectors assigned to it:

$$c_k^{(t+1)} = \frac{1}{|S_k^{(t)}|} \sum_{a_i \in S_k^{(t)}} a_i. \quad (3)$$

This iterative process converges when the cluster assignments, and thus the node memberships, no longer change between iterations. The final output is a set of  $P$  centroids representing the identified communities and a partition of the nodes into these communities.

Following the partitioning of nodes into their respective communities, we quantify the relationships between these communities. The set of  $P$  final centroids,  $\{c_1, c_2, \dots, c_P\}$ , represents the average connectivity profiles of the identified communities. To measure the dissimilarity between these community profiles, we compute the pairwise Euclidean distance between each pair of centroid vectors. The element  $D_{kl}$  of the resulting  $P \times P$  distance matrix is calculated as:

$$D_{kl} = \|c_k - c_l\|_2 = \sqrt{\sum_{i=1}^n (c_{ki} - c_{li})^2} \quad (4)$$

where  $c_{ki}$  and  $c_{li}$  are the  $i$ -th elements of the centroid vectors  $c_k$  and  $c_l$ , respectively.

Finally, to normalize the distribution of these distances, we standardize the resulting matrix  $D$  using a z-score transformation. Each element  $Z_{kl}$  of the final standardized distance matrix  $Z$  is computed as:

$$Z_{kl} = \frac{D_{kl} - \mu_D}{\sigma_D} \quad (5)$$

where  $\mu_D$  and  $\sigma_D$  are the mean and standard deviation, respectively, of all elements in the distance matrix  $D$ . This transformation yields the final community association matrix used for the subsequent optimal transport mapping.

## 4.2 Optimal Transport for Spatial Mapping

With the inter-community relationships quantified, the next step is to arrange these  $P$  communities onto a single two-dimensional grid. The goal is to create a spatial map where the distance between communities on the grid reflects their structural similarity. We frame this as an Optimal Transport (OT) problem, which finds a correspondence between the geometry of the community relationships and the geometry of a physical grid<sup>106</sup>. The method operates on two metric measure spaces: the Community Space,  $(C_{\text{struct}}, p)$ , which represents the intrinsic geometry of all  $P$  discovered communities, and the Grid Space,  $(C_{\text{grid}}, q)$ , which represents the target 2D topology, with its cost matrix  $C_{\text{grid}}$  composed of the pairwise squared Euclidean distances between all  $P$  locations on the grid template.

We utilize the Gromov-Wasserstein (GW) discrepancy to align these two geometric structures<sup>107</sup>. The GW framework finds an optimal transport plan  $T$  that minimizes the distortion between the two distance matrices, ensuring that highly associated communities are mapped to proximal locations on the grid. The GW distance is formally defined as:

$$d_{GW}(C_{\text{struct}}, C_{\text{grid}}, p, q) := \min_{T \in \Pi(p, q)} \sum_{i,j,k,l} (C_{\text{struct}}(i, k) - C_{\text{grid}}(j, l))^2 T_{ij} T_{kl} \quad (6)$$

where  $\Pi(p, q) = \{T \in \mathbb{R}^{P \times P} \mid T\mathbf{1}_P = p, T^T\mathbf{1}_P = q\}$ . The optimization yields a single transport plan  $T$  that is resolved into a permutation matrix. This matrix dictates a fixed spatial position for each of the  $P$  communities on the 2D grid, creating a **single master structural layout** that preserves the graph's overall relational information.

From this master layout, we then generate a unique image for each individual community. For a given community, its corresponding image is created by populating the grid locations with the z-scored structural similarity values between itself and all other communities in their assigned master positions. This ensures that while all images share the same spatial arrangement of communities, the pixel intensities of each image reflect the specific relational profile of its corresponding community.

In practice, solving for the exact transport plan can be computationally intensive. To improve efficiency, the OT problem can be regularized with an entropy term,  $-\varepsilon H(T)$ <sup>108</sup>. This yields a probabilistic mapping that can be resolved into a discrete assignment using a linear sum assignment algorithm<sup>109</sup>. For all main results in this work, we set  $\varepsilon = 0$  to obtain the exact, unregularized transport matrix.

## 4.3 Image Construction from Structural and Feature Embeddings

Biological networks are typically accompanied by features for individual nodes<sup>110</sup>. Since each node in the graph was converted to a 2D grid of spatial embedding, the logical step is to convert the features of each node into a 2D feature embedding to ensure that a CNN can be trained with both structural and functional information. We represent the node features as a matrix  $F \in \mathbb{R}^{n \times k}$ , where  $n$  is the number of nodes and  $k$  is the number of features per node. To create an image-like representation of these features, we follow a similar OT-based approach as was used for the graph structure.

First, we compute a pairwise feature association matrix,  $C_{\text{feat}} \in \mathbb{R}^{k \times k}$ . This is achieved by calculating the Pearson correlation between each pair of feature vectors (the columns of the feature matrix  $F$ ), after z-score normalizing each column. Let  $f_j$  and

$f_l$  be the column vectors for the  $j$ -th and  $l$ -th features in  $F$ , respectively. The feature association matrix  $C_{\text{feat}}$  is computed as:

$$C_{\text{feat}} = \frac{\sum_{i=1}^n (f_{ij} - \bar{f}_j)(f_{il} - \bar{f}_l)}{\sqrt{\sum_{i=1}^n (f_{ij} - \bar{f}_j)^2} \sqrt{\sum_{i=1}^n (f_{il} - \bar{f}_l)^2}} \quad (7)$$

where  $f_{ij}$  is the value of the  $j$ -th feature for the  $i$ -th node, and  $\bar{f}_j$  is the mean of the  $j$ -th feature vector. The OT algorithm (Eq. 6) is again applied to find the optimal mapping of these  $P$  community feature profiles onto a separate  $P \times P$  grid, creating a feature embedding that spatially encodes feature relationships.

This process results in two distinct embeddings. First, we obtain a structural embedding of the  $P$  communities, and next a feature embedding of the  $k$  features. To ensure these two embeddings are compatible for concatenation, the smaller of the two is zero-padded to match the dimensions of the larger one. For instance, the structural embedding of the  $P$  communities is mapped in the center of a matrix with zeros onto a grid of size  $P_s \times P_s$ , where  $P_s = \lceil \sqrt{P} \rceil$ . Since  $P_s \leq P$ , the structural embedding is padded with zeros to match the  $P \times P$  dimensions of the feature embedding. Finally, the two compatible  $P \times P$  embeddings are concatenated as separate channels to form the final Graph2Image, a multi-channel image of shape  $P \times P \times 2$ . Furthermore, this channel-based approach naturally allows for the integration of multi-omics data; a separate feature embedding can be created for each modality and concatenated as an additional channel in the final image. This final representation, which synergistically encodes both structural and feature information, is then used to train deep learning models.

#### 4.4 CNN Architecture and Model Training

Once the node-specific images are constructed, we train a CNN to perform the classification task. The network architecture is designed to process the multi-channel image inputs, each of size  $P \times P$ . The model consists of a feature extraction backbone and a subsequent classifier head. The feature extractor comprises four sequential 2D convolutional layers, each employing a  $5 \times 5$  kernel with 16 filters. To maintain spatial resolution throughout the feature extraction process, we use same padding. A Rectified Linear Unit (ReLU) activation function is applied after each convolutional layer to introduce non-linearity. Following the convolutional blocks, the resulting feature maps are flattened into a vector and passed to a classifier head, which consists of two fully connected layers of 768 and 512 neurons, respectively. The output of the network is a final fully connected layer with a dimension equal to the number of classes, followed by a softmax activation function to produce a class probability distribution. The model is trained by minimizing the cross-entropy loss. While this study employs a standard CNN architecture to demonstrate the fundamental efficacy of the Graph2Image transformation, the framework is flexible and could readily incorporate more advanced convolutional designs.

For model training, the dataset was partitioned into training (70%), validation (15%), and testing (15%) sets. The network was trained using the Stochastic Gradient Descent with Momentum (SGDM) optimizer with an initial learning rate of  $3 \times 10^{-4}$  and a mini-batch size of 32. The model was trained for a maximum of 20 epochs, with the training data shuffled at the beginning of each epoch. To prevent overfitting and select the best-performing model, the network's performance on the validation set was evaluated at regular intervals during training. The model that achieved the lowest loss on the validation set was selected for final evaluation on the held-out test set. Performance was assessed using accuracy, precision, F1-score, and recall.

#### 4.5 Model Interpretability with SHapley Additive exPlanations

To deconstruct the biological principles learned by the trained CNN and identify the features driving its predictions, we employed SHapley Additive exPlanations (SHAP), a game-theoretic approach for explaining the output of any machine learning model<sup>111</sup>. For a given prediction, SHAP assigns each feature an importance value, or Shapley value, representing its contribution to pushing the model's output from a baseline value, defined as the average prediction over a background dataset. The Shapley value for a feature  $j$ ,  $\phi_j$ , is calculated by considering all possible subsets of features  $S \subseteq F \setminus \{j\}$ , where  $F$  is the set of all features. The value is the weighted average of the feature's marginal contribution across all these subsets:

$$\phi_j(f, x) = \sum_{S \subseteq F \setminus \{j\}} \frac{|S|!(|F| - |S| - 1)!}{|F|!} [f_x(S \cup \{j\}) - f_x(S)] \quad (8)$$

where  $f_x(S)$  is the model's prediction for input  $x$  given only the subset of features  $S$ .

In our implementation, we first computed local, per-sample SHAP values for a subset of the 1000 most informative features for each sample in the test set. To select these features, we identified the most highly variable features from the feature matrix  $F$ . This was achieved using a variance-stabilizing transformation, which models the mean-variance relationship in the data to identify features with higher-than-expected variance. This standard approach ensures that the subsequent, computationally intensive SHAP analysis is focused on the features most likely to contribute to the biological differences between classes. For a specific sample  $x_i$  and a target class  $c$ , we defined a prediction function that returns the model's softmax score for that class. The shapley explainer was then used to compute the contribution of each pixel in the multi-channel Graph2Image to

this prediction score, using the full dataset as a background reference to establish the baseline prediction. To obtain a global understanding of the model’s decision-making for a particular class, we then averaged these local SHAP values for each feature across all test samples belonging to that class. This resulted in a class-specific global importance score for every feature. Finally, using the permutation matrices generated by the OT algorithm, these pixel-level importance scores were mapped back to their original biological identities (i.e., gene names for the feature channel), allowing us to identify the specific genes that positively or negatively influenced the classification.

## 4.6 Datasets

### 4.6.1 PP-Pathways tissue-of-expression interactome

To evaluate Graph2Image on a pathway-derived protein–protein interaction network, we used the PP-Pathways human interactome from the SNAP collection<sup>50</sup>. This resource aggregates experimentally supported physical interactions from multiple curated pathway databases into a heterogeneous network of human proteins, providing a systems-level view of signaling and metabolic pathways. To obtain biologically meaningful node features and labels, we overlaid GTEx v8 bulk RNA-seq profiles onto the network<sup>51,52</sup>. For each gene present in both PP-Pathways and GTEx, we computed log-transformed expression features by averaging Transcripts Per Million (TPM) across all samples from the same tissue and taking  $\log_2(\text{TPM} + 1)$ , yielding a gene-by-tissue feature matrix across 54 GTEx tissues. We then assigned each gene a tissue-of-expression label defined as the tissue in which it has the highest mean expression, resulting in a 54-class tissue-of-expression prediction task (see Supplementary Table S1).

### 4.6.2 HuRI and GTEx tissue interactome

To test whether our approach can recover tissue programs directly from a high-quality reference interactome, we used the Human Reference Interactome (HuRI), which compiles systematically mapped, high-confidence human protein–protein interactions<sup>70</sup>. HuRI encompasses thousands of proteins connected by tens of thousands of binary interactions, capturing a broad range of cellular pathways in a tissue-agnostic manner. As in the PP-Pathways analysis, we annotated HuRI genes with GTEx v8 bulk RNA-seq expression across normal tissues<sup>52,71,72</sup>. For each gene, we summarized expression as  $\log_2(\text{TPM} + 1)$  averaged over donors within each tissue and defined its primary tissue label as the tissue with maximal mean expression. For downstream benchmarking, we focused on nine tissues with robust representation and clear physiological roles—whole blood, brain-cerebellum, brain-cerebellar hemisphere, skeletal muscle, thyroid, ovary, testis, EBV-transformed lymphoblastoid cell lines, and cultured fibroblasts—yielding a nine-way tissue-of-expression classification problem on the HuRI network.

### 4.6.3 Tabula Muris

To assess our method’s performance on a complex cellular landscape, we used the Tabula Muris collection, a foundational single-cell atlas of the model organism *Mus musculus*<sup>112</sup>. This dataset captures the transcriptomic state of diverse and interacting cell populations across 20 organs, providing a system-wide view of cellular heterogeneity. We utilized a pre-processed version containing 54,865 cells across 55 distinct cell types (see Supplementary Table S4), selecting the 1,089 most highly variable genes to model the core cellular interaction network (see Supplementary Tables S5, S6, S7).

### 4.6.4 Pan-Cancer Multi-Omics (MLOmics)

To challenge our model’s ability to detect patterns across heterogeneous cancer systems, we utilized the Pan-Cancer dataset from the MLOmics benchmark<sup>113</sup>. This dataset provides a systems-level view of tumor biology by integrating molecular profiles (gene expression, DNA methylation, and copy number variation) from 8314 tumor samples across 32 distinct cancer types from The Cancer Genome Atlas (TCGA) (see Supplementary Table S9 for class names). The task was to classify tumors based on their integrated molecular state, reflecting the underlying regulatory networks that define each cancer type.

### 4.6.5 Prostate Cancer

To evaluate our method on a clinically critical task, we used transcriptomic data from the P-Net study, which profiled a large cohort of prostate cancer patients<sup>114</sup>. The dataset comprises 1,013 patient samples, divided into two distinct classes: 680 primary tumors and 333 metastatic tumors. The goal was to distinguish between these two disease states, a key challenge in clinical oncology. For our analysis, we constructed the network using the top 5,000 most highly variable genes from the expression data before applying the Graph2Image pipeline.

## References

1. Tucker, C. L., Gera, J. F. & Uetz, P. Towards an understanding of protein–protein interaction maps. *Trends cell biology* **11**, 102–106 (2001).
2. Barabási, A.-L. & Oltvai, Z. N. Network biology: understanding the cell’s functional organization. *Nat. Rev. Genet.* **5**, 101–113 (2004).

3. Davidson, E. H. *et al.* A genomic regulatory network for development. *Science* **295**, 1669–1678 (2002).
4. Sporns, O., Tononi, G. & Kötter, R. The human connectome: a structural description of the human brain. *PLoS Comput. Biol.* **1**, e42 (2005).
5. Bullmore, E. & Sporns, O. Complex brain networks: graph theoretical analysis of structural and functional systems. *Nat. Rev. Neurosci.* **10**, 186–198 (2009).
6. Ideker, T. & Sharan, R. Protein networks in disease. *Genome Res.* **18**, 644–652 (2008).
7. Kitano, H. Systems biology: a brief overview. *Science* **295**, 1662–1664 (2002).
8. Jeong, H., Tombor, B., Albert, R., Oltvai, Z. N. & Barabási, A.-L. The large-scale organization of metabolic networks. *Nature* **407**, 651–654 (2000).
9. Rouunge, T. B., Umu, S. U., Keller, A. & Meese, E. The human microbiome and its applications in medicine. *J. internal medicine* **288**, 618–638 (2020).
10. Keeling, M. J. & Eames, K. T. Networks and epidemic models. *J. Royal Soc. Interface* **2**, 295–307 (2005).
11. Dunne, J. A., Williams, R. J. & Martinez, N. D. Food-web structure and network theory: The role of connectance and size. *Proc. Natl. Acad. Sci.* **99**, 12917–12922 (2002).
12. Hartwell, L. H., Hopfield, J. J., Leibler, S. & Murray, A. W. From molecular to modular cell biology. *Nature* **402**, C47–C52 (1999).
13. Alon, U. Network motifs: theory and experimental approaches. *Nat. reviews genetics* **8**, 450–461 (2007).
14. Yildirim, M. A., Goh, K.-I., Cusick, M. E., Barabási, A.-L. & Vidal, M. Drug–target network. *Nat. biotechnology* **25**, 1119–1126 (2007).
15. Camacho, D. M., Collins, K. M., Powers, R. K., Costello, J. C. & Collins, J. J. Next-generation machine learning for biological networks. *Cell* **173**, 1581–1592 (2018).
16. Gaudelet, T. *et al.* Utilizing graph machine learning within drug discovery and development. *Briefings bioinformatics* **22** (2021).
17. Zhang, W., Chien, J., Yong, J. & Kuang, R. Network-based machine learning and graph theory algorithms for precision oncology. *NPJ precision oncology* **1**, 25 (2017).
18. Chhibber, A. & Bafna, V. Network-based approaches in cancer genomics. *Curr. Opin. Syst. Biol.* **26**, 100342 (2021).
19. Hasin, Y., Seldin, M. & Lusis, A. Multi-omics approaches to disease. *Nat. Rev. Genet.* **18**, 261–274 (2017).
20. Szklarczyk, D. *et al.* The string database in 2021: customizable protein–protein networks, and functional characterization of user-uploaded gene/measurement sets. *Nucleic acids research* **49**, D605–D612 (2021).
21. Batarfi, O. *et al.* Large scale graph processing systems: survey and an experimental evaluation. *Clust. Comput.* **18**, 1189–1213 (2015).
22. Zou, L. *et al.* A survey on large-scale graph processing and learning. *ACM Comput. Surv.* **55**, 1–38 (2023).
23. Shi, J. & Malik, J. Normalized cuts and image segmentation. *IEEE Transactions on pattern analysis machine intelligence* **22**, 888–905 (2000).
24. Von Luxburg, U. A tutorial on spectral clustering. *Stat. computing* **17**, 395–416 (2007).
25. Ng, A. Y., Jordan, M. I. & Weiss, Y. On spectral clustering: Analysis and an algorithm. *Adv. Neural Inf. Process. Syst.* **14** (2002).
26. Vishwanathan, S. V. N., Schraudolph, N. N., Kondor, R. & Borgwardt, K. M. Graph kernels. *The J. Mach. Learn. Res.* **11**, 1201–1242 (2010).
27. Shervashidze, N., Schweitzer, P., Van Leeuwen, E. J., Mehlhorn, K. & Borgwardt, K. M. Weisfeiler-lehman graph kernels. *J. Mach. Learn. Res.* **12** (2011).
28. Shervashidze, N. & Borgwardt, K. Fast subtree kernels on graphs. *Adv. neural information processing systems* **22** (2009).
29. Borgwardt, K. M. *et al.* Protein function prediction via graph kernels. *Bioinformatics* **21**, i47–i56 (2005).
30. Wu, Z. *et al.* A comprehensive survey on graph neural networks. *IEEE Transactions on Neural Networks Learn. Syst.* **32**, 4–24 (2021).
31. Zhou, J. *et al.* Graph neural networks: A review of methods and applications. *AI open* **1**, 57–81 (2020).

32. Zhang, Z., Cui, P. & Zhu, W. Deep learning on graphs: A survey. *IEEE Transactions on Knowl. Data Eng.* **34**, 249–270 (2020).
33. Kipf, T. Semi-supervised classification with graph convolutional networks. *arXiv preprint arXiv:1609.02907* (2016).
34. Defferrard, M., Bresson, X. & Vandergheynst, P. Convolutional neural networks on graphs with fast localized spectral filtering. *Adv. neural information processing systems* **29** (2016).
35. Hamilton, W., Ying, Z. & Leskovec, J. Inductive representation learning on large graphs. *Adv. neural information processing systems* **30** (2017).
36. Chen, J., Zhu, J. & Song, L. Stochastic training of graph convolutional networks with variance reduction. *arXiv preprint arXiv:1710.10568* (2017).
37. Veličković, P. *et al.* Graph attention networks. *arXiv preprint arXiv:1710.10903* (2017).
38. Zhang, J. *et al.* Gaan: Gated attention networks for learning on large and spatiotemporal graphs. *arXiv preprint arXiv:1803.07294* (2018).
39. Xu, K., Hu, W., Leskovec, J. & Jegelka, S. How powerful are graph neural networks? *arXiv preprint arXiv:1810.00826* (2018).
40. Morris, C. *et al.* Weisfeiler and leman go neural: Higher-order graph neural networks. In *Proceedings of the AAAI conference on artificial intelligence*, vol. 33, 4602–4609 (2019).
41. Wu, Z. *et al.* A comprehensive survey on graph neural networks. *IEEE transactions on neural networks learning systems* **32**, 4–24 (2020).
42. Hamilton, W. L., Ying, R. & Leskovec, J. Representation learning on graphs: Methods and applications. *arXiv preprint arXiv:1709.05584* (2017).
43. Li, Q., Han, Z. & Wu, X.-M. Deeper insights into graph convolutional networks for semi-supervised learning. In *Proceedings of the AAAI conference on artificial intelligence*, vol. 32 (2018).
44. Alon, U. & Yahav, E. On the bottleneck of graph neural networks and its practical implications. *arXiv preprint arXiv:2006.05205* (2020).
45. Garg, V. K., Jegelka, S. & Jaakkola, T. Generalization and representational limits of graph neural networks. In *International Conference on Machine Learning*, 3423–3433 (PMLR, 2020).
46. Chen, Z., Chen, L., Villar, S. & Bruna, J. Can graph neural networks count substructures? In *Advances in Neural Information Processing Systems*, vol. 33, 10383–10395 (2020).
47. Chami, I., Abu-El-Haija, S., Perozzi, B., Ré, C. & Murphy, K. Machine learning on graphs: A model and comprehensive taxonomy. *J. Mach. Learn. Res.* **23**, 1–98 (2022).
48. Ying, R., Bourgeois, D., You, J., Zitnik, M. & Leskovec, J. Gnnexplainer: Generating explanations for graph neural networks. In *Advances in neural information processing systems*, vol. 32 (2019).
49. Yuan, H., Yu, H., Gui, S. & Ji, S. Explainability in graph neural networks: A taxonomic survey. *IEEE Transactions on Pattern Analysis Mach. Intell.* **45**, 5783–5801 (2022).
50. Stanford Network Analysis Platform. Pp-pathways network. <https://snap.stanford.edu/biodata/datasets/10004/10004-PP-Pathways.html> (2024). Human protein–protein interaction network aggregated from pathway databases.
51. GTEx Consortium. The GTEx consortium atlas of genetic regulatory effects across human tissues. *Science* **369**, 1318–1330 (2020).
52. GTEx Consortium. Adult GTEx: Tissue and sample statistics. <https://gtexportal.org> (2024).
53. Uhlén, M., Fagerberg, L. *et al.* Tissue-based map of the human proteome. *Science* **347**, 1260419 (2015).
54. Kershaw, E. E. & Flier, J. S. Adipose tissue as an endocrine organ. *J. Clin. Endocrinol. Metab.* **89**, 2548–2556 (2004).
55. Ahima, R. S. & Flier, J. S. Adipose tissue as an endocrine organ. *Trends Endocrinol. Metab.* **11**, 327–332 (2000).
56. Dutt, M. & Diwan, D. Physiology, adrenal gland. *StatPearls* (2023). StatPearls Publishing.
57. Chaudhry, R., Zha, A. *et al.* Physiology, cardiovascular. *StatPearls* (2022). StatPearls Publishing.
58. Cleveland Clinic. How blood flows through the heart & body. <https://my.clevelandclinic.org/health/articles/17060-how-does-the-blood-flow-through-your-heart> (2017).
59. Basile, E. J. & colleagues. Physiology, nutrient absorption. *StatPearls* (2023). StatPearls Publishing.

60. Collins, J. T. *et al.* Anatomy, abdomen and pelvis, small intestine. *StatPearls* (2024). StatPearls Publishing.

61. Kobayashi, K. *et al.* Culture models to investigate mechanisms of milk production. *Cell Tissue Res.* **392**, 1–15 (2023).

62. Shennan, D. B. & Peaker, M. Transport of milk constituents by the mammary gland. *Physiol. Rev.* **80**, 925–951 (2000).

63. Duval, A., Jin, H.-W., Paurat, D. & Tixier, A. J.-P. Graphsvx: A universal and efficient framework for explaining graph neural networks. In *Proceedings of the 2021 International Conference on Management of Data*, 2501–2505 (2021).

64. Jin, W. *et al.* Orphicx: A causal-inspired shapley-based method for explaining graph neural networks. *Briefings Bioinforma.* **23**, bbac417 (2022).

65. Ying, R., Bourgeois, D., You, J., Zitnik, M. & Leskovec, J. Gnnexplainer: Generating explanations for graph neural networks. In *NeurIPS* (2019).

66. Duval, A. & Malliaros, F. D. Graphsvx: Shapley value explanations for graph neural networks. In *ECML PKDD* (2021).

67. Lin, W., Lan, H., Wang, H. & Li, B. Orphicx: A causality-inspired latent variable model for interpreting graph neural networks. In *CVPR* (2022).

68. Canadian Cancer Society. Adrenal gland hormones. *Online resource* (2022).

69. Duca, F. A. *et al.* The metabolic impact of small intestinal nutrient sensing. *Nat. Commun.* **12**, 903 (2021).

70. Luck, K. *et al.* A reference map of the human binary protein interactome. *Nature* **580**, 402–408 (2020).

71. GTEx Consortium. Genetic effects on gene expression across human tissues. *Nature* **550**, 204–213 (2017).

72. GTEx Consortium. The GTEx consortium atlas of genetic regulatory effects across human tissues. *Science* **369**, 1318–1330 (2020).

73. Kalluri, R. The biology and function of fibroblasts in cancer. *Nat. Rev. Cancer* **16**, 582–598 (2016).

74. Omi, N. *et al.* Efficient and reliable establishment of lymphoblastoid cell lines. *Sci. Reports* **7**, 43833 (2017).

75. Wroblewski, J. M. *et al.* Epstein–barr virus-transformed b lymphoblastoid cell lines as a model of b-cell activation. *J. Immunol.* **169**, 643–650 (2002).

76. Murphy, K. *Janeway's Immunobiology* (Garland Science, 2012), 8 edn.

77. Fox, R. I. *et al.* Expression of histocompatibility antigen hla-dr by salivary gland epithelial cells. *Arthritis Rheum.* **29**, 1105–1111 (1986).

78. Zhang, K. *et al.* Identification of key genes in salivary gland in sjögren's syndrome and their association with thyroid autoimmunity. *Medicine* **102**, e35155 (2023).

79. Lin, Y. *et al.* Potential common mechanisms between primary sjögren's syndrome and hashimoto's thyroiditis. *Front. Genet.* **16**, 1520332 (2025).

80. Weigert, M. *et al.* Reproductive hormones coordinate gene expression programs across uterus, ovary and fallopian tube. *Commun. Biol.* (2025). In press.

81. Ulrich, N. D. *et al.* Cellular heterogeneity of human fallopian tubes in normal and disease states. *Cell Reports* **39**, 110757 (2022).

82. Lengyel, E. *et al.* A molecular atlas of the human postmenopausal fallopian tube. *Cell Reports* **39**, 111023 (2022).

83. Human Protein Atlas Project. The fallopian tube-specific proteome. <https://www.proteinatlas.org/humanproteome/tissue/fallopian+tube> (2025). Accessed 2025.

84. Hedger, M. P. The immunophysiology of male reproduction. *Springer Handb. Immunotoxicol.* 405–429 (2014).

85. Li, N. *et al.* Structural, cellular and molecular aspects of immune privilege in the testis. *Front. Immunol.* **3**, 152 (2012).

86. Hermiston, M. L., Xu, Z. & Weiss, A. CD45: a critical regulator of t-cell activation. *Annu. Rev. Immunol.* **21**, 107–137 (2003).

87. Karasuyama, H., Rolink, A. & Melchers, F. The pre-b-cell receptor: a new molecular complex on b-cell precursors. *Curr. Opin. Immunol.* **6**, 225–230 (1994).

88. Clevers, H., Alarcon, B., Wileman, T. & Terhorst, C. The t cell receptor/cd3 complex: a dynamic protein ensemble. *Annu. Rev. Immunol.* **6**, 629–662 (1988).

89. Faurschou, M. & Borregaard, N. Neutrophil granules and secretory vesicles in inflammation. *Microbes Infect.* **5**, 1317–1327 (2003).

90. Tamura, T. & Ozato, K. ICSBP/IRF-8: a key transcription factor for myeloid development. *J. Interf. & Cytokine Res.* **22**, 145–152 (2002).

91. Trzpis, M., McLaughlin, P. M., de Leij, L. M. & Harmsen, M. C. Epithelial cell adhesion molecule: more than a carcinoma marker and adhesion molecule. *The Am. J. Pathol.* **171**, 386–395 (2007).

92. Franke, W. W., Schmid, E., Osborn, M. & Weber, K. Different intermediate-sized filaments distinguished by immunofluorescence microscopy. *Proc. Natl. Acad. Sci.* **75**, 5034–5038 (1978).

93. Rothschild, M. A., Oratz, M. & Schreiber, S. S. Albumin synthesis. *New Engl. J. Medicine* **286**, 748–757 (1972).

94. Weaver, T. E. & Conkright, J. J. Function of surfactant proteins b and c. *Annu. Rev. Physiol.* **63**, 555–578 (2001).

95. Hoadley, K. A. *et al.* Multiplatform analysis of 12 cancer types reveals molecular classification within and across tissues of origin. *Cell* **158**, 929–944 (2014).

96. Network, C. G. A. R. Integrated genomic analyses of ovarian carcinoma. *Nature* **474**, 609–615 (2011).

97. Noushmehr, H. *et al.* Identification of a cpg island methylator phenotype that defines a distinct subgroup of glioma. *Cancer Cell* **17**, 510–522 (2010).

98. Hanahan, D. & Weinberg, R. A. Hallmarks of cancer: the next generation. *Cell* **144**, 646–674 (2011).

99. Abbas, W., Kausar, S. & Kumar, A. The eef1a proteins: at the crossroads of oncogenesis, apoptosis, and viral infections. *Front. Oncol.* **5**, 75 (2015).

100. Cairns, R. A., Harris, I. S. & Mak, T. W. Regulation of cancer cell metabolism. *Nat. Rev. Cancer* **11**, 85–95 (2011).

101. Kalluri, R. Basement membranes: structure, assembly and role in tumour angiogenesis. *Nat. Rev. Cancer* **9**, 587–598 (2009).

102. Lilja, H. A kallikrein-like serine protease in prostatic fluid cleaves the predominant seminal vesicle protein. *J. Clin. Investig.* **76**, 1899–1903 (1985).

103. Deisenroth, C. & Zhang, Y. Ribosome biogenesis surveillance: probing the ribosomal protein-mdm2-p53 pathway. *Oncogene* **29**, 4253–4260 (2010).

104. Chu, F.-F., Esworthy, R. S. & Doroshow, J. H. Role of glutathione peroxidase in the toxicology of anticancer agents. *Curr. Drug Targets* **5**, 423–432 (2004).

105. Arthur, D. & Vassilvitskii, S. k-means++: The advantages of careful seeding. Tech. Rep., Stanford (2006).

106. Peyré, G., Cuturi, M. *et al.* Computational optimal transport: With applications to data science. *Foundations Trends Mach. Learn.* **11**, 355–607 (2019).

107. Peyré, G., Cuturi, M. & Solomon, J. Gromov-wasserstein averaging of kernel and distance matrices. In *International conference on machine learning*, 2664–2672 (PMLR, 2016).

108. Cuturi, M. Sinkhorn distances: Lightspeed computation of optimal transport. *Adv. neural information processing systems* **26** (2013).

109. Crouse, D. F. On implementing 2d rectangular assignment algorithms. *IEEE Transactions on Aerosp. Electron. Syst.* **52**, 1679–1696 (2016).

110. Camacho, D. M., Collins, K. M., Powers, R. K., Costello, J. C. & Collins, J. J. Next-generation machine learning for biological networks. *Cell* **174**, 1571–1582 (2018).

111. Lundberg, S. M. & Lee, S.-I. A unified approach to interpreting model predictions. *Adv. neural information processing systems* **30** (2017).

112. Schaum, N. *et al.* Single-cell transcriptomics of 20 mouse organs creates a tabula muris. *Nature* **562**, 367–372 (2018).

113. Yang, Z., Kotoge, R., Piao, X., Liu, J. & Hamamoto, R. MLOmics: Cancer Multi-Omics Database for Machine Learning. *Sci. Data* **12**, 913 (2025).

114. Elmarakeby, H. *et al.* Biologically informed deep neural network for prostate cancer classification and discovery. *Nature* **598**, 348–352 (2021).

## **Supporting Information**

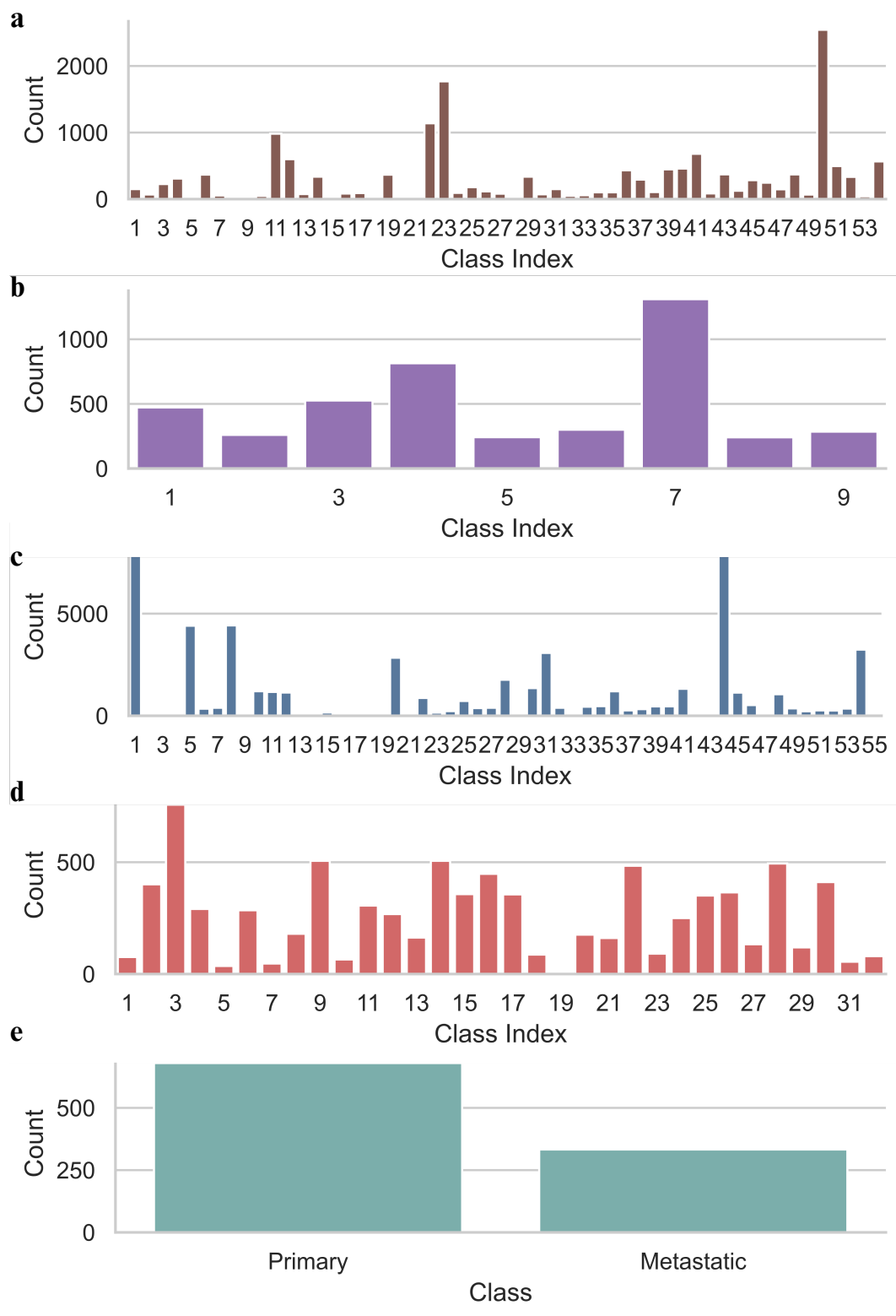


**Figure S1.** Class Distribution of different datasets of this study. **a.** PP-Pathways (see Table S1 for class names) **b.** HuRI (see Table S2 for class names) **c.** Tabula Muris (see Table S4 for class names) **d.** Pan Cancer (Please )see Table S9 for class names. **e.** Prostate Cancer.

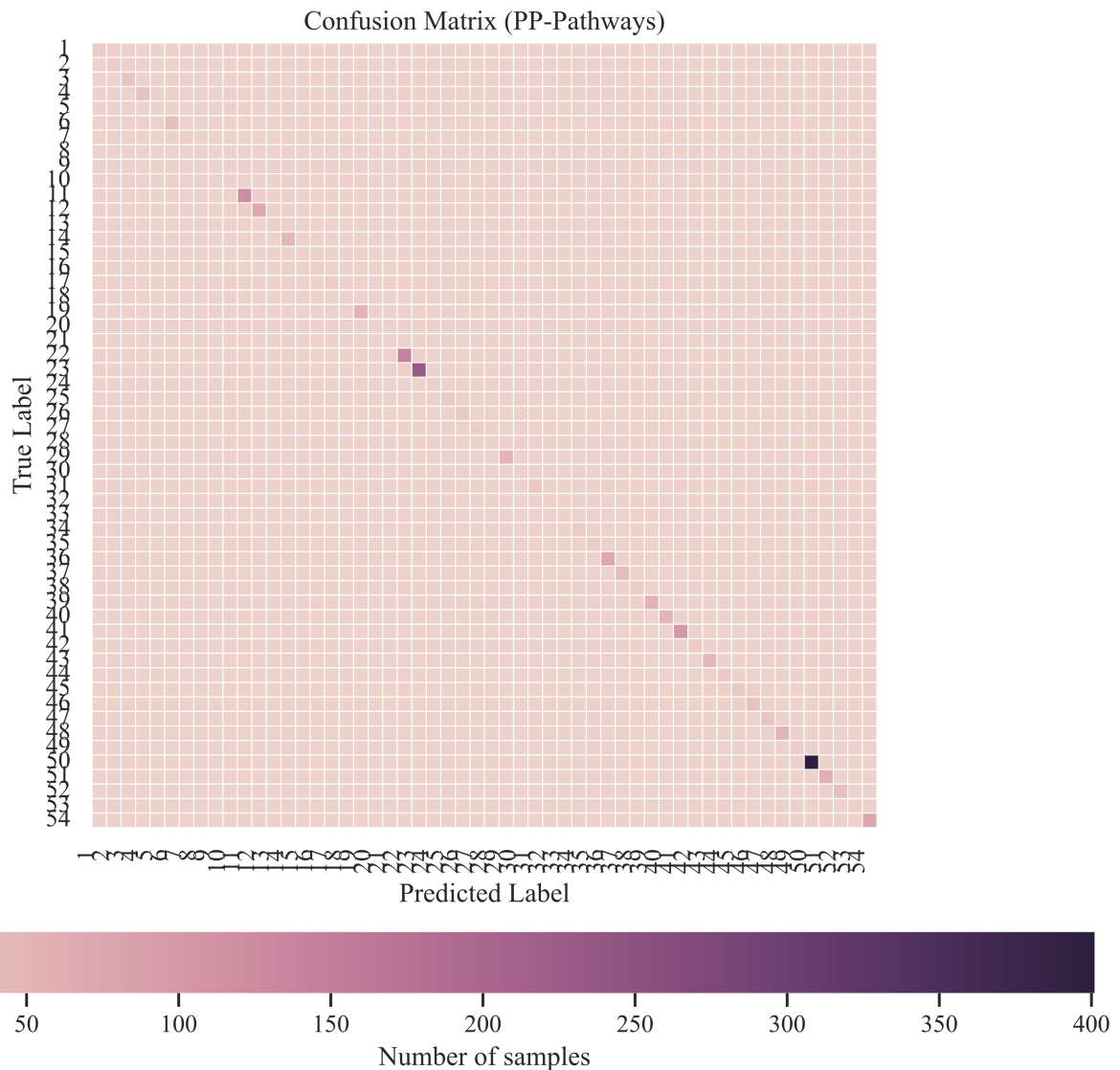


**Figure S2.** PP-Pathways confusion matrix. Confusion matrix of Graph2Image predictions across 54 cell types with counts shown on a logarithmic colour scale. The prominent diagonal and sparse off-diagonal entries indicate high per-class accuracy with limited cross-class confusion. Class indices and names follow Supplementary Table [S4](#).

**Table S1.** GTEx tissue classes for the PP-Pathways dataset

Index	Tissue name
1	Adipose – Subcutaneous
2	Adipose – Visceral (Omentum)
3	Adrenal Gland
4	Artery – Aorta
5	Artery – Coronary
6	Artery – Tibial
7	Bladder
8	Brain – Amygdala
9	Brain – Anterior cingulate cortex (BA24)
10	Brain – Caudate (basal ganglia)
11	Brain – Cerebellar Hemisphere
12	Brain – Cerebellum
13	Brain – Cortex
14	Brain – Frontal Cortex (BA9)
15	Brain – Hippocampus
16	Brain – Hypothalamus
17	Brain – Nucleus accumbens (basal ganglia)
18	Brain – Putamen (basal ganglia)
19	Brain – Spinal cord (cervical c-1)
20	Brain – Substantia nigra
21	Breast – Mammary Tissue
22	Cells – Cultured fibroblasts
23	Cells – EBV-transformed lymphocytes
24	Cervix – Ectocervix
25	Cervix – Endocervix
26	Colon – Sigmoid
27	Colon – Transverse
28	Esophagus – Gastroesophageal Junction
29	Esophagus – Mucosa
30	Esophagus – Muscularis
31	Fallopian Tube
32	Heart – Atrial Appendage
33	Heart – Left Ventricle
34	Kidney – Cortex
35	Kidney – Medulla
36	Liver
37	Lung
38	Minor Salivary Gland
39	Muscle – Skeletal
40	Nerve – Tibial
41	Ovary
42	Pancreas
43	Pituitary
44	Prostate
45	Skin – Not Sun Exposed (Suprapubic)
46	Skin – Sun Exposed (Lower leg)
47	Small Intestine – Terminal Ileum
48	Spleen
49	Stomach
50	Testis
51	Thyroid
52	Uterus
53	Vagina
54	Whole Blood

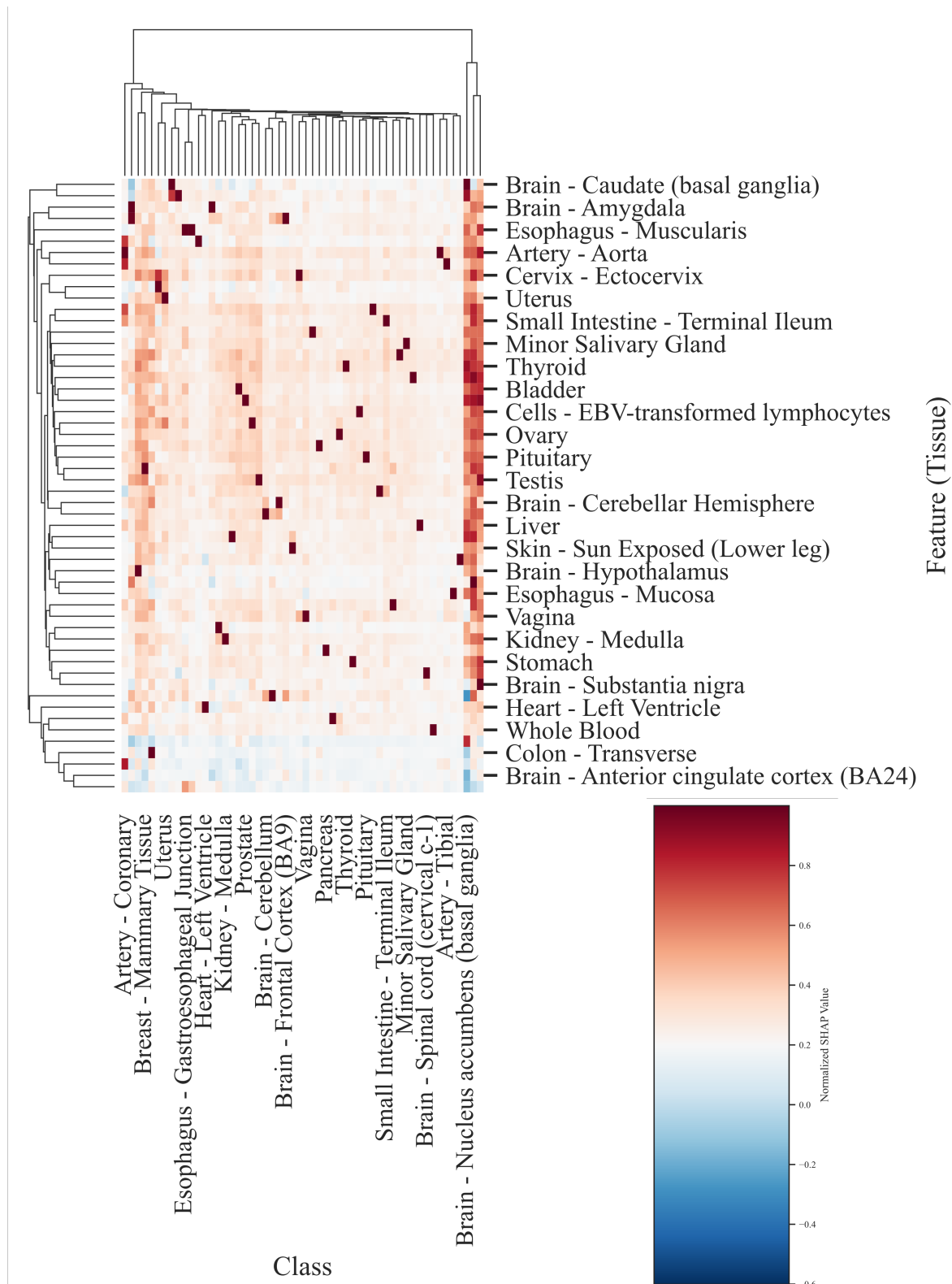


**Figure S3.** Clustered SHAP heatmap revealing tissue-level feature importance structure in the PP-Pathways dataset. Clustered heatmap showing normalized SHAP values for the top positively and negatively influential tissues across all PP-Pathways classes. Hierarchical clustering on both tissues (rows) and classes (columns) highlights coherent blocks of shared feature-importance structure. Brain-related tissues form several tight subclusters, reflecting shared expression patterns across related neuroanatomical regions, whereas digestive, reproductive, endocrine, and vascular tissues display distinct SHAP signatures. Columns correspond to PP-Pathways classes, and rows correspond to tissues selected by class-specific SHAP ranking. Color intensity indicates the normalized SHAP magnitude, with red denoting strong positive contributions and blue denoting strong negative contributions. The dual dendrogram structure provides an interpretable overview of how different tissues contribute to Graph2Image model predictions and reveals biologically meaningful relationships among tissue-specific expression profiles.

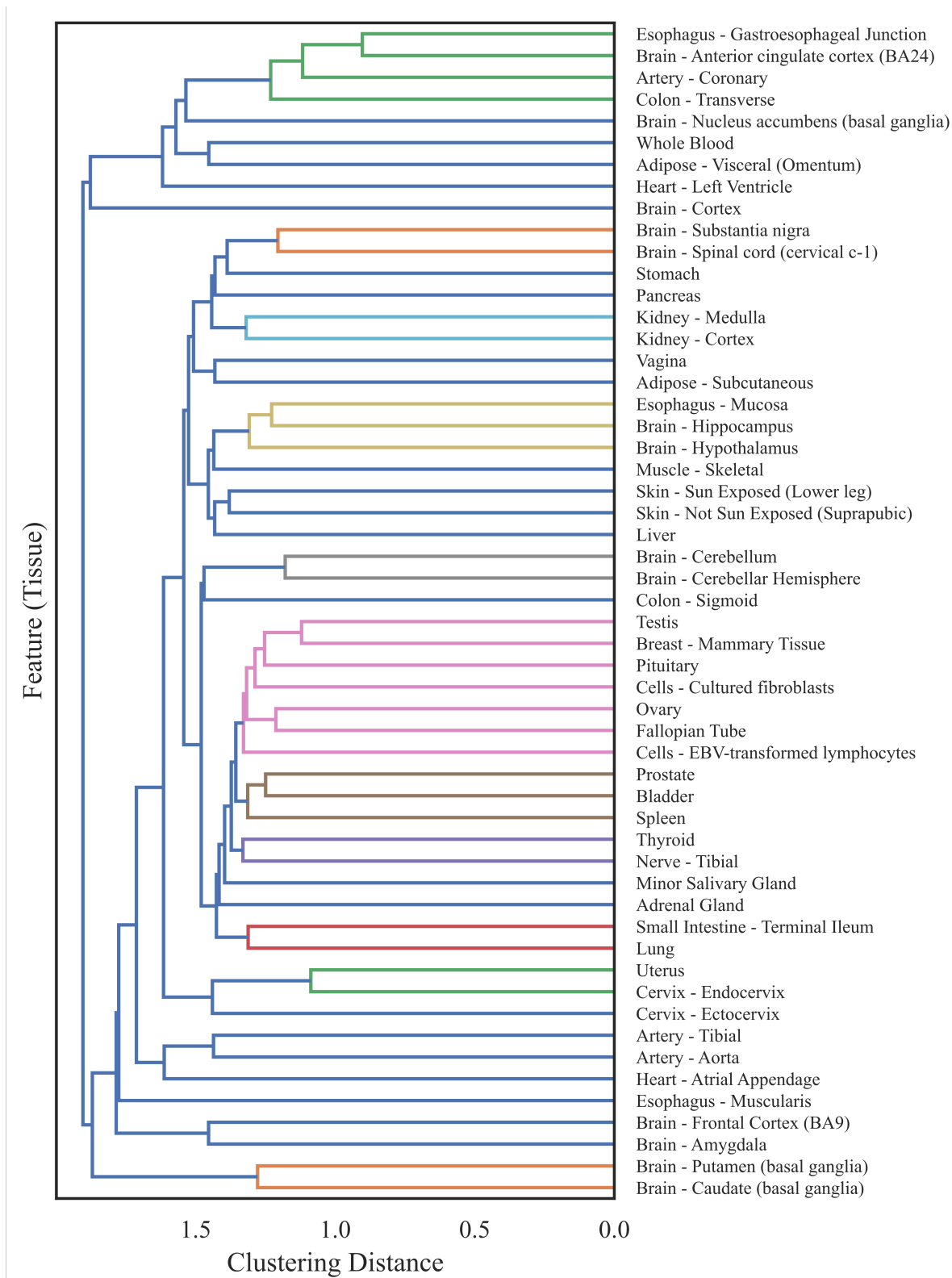


**Figure S4.** Hierarchical clustering of tissue-level SHAP importance profiles in the PP-Pathways dataset. Dendrogram showing the hierarchical relationships among tissues based on their normalized SHAP value profiles across all PP-Pathways classes. Each branch represents a tissue whose SHAP contribution reflects its discriminative importance for class-specific Graph2Image patterns. Tissues with similar SHAP signatures cluster together, revealing shared regulatory or expression landscapes, e.g., anatomically related brain regions and gastrointestinal tissues form coherent subtrees. The clustering is computed using average linkage and Euclidean distance on the top SHAP-ranked features per class. This analysis highlights interpretable groupings of functionally related tissues and provides a global view of how distinct anatomical systems contribute to Graph2Image model predictions.

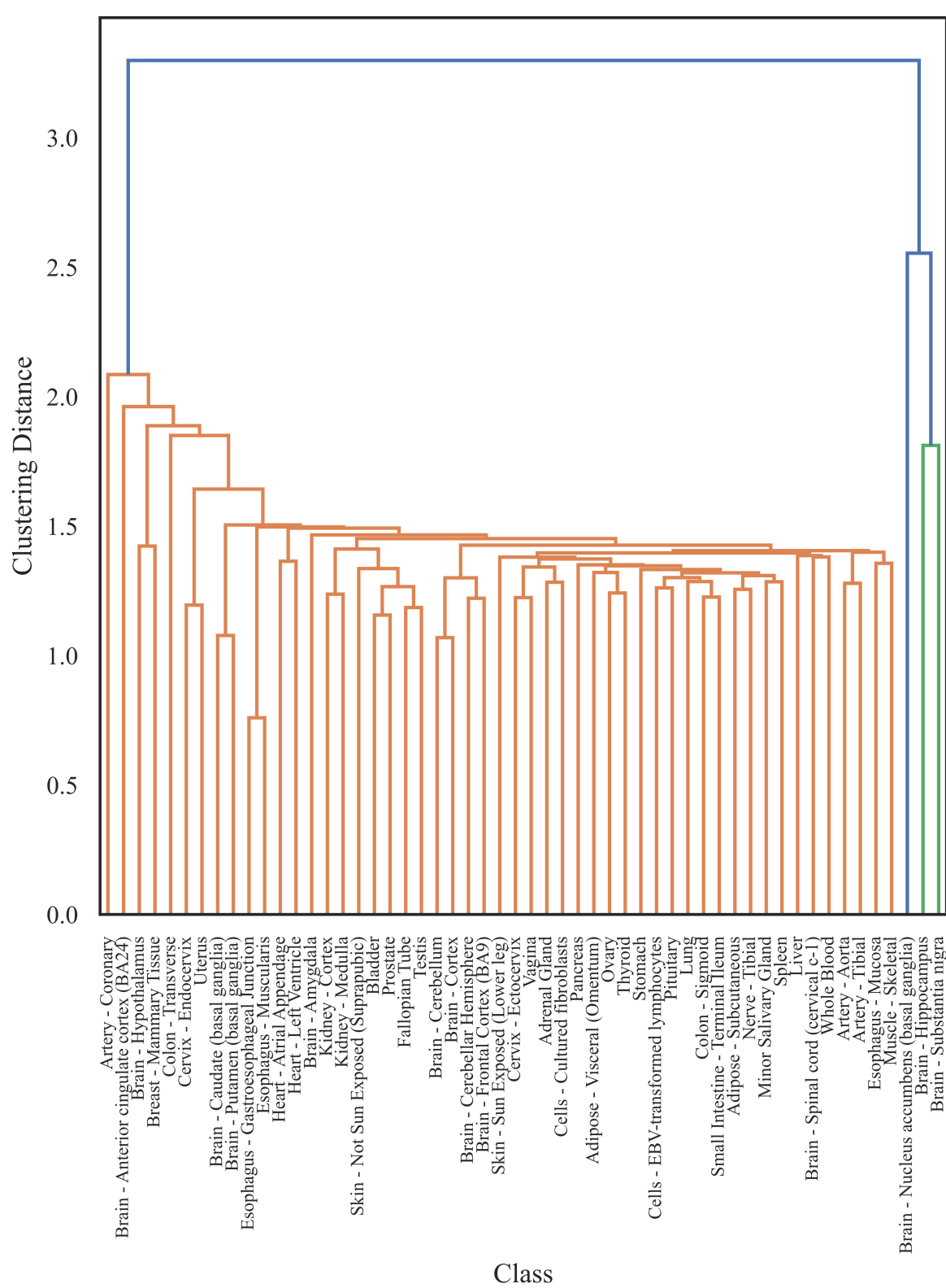


**Figure S5.** Hierarchical clustering of PP-Pathways classes based on normalized SHAP importance profiles. Dendrogram illustrating the hierarchical relationships among PP-Pathways classes derived from their normalized SHAP feature-importance signatures. Each leaf corresponds to a tissue class, and branch structure reflects similarity in the SHAP contribution patterns that drive Graph2Image predictions. Closely clustered tissues show highly similar SHAP profiles, revealing biologically coherent groupings, e.g., related brain regions cluster tightly, while immune-associated and gastrointestinal tissues form distinct subtrees. Clustering was performed using average linkage and Euclidean distance on SHAP-selected top features. This visualization provides a global view of class-level similarity in model-derived tissue importance patterns.

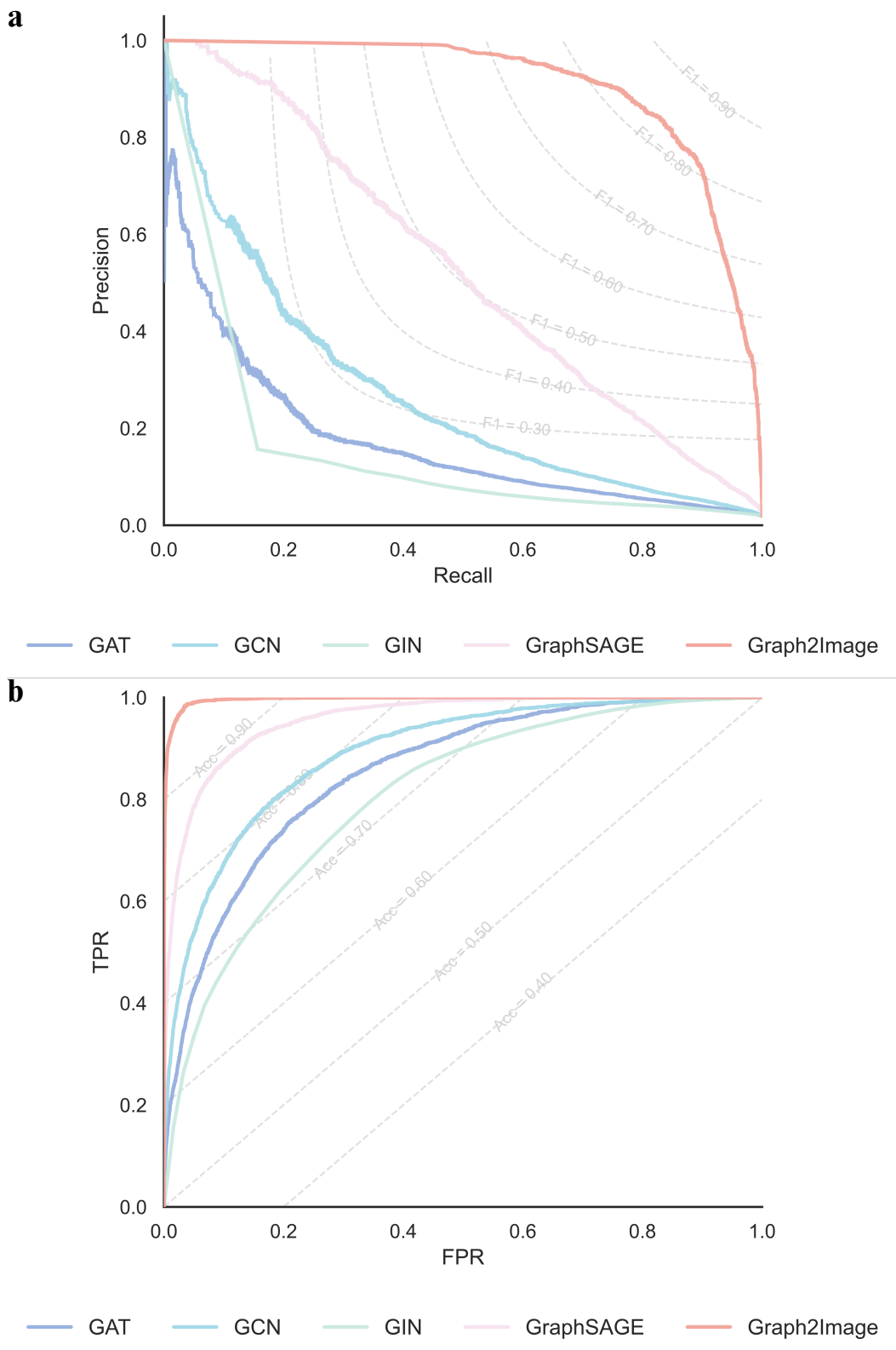


**Figure S6.** Precision-recall and ROC performance of Graph2Image versus GNN baselines on the PP-Pathways dataset. a, Macro-averaged precision-recall curves for Graph2Image and graph neural network baselines (GCN, GAT, GIN, and GraphSAGE). Dashed curves denote F1 contours. Graph2Image achieves substantially higher precision across the full recall range, reflecting stronger discrimination between tissue classes in the PP-Pathways dataset. b, ROC curves for the same models. Dashed lines indicate AUC contours. Graph2Image approaches near-perfect sensitivity across false-positive rates, outperforming all GNN baselines. Together, these results highlight the superior separability of Graph2Image embeddings for complex multi-tissue expression signatures.

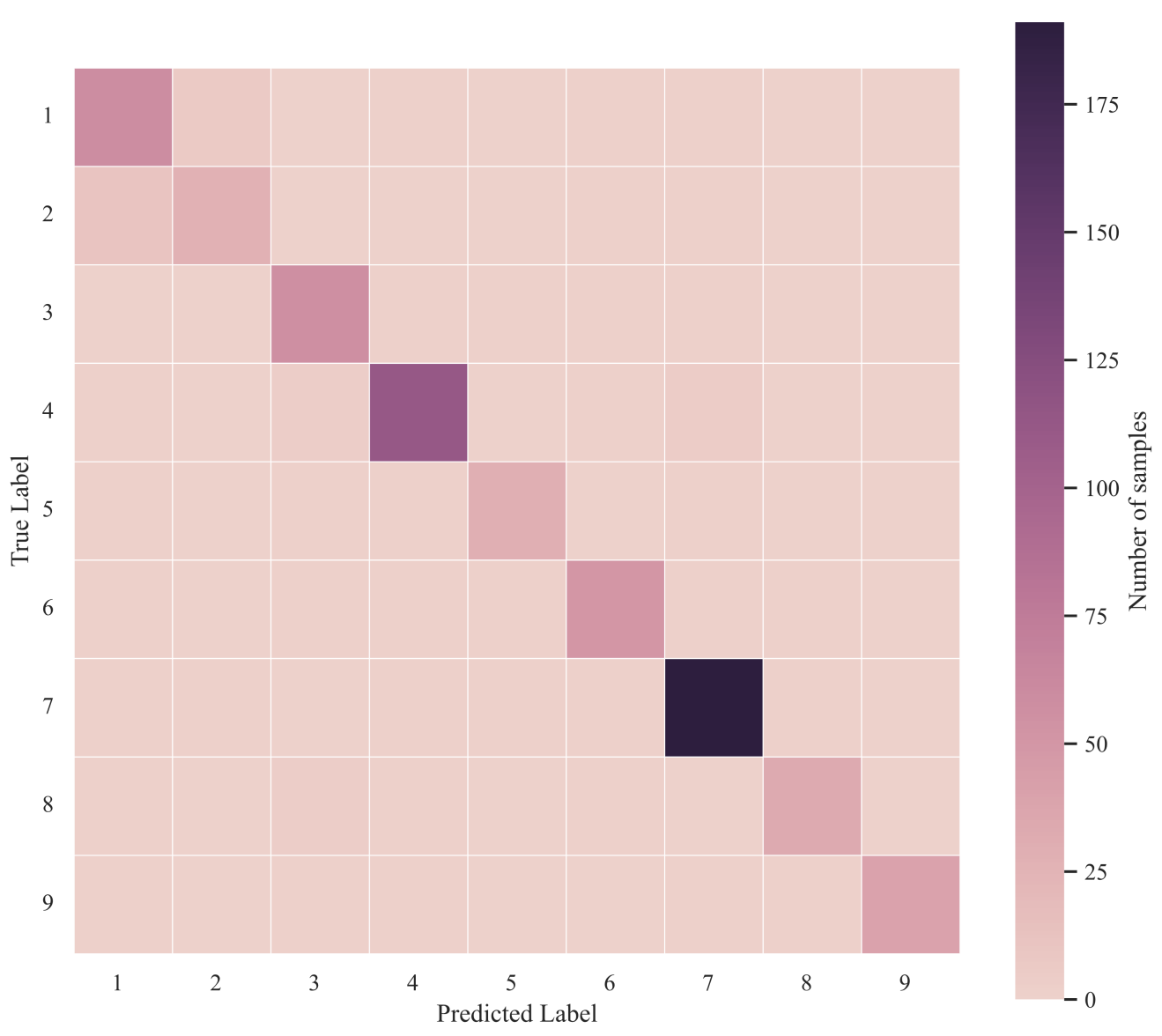


**Figure S7.** Confusion matrix for Graph2Image predictions on the HuRI dataset. Confusion matrix showing classification performance across the nine GTEx-derived tissue classes in the HuRI protein–protein interaction dataset. Graph2Image exhibits strong diagonal dominance, indicating highly accurate tissue-of-origin prediction from gene-level embeddings. Off-diagonal values are minimal across all classes, demonstrating that tissues with distinct expression signatures, i.e., Thyroid, Muscle, Testis and Whole Blood are cleanly separated by the model. Color intensity reflects the number of samples assigned to each true–predicted label pair. Class indices and names follow Supplementary Table S2.

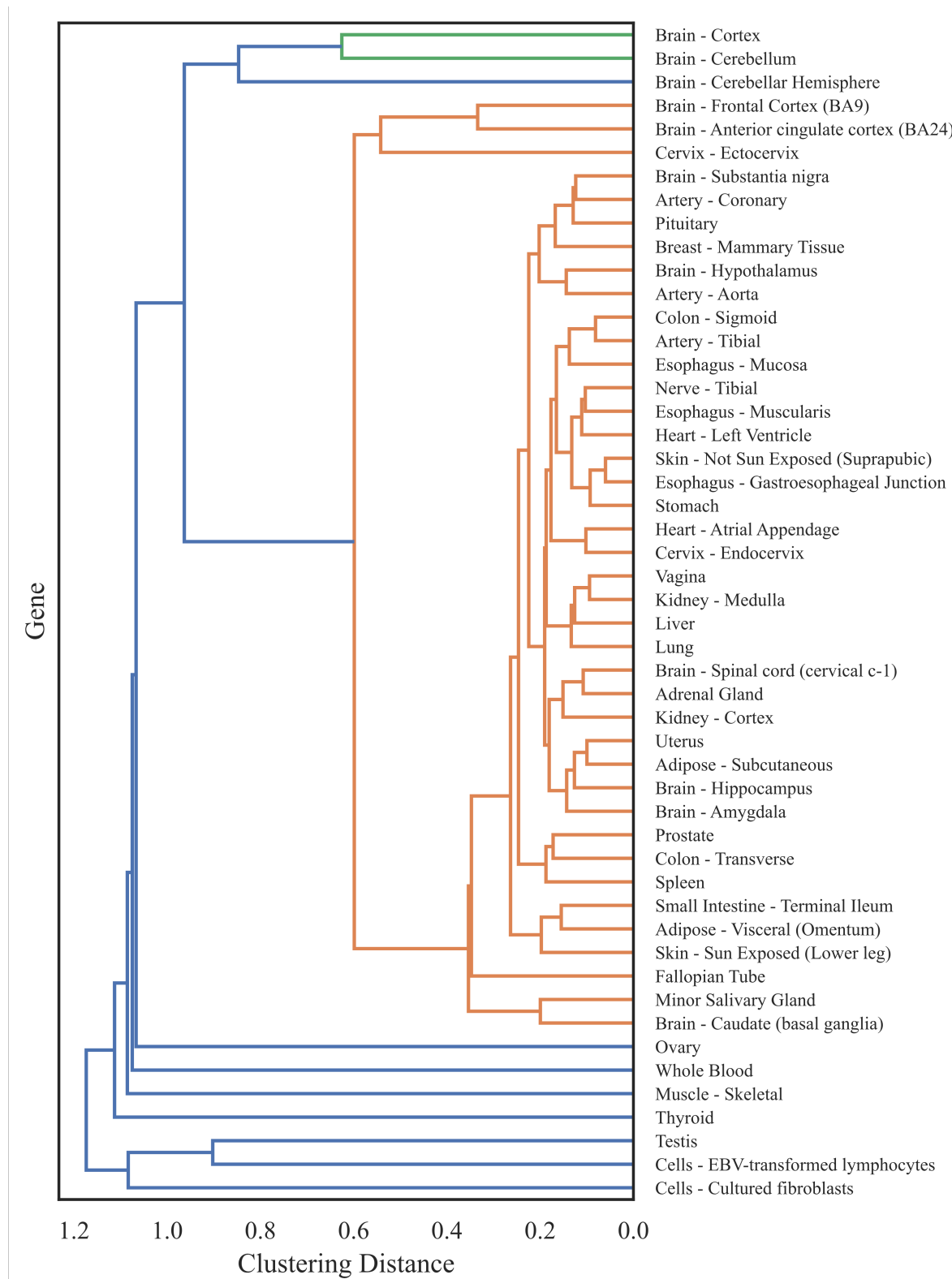


**Figure S8.** Hierarchical clustering of tissue-level SHAP feature importance in the HuRI dataset. Dendrogram showing the hierarchical relationships among GTEx tissue features based on their normalized SHAP importance profiles for the HuRI Graph2Image classifier. Each leaf corresponds to a tissue whose SHAP values summarize how strongly that feature contributes to distinguishing the nine HuRI tissue classes. Closely related tissues, such as multiple cortical and cerebellar brain regions or adipose and skin tissues, form coherent subclusters, whereas immune, endocrine and gastrointestinal tissues separate into distinct branches. Distances were computed from SHAP-derived importance vectors using Euclidean distance with average-linkage agglomeration. This analysis indicates that the model's feature attributions recover biologically meaningful similarity structure among tissues in the HuRI dataset. **31/65**

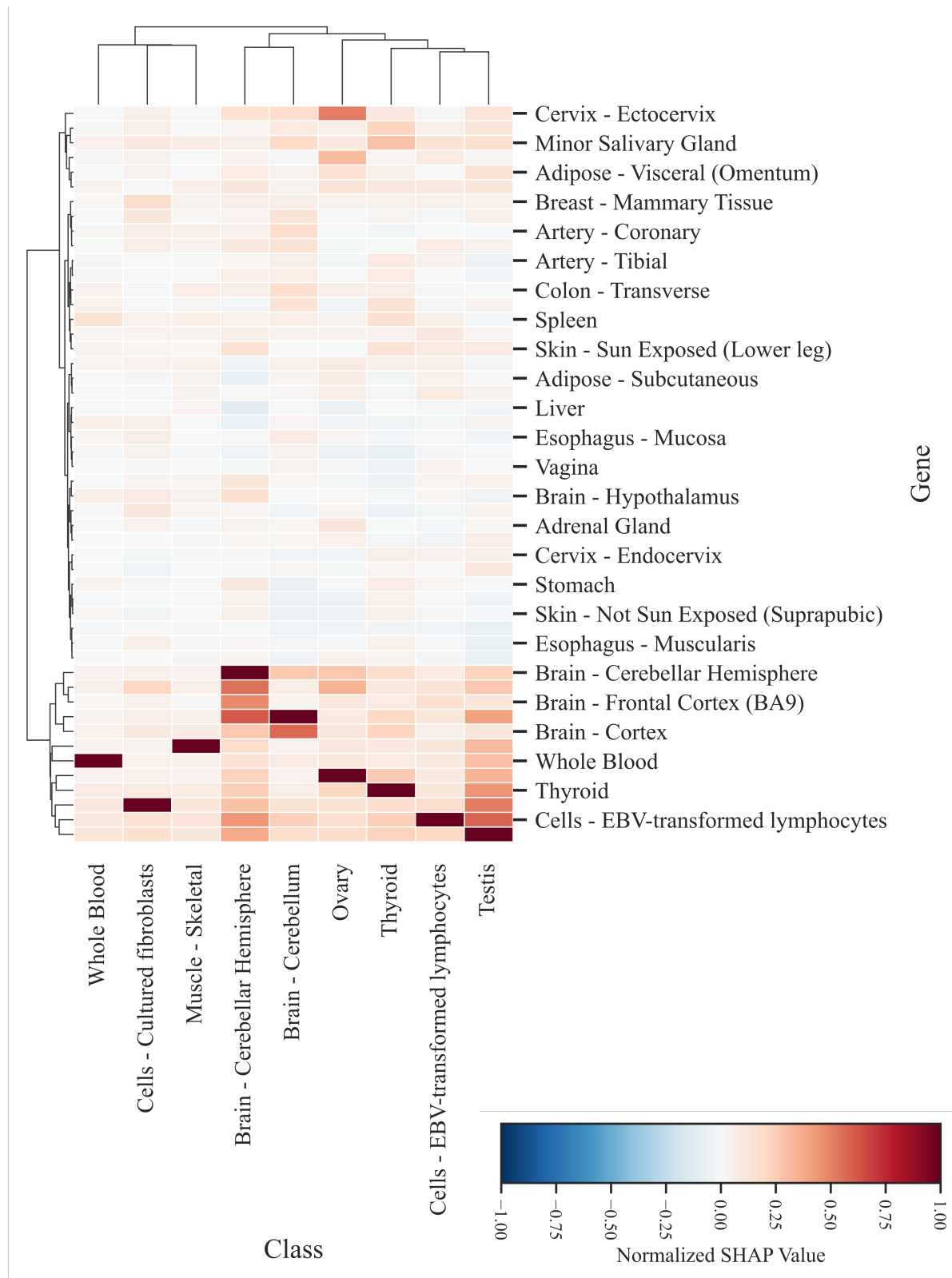


**Figure S9.** SHAP-based interpretation of Graph2Image predictions on the HuRI interactome. Hierarchically clustered heatmap showing the normalized SHAP values for the top predictive genes across the nine GTEx tissues represented in the HuRI-GTEx joint dataset. Rows denote genes selected based on the highest absolute class-specific SHAP contributions, and columns correspond to HuRI tissue classes. Positive SHAP values (red) indicate features that strongly drive the model toward a given tissue prediction, whereas negative values (blue) represent features that oppose that prediction. Dendrograms along both axes reveal that Graph2Image uncovers biologically meaningful co-regulation structure, grouping related tissues (e.g., brain tissues and immune-derived cell types) and clustering coherent gene sets associated with tissue-specific expression programs. The scale bar represents normalized SHAP values.

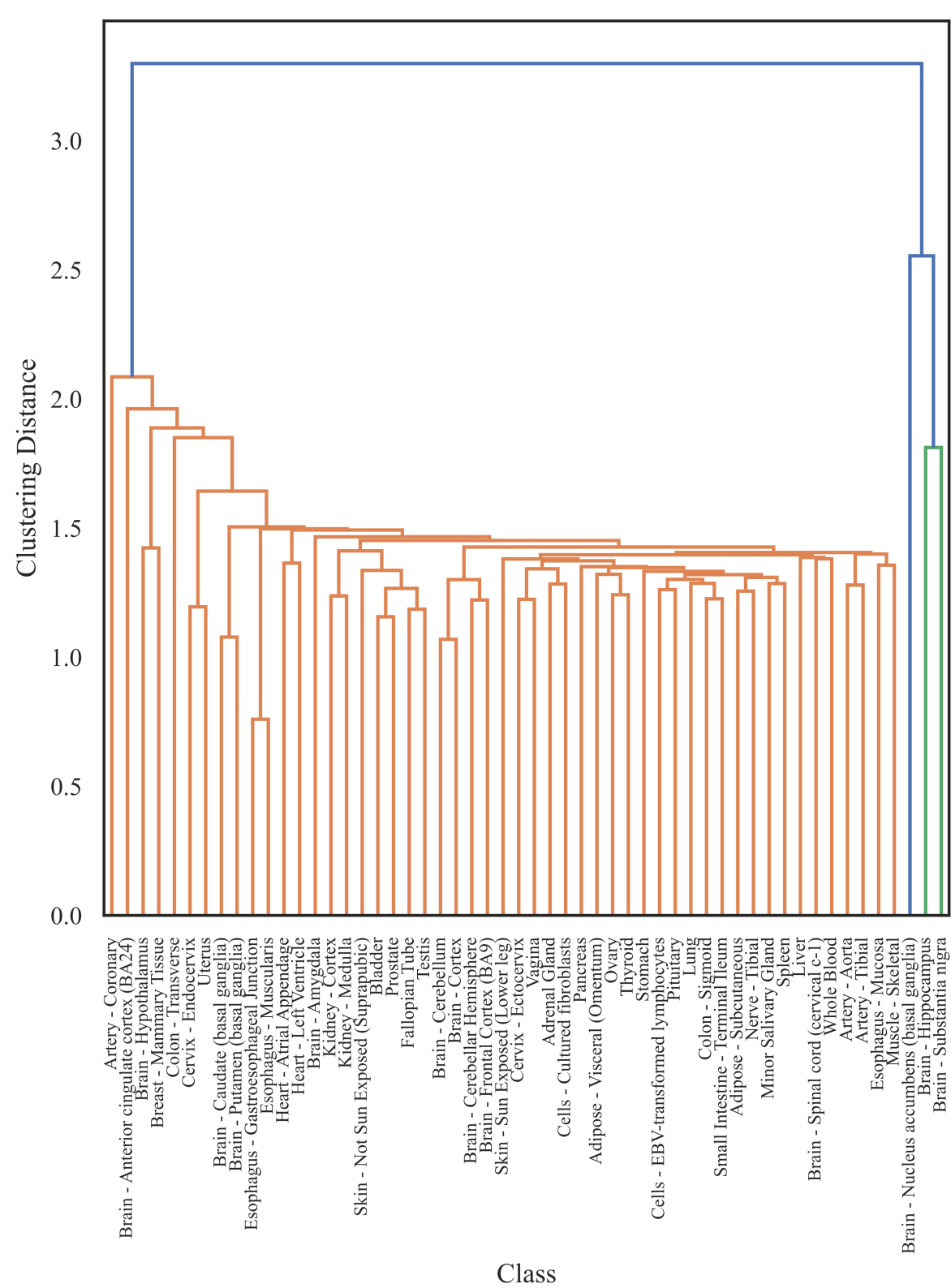


**Figure S10.** Hierarchical clustering of tissue-specific SHAP profiles in the HuRI interactome. Dendrogram showing hierarchical clustering of the nine HuRI tissue classes based on their normalized SHAP importance profiles derived from Graph2Image embeddings. Distances reflect similarity in feature attribution patterns across tissues, revealing biologically meaningful groupings such as the close proximity of brain regions (Cerebellum and Cerebellar Hemisphere), immune-related cell types (EBV-transformed lymphocytes and cultured fibroblasts), and reproductive tissues (Ovary and Testis). Clustering was performed using average linkage and Euclidean distance.

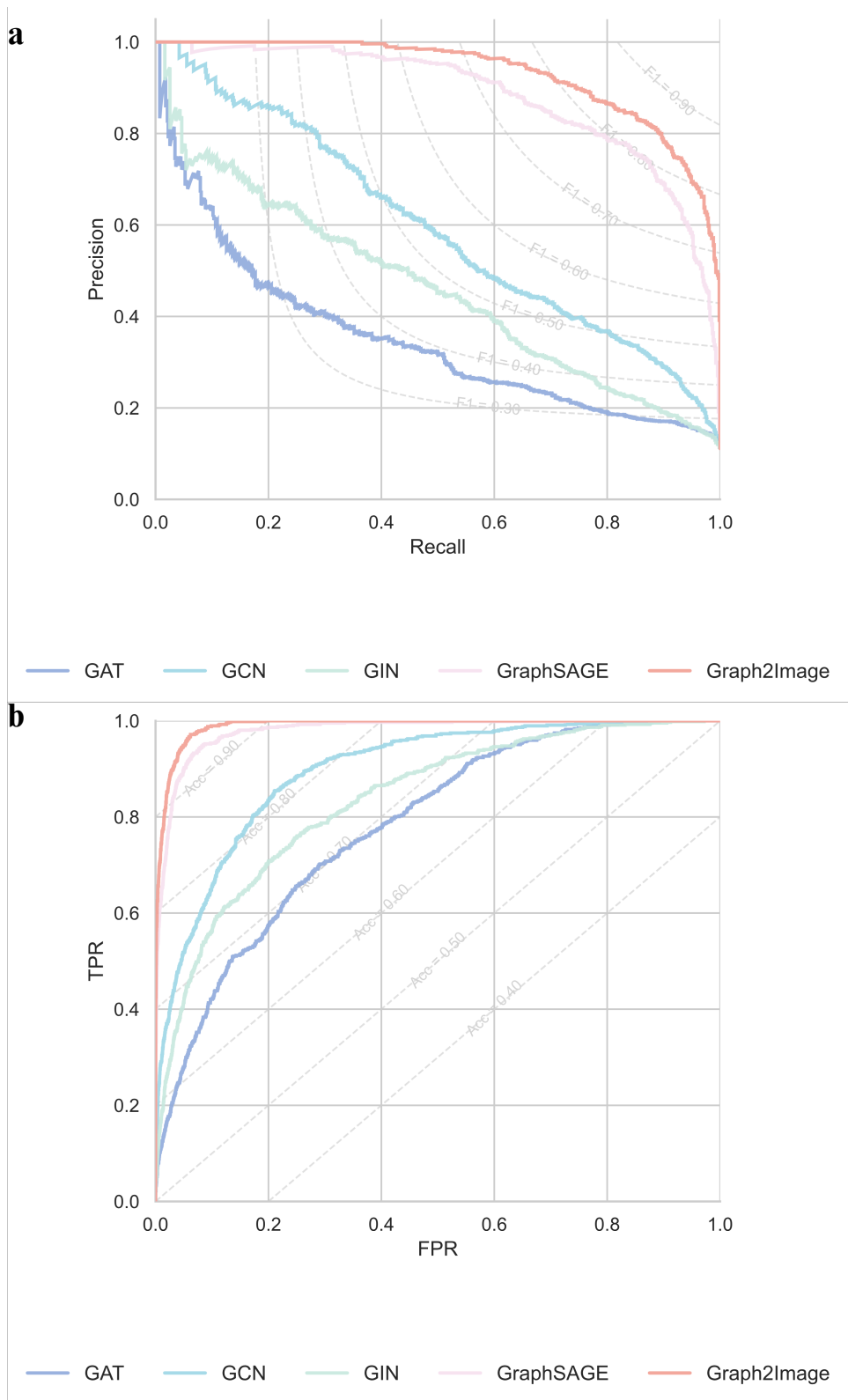


**Figure S11.** Performance comparison of Graph2Image and graph neural network baselines on the HuRI interactome. a, Micro-averaged precision–recall curves for Graph2Image and baseline GNNs (GCN, GAT, GIN, GraphSAGE) on the nine-class HuRI tissue classification task. Graph2Image achieves consistently higher precision across the full recall range, indicating stronger discriminative ability in this sparse interactome setting. b, ROC curves showing that Graph2Image attains markedly higher true-positive rates at low false-positive rates, reflecting improved sensitivity. Dashed lines denote F1 (panel a) and AUROC (panel b) reference contours for visual calibration.

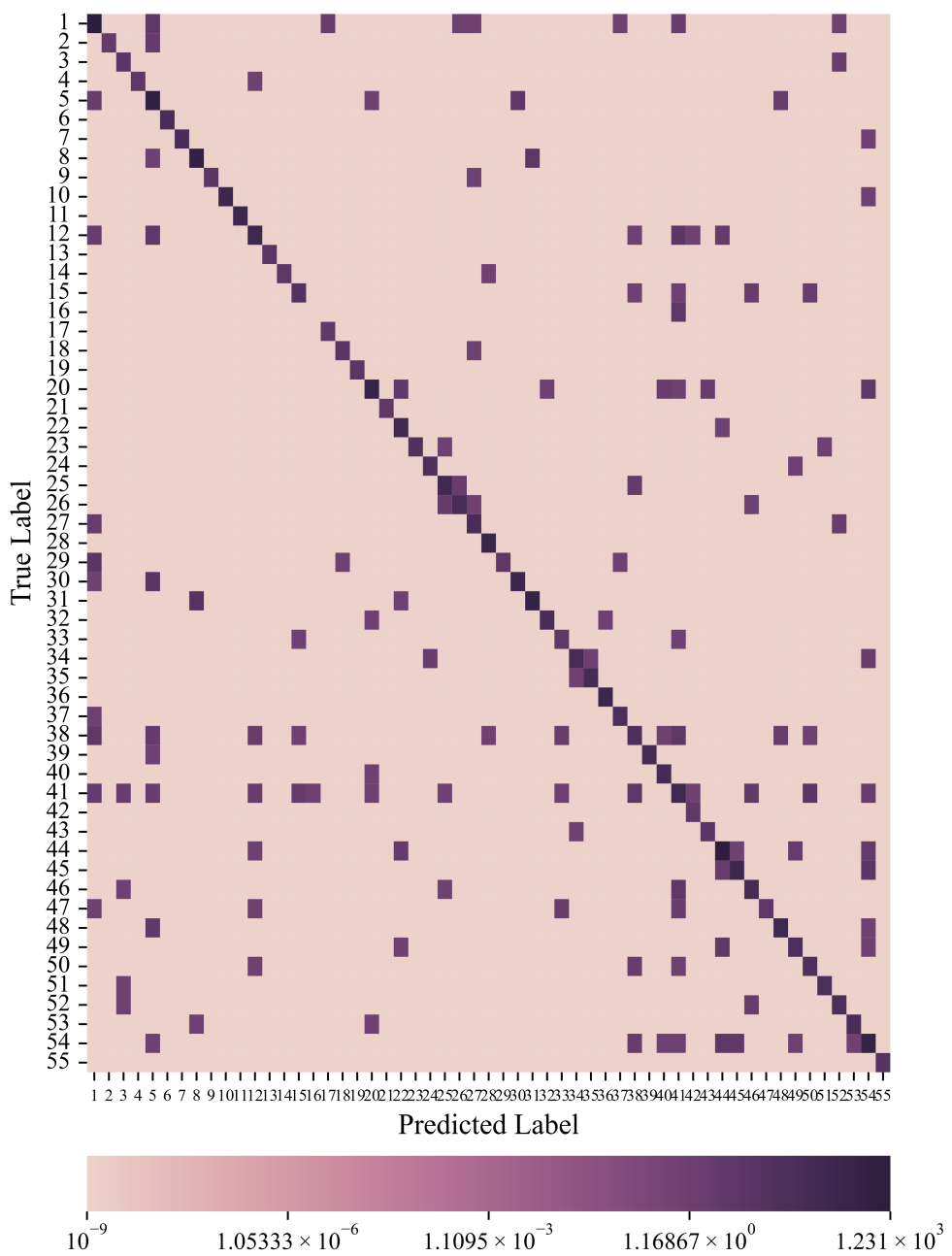


**Figure S12.** Tabula Muris confusion matrix. Confusion matrix of Graph2Image predictions across 55 cell types with counts shown on a logarithmic colour scale. The prominent diagonal and sparse off-diagonal entries indicate high per-class accuracy with limited cross-class confusion. Class indices and names follow Supplementary Table S4.

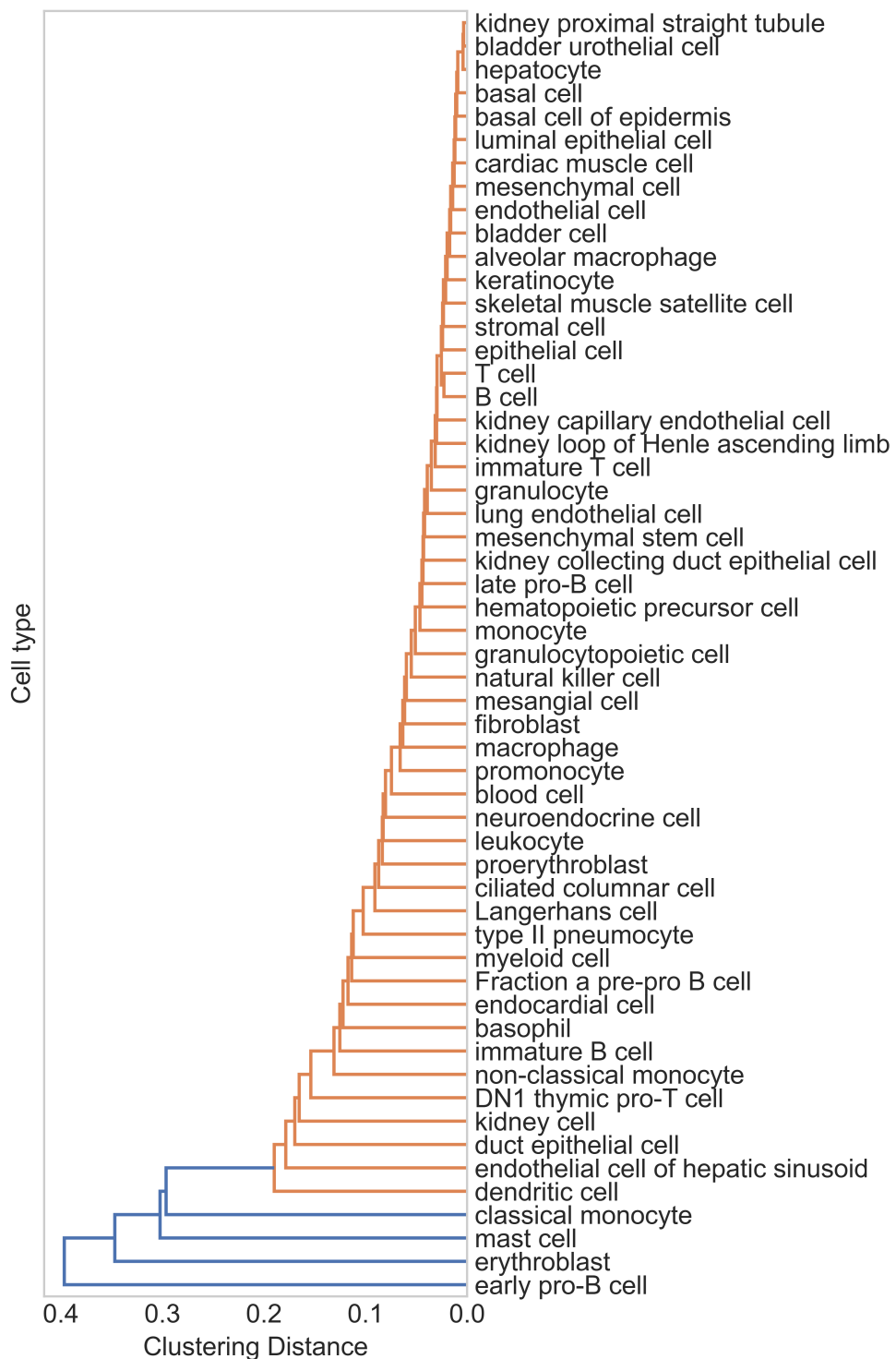


**Figure S13.** Tabula Muris dendrogram from SHAP profiles. Hierarchical clustering of the 55 cell types using class-averaged, gene-level SHAP profiles (average-linkage, Euclidean distance). The branching recapitulates expected haematopoietic and epithelial lineages and reveals coherent groupings discussed in the main text.

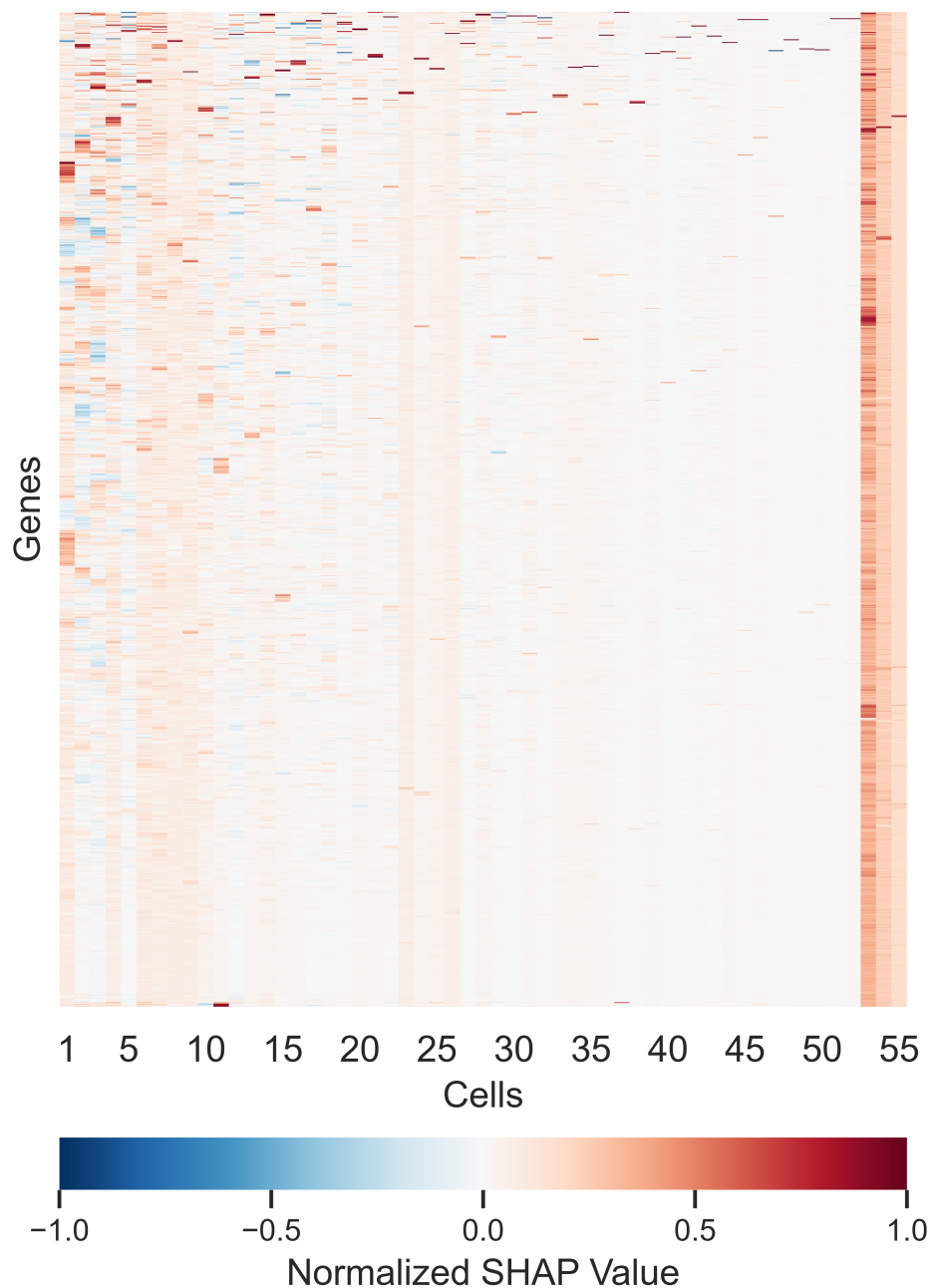


**Figure S14.** Tabula Muris class-averaged SHAP heatmap. Heatmap of class-averaged SHAP values for top marker genes across all 55 cell types. SHAP values are normalised within each class to the maximum absolute value; warm colours denote features increasing class probability and cool colours the converse. Gene names are listed in Supplementary Table S5, S6, and S7; cell-type labels follow Supplementary Table S4.

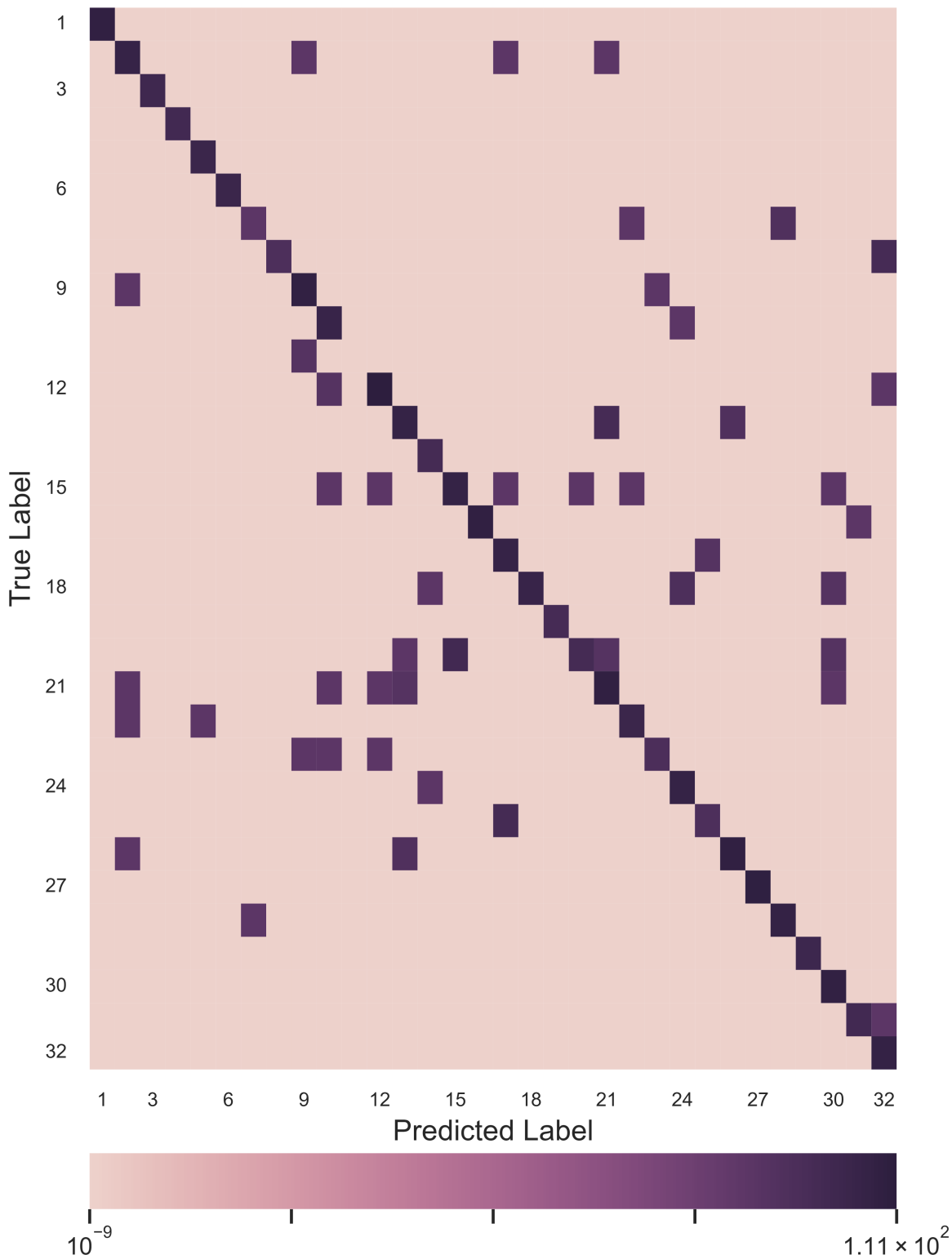


**Figure S15.** Pan-cancer confusion matrix. Confusion matrix of Graph2Image predictions across 32 TCGA cancer types with a logarithmic colour scale. The strong diagonal highlights accurate class assignment, while rare off-diagonal entries capture confusions among related tissues. Cancer-type names and order follow Supplementary Table S9.

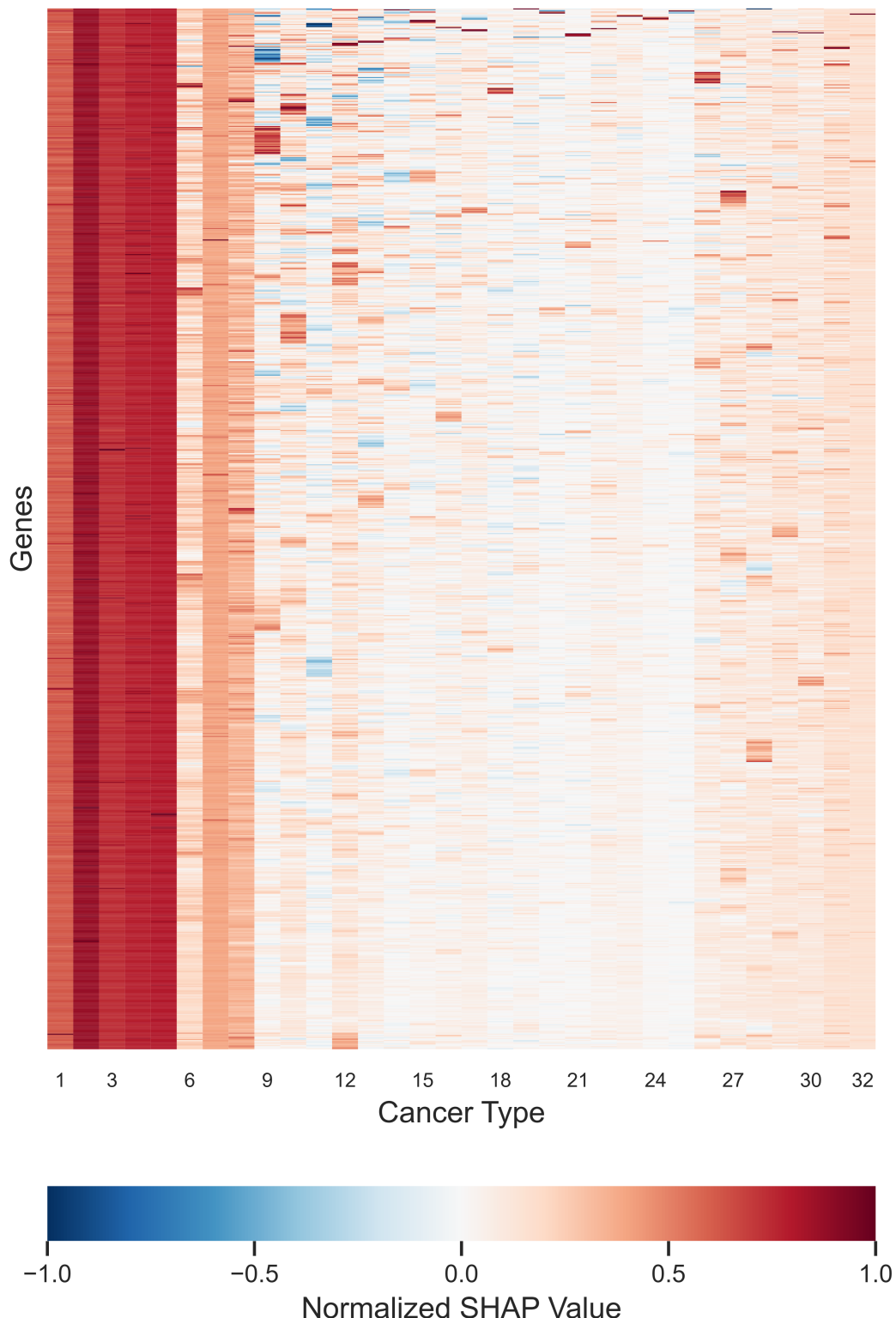


**Figure S16.** Pan-cancer class-averaged SHAP heatmap. Heatmap of class-averaged SHAP values for mRNA features across 32 cancer types, normalised within class ( $\max |\text{SHAP}| = 1$ ). Distinct blocks reflect shared transcriptional programmes and cancer-type-specific signatures described in the main text. Gene names are provided in Supplementary Table S10 and S11; labels follow Supplementary Table S9.

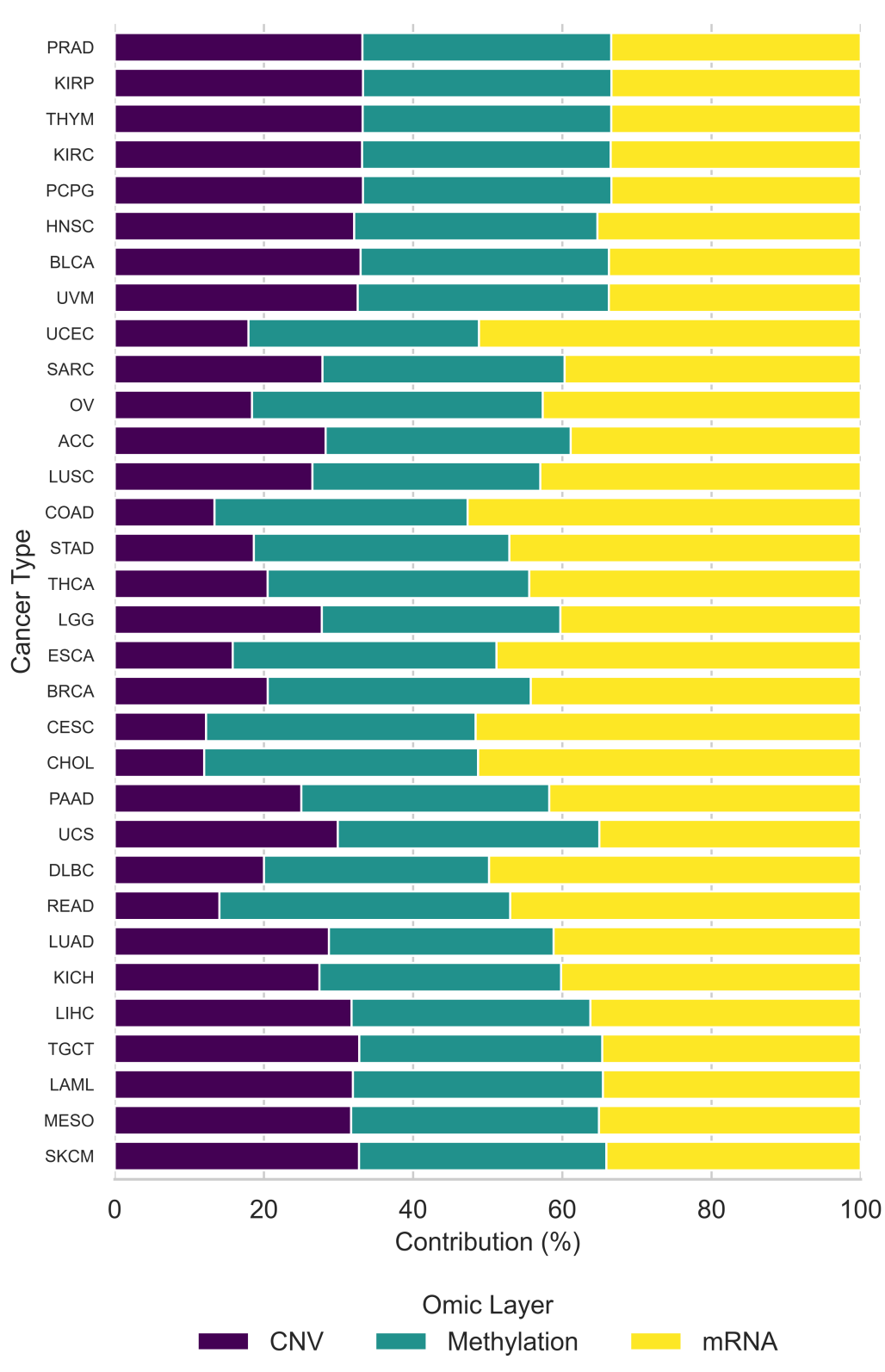


**Figure S17.** Relative contribution of omics modalities. Per-class mean absolute SHAP partitioned by mRNA, copy-number variation (CNV) and DNA methylation for each cancer type. Modality usage mirrors tissue of origin and known driver biology. Cancer-type order matches Supplementary Table S9.

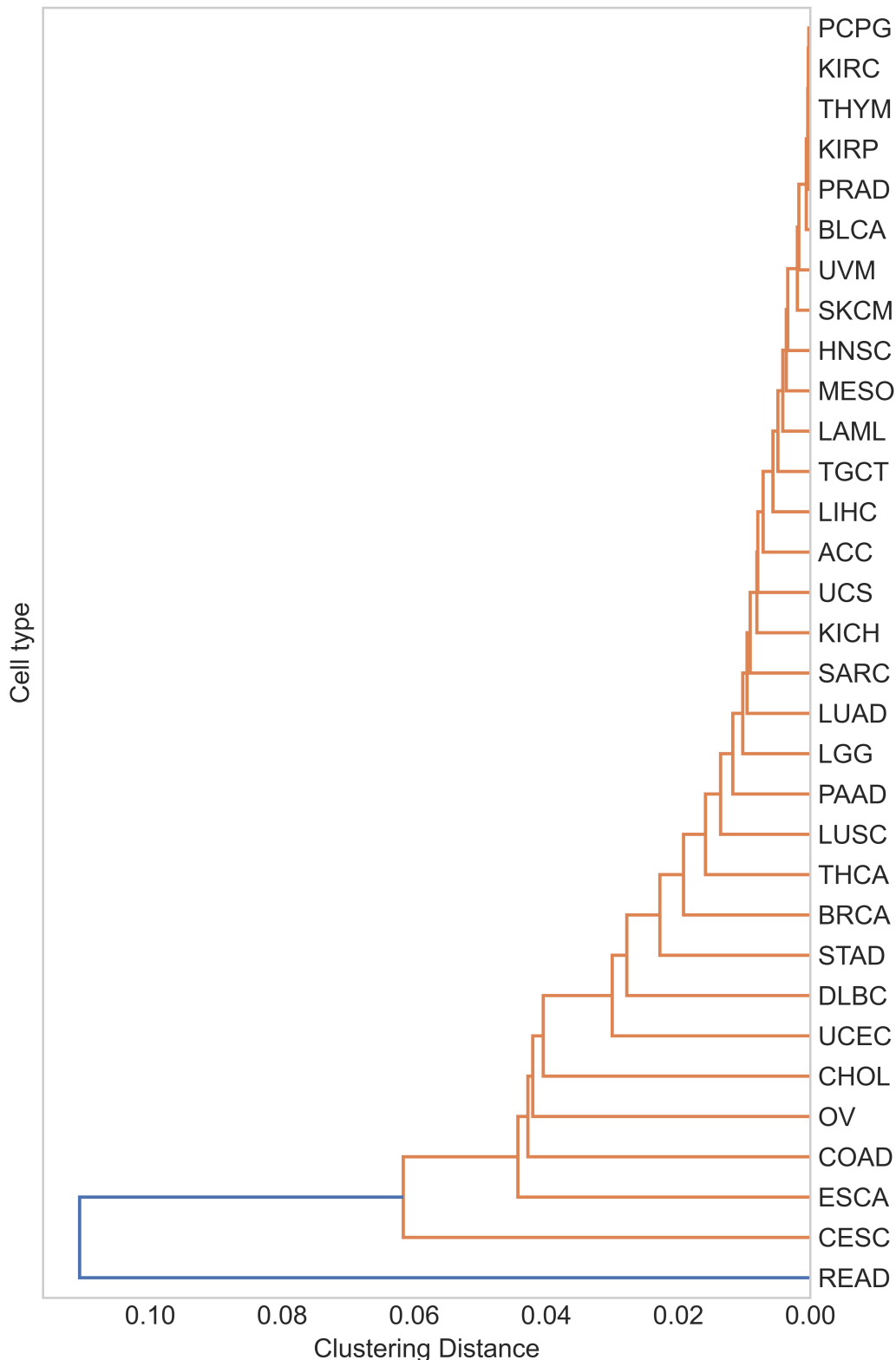


**Figure S18.** Pan-cancer dendrogram from SHAP profiles. Hierarchical clustering of 32 cancer types using class-level SHAP profiles (average-linkage, Euclidean distance). The arrangement groups tumours with shared molecular programmes and anatomical origin; salient clades are discussed in the main text.



**Figure S19.** 'Butterfly' plots of gene-level SHAP in prostate cancer. Mirrored kernel-density estimates of SHAP distributions for selected genes in primary versus metastatic tumours highlight features that preferentially drive each state. Genes are ordered by cohort-wide importance.

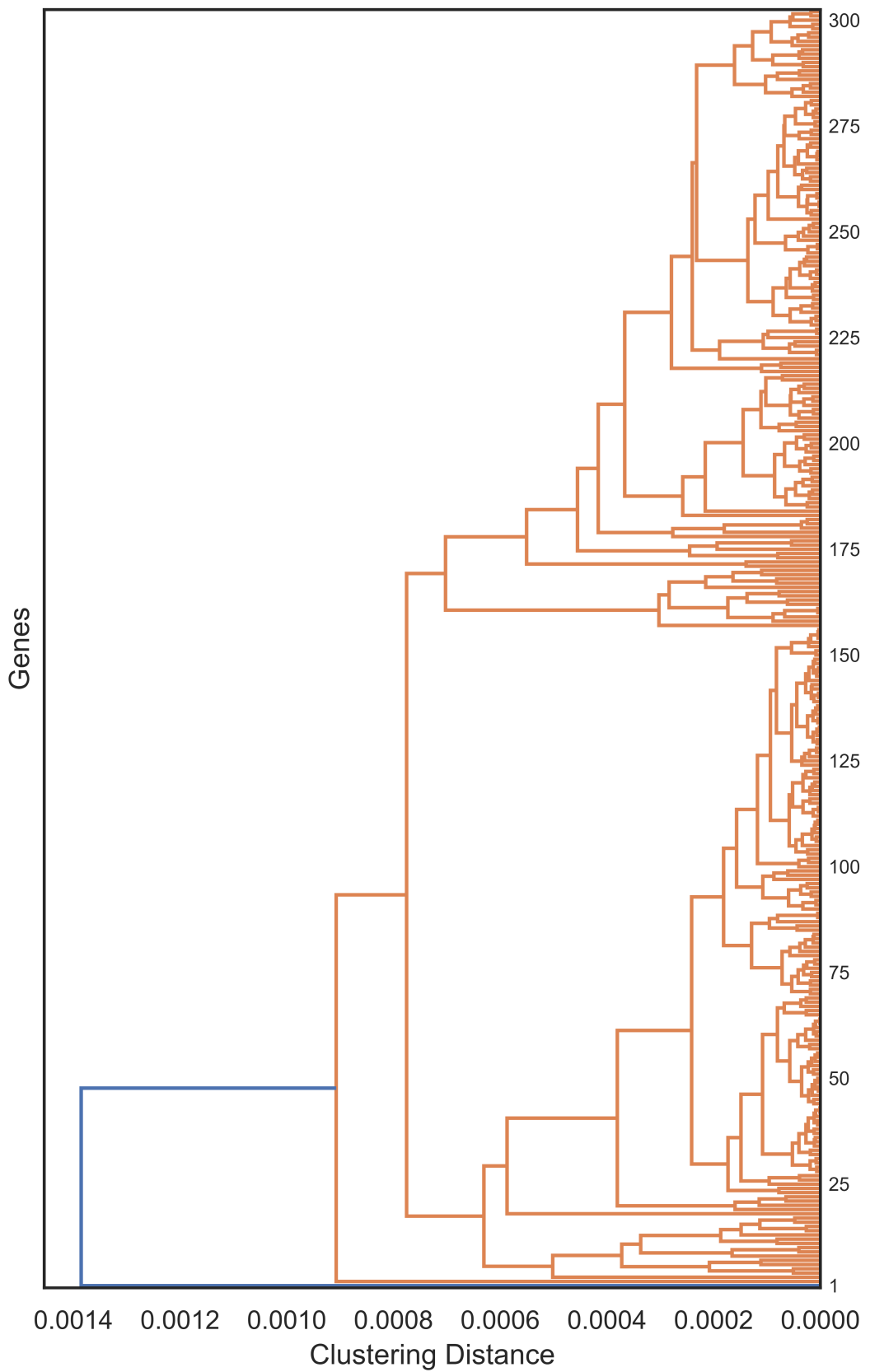


**Figure S20.** Prostate cancer gene dendrogram from SHAP profiles. Average-linkage clustering (Euclidean distance) of top predictive genes using their SHAP profiles across samples identifies modules associated with primary or metastatic disease states. Gene names are the supplementary Table S12.

**Table S2.** GTEx tissue classes for the HuRI dataset.

<b>Index</b>	<b>Tissue name</b>
1	Brain – Cerebellar Hemisphere
2	Brain – Cerebellum
3	Cells – Cultured fibroblasts
4	Cells – EBV-transformed lymphocytes
5	Muscle – Skeletal
6	Ovary
7	Testis
8	Thyroid
9	Whole Blood

**Table S3.** Index mapping for HuRI tissues.

Index	Tissue name
1	Adipose – Subcutaneous
2	Adipose – Visceral (Omentum)
3	Adrenal Gland
4	Artery – Aorta
5	Artery – Coronary
6	Artery – Tibial
7	Bladder
8	Brain – Amygdala
9	Brain – Anterior cingulate cortex (BA24)
10	Brain – Caudate (basal ganglia)
11	Brain – Cerebellar Hemisphere
12	Brain – Cerebellum
13	Brain – Cortex
14	Brain – Frontal Cortex (BA9)
15	Brain – Hippocampus
16	Brain – Hypothalamus
17	Brain – Nucleus accumbens (basal ganglia)
18	Brain – Putamen (basal ganglia)
19	Brain – Spinal cord (cervical c-1)
20	Brain – Substantia nigra
21	Breast – Mammary Tissue
22	Cells – Cultured fibroblasts
23	Cells – EBV-transformed lymphocytes
24	Cervix – Ectocervix
25	Cervix – Endocervix
26	Colon – Sigmoid
27	Colon – Transverse
28	Esophagus – Gastroesophageal Junction
29	Esophagus – Mucosa
30	Esophagus – Muscularis
31	Fallopian Tube
32	Heart – Atrial Appendage
33	Heart – Left Ventricle
34	Kidney – Cortex
35	Kidney – Medulla
36	Liver
37	Lung
38	Minor Salivary Gland
39	Muscle – Skeletal
40	Nerve – Tibial
41	Ovary
42	Pancreas
43	Pituitary
44	Prostate
45	Skin – Not Sun Exposed (Suprapubic)
46	Skin – Sun Exposed (Lower leg)
47	Small Intestine – Terminal Ileum
48	Spleen
49	Stomach
50	Testis
51	Thyroid
52	Uterus
53	Vagina
54	Whole Blood

**Table S4.** Tabula Muris dataset cell names

1: keratinocyte	2: neuroendocrine cell	3: duct epithelial cell	4: skeletal muscle satellite cell
5: dendritic cell	6: endothelial cell	7: mesenchymal cell	8: basal cell of epidermis
9: luminal epithelial cell	10: stromal cell	11: mesenchymal stem cell	12: immature B cell
13: hematopoietic precursor cell	14: T cell	15: granulocytopoietic cell	16: promonocyte
17: myeloid cell	18: blood cell	19: Fraction a pre-pro B cell	20: kidney capillary endothelial cell
21: natural killer cell	22: macrophage	23: cardiac muscle cell	24: epithelial cell
25: alveolar macrophage	26: basal cell	27: kidney cell	28: B cell
29: leukocyte	30: DN1 thymic pro-T cell	31: immature T cell	32: Langerhans cell
33: granulocyte	34: bladder cell	35: kidney loop of Henle ascending limb	36: monocyte
37: non-classical monocyte	38: type II pneumocyte	39: kidney collecting duct epithelial cell	40: basophil
41: mast cell	42: mesangial cell	43: endothelial cell of hepatic sinusoid	44: lung endothelial cell
45: endocardial cell	46: fibroblast	47: ciliated columnar cell	48: classical monocyte
49: erythroblast	50: proerythroblast	51: early pro-B cell	52: late pro-B cell
53: hepatocyte	54: bladder urothelial cell	55: kidney proximal straight tubule	

**Table S5.** Tabula Muris SHAP gene list (part 1 of 3; first 400 genes).

Fcer1g	Ubb	Cd79a	Cd79b	Cd3g	Bst2	Il1b
Cfh	Cst3	Fxyd5	Tmsb10	Laptm5	Lsp1	Gnas
S100a4	Alox5ap	Ly6c1	Plvap	Ctsl	Irf8	H2_K1
Klf2	Lyz2	Sepp1	Ccl3	Vim	Socs3	Lyz1
Krt14	Ramp2	Ckb	Oaz1	Gm1821	Marcks11	Arpc2
Hbb_b2	Car2	Scgb1a1	Prss34	Ccl9	Defb1	Tyrobp
AW112010	Nkg7	Ifitm1	Tg	H2_D1	Emp3	Hmgb2
Dek	Ly6c2	Coro1a	Slc12a1	Fbln1	Ccl6	Ctsd
S100a8	Krt19	Shisa5	Rps15a_ps6	Clic1	Rps20	B2m
Igj	Crip1	Igfbp7	Ifitm3	Fabp4	Sparcl1	Selk
Jund	Capzb	Krt7	Serp1	Cd52	A130040M12Rik	Ctsb
Myl4	Nppa	Ifitm6	Retnlg	S100a9	x1100001G20Rik	Laptm4a
Tmsb4x	Cxcl15	Sftpb	Sftpc	Ly6a	Atp1b1	Ly6e
Tuba1a	Clec3b	Sod3	Pcolce2	Tnfaip6	Dntt	Ptprcap
Sh3bgrl3	Pck1	Slc34a1	Errf1	Mt2	Btg1	Hspa1a
Meg3	Vcam1	Id3	Ndufa2	x1110003E01Rik	Upk1a	Upk1b
Cfl1	Rpl37	Gadd45b	Zfp36	Jun	Rps6	Postn
Rps16	Dpt	Ppp1r15a	Rpl7	Srsf5	Npc2	Cryab
Pabpc1	Rps26	Atp5k	Cyc1	Tceb2	Sec61g	x2410015M20Rik
Ubl5	Mdh2	Vdac1	Atox1	Aplp2	Cox6c	Lamp1
x1190002H23Rik	Cks2	Ccl7	Cyr61	Aqbp3	Perp	Cd9
Tbca	Mif	Pim3	Eif6	Trim29	Jup	Krt6a
Rab25	Fabp5	Ly6d	Rtn4	Nfkbia	D14Ert449e	Rpl9
Rps10	Eif4a1	Lgals3	x2010001M09Rik	Chchd10	Ndufc2	Psap
Sepw1	Psmb8	Rhoa	Gabarap	Arpc5	Tmed10	Mal
Lum	Csrp1	H3f3b	Cd24a	S100a11	Cotl1	Taldo1
Actb	Rpl37a	Rplp2	Serinc3	Tmem176a	Gdi2	H2_Aa
Btg2	Ccl17	Tmem176b	Atf4	Fosb	Gadd45g	Rnase4
Ptpn18	Rps2	Rps11	Rps17	Atp5b	Rpl8	Rplp1
Rpl18a	Rps8	Sat1	Ndufb10	Chchd2	Ccdc72	Cox8a
Atp5a1	Btf3	Ndufv3	Myl12a	Rnasek	Foxq1	Ivl
Wfdc2	Rplp0	Pdlim1	Rpl19	Sdc1	Igfbp3	Gltscr2
Hspa8	Rpl15	S100a10	Mrfap1	Pkm2	Psmb3	Sfn
Rbm3	Rps5	Txndc17	Cldn5	H2_Ab1	Cd74	H2_Eb1
Cd164	Krt8	H3f3a	Romo1	Hmgn1	Rps28	H2afv
Eif5a	Rpl23	Rps24	Aldh2	Rpl2211	Tomm6	Fos
Arpc1b	Shfm1	Klf9	Cox7a2l	Rpl27	Rpl18	x1500012F01Rik
Atf3	Cct4	Adamts1	Pa2g4	Atp6v0e	Timp3	Rpl32
Rps15	Rpl41	Rps27	Hnrnpk	Ran	Pcbp1	Usmg5
Cnbp	Eif2s2	Map1lc3a	My16	Cyba	Sec11c	Hint1
Anp32e	Cenpa	Eif1	Zfp706	Atp1a1	Bag1	Rpl5
Ifi27l2a	Atp6v0b	Slc38a2	Ier5	Pnrc1	Tpm4	Vtn
Akr1c6	Gnmt	Srp9	Nfe2l2	x2310003F16Rik	Gsr	Hp
S100a1	x1810037I17Rik	Rac2	Brp44	Nr4a1	Egr1	Arf1
Hist1h2bc	Hras1	Sepx1	Apoe	Ifdr1	Prdx5	Umod
Hnrnpf	Rpl4	Rps27a	Use1	Tmed2	Bsg	Tomm7
Uqcrc1	Ctla2a	Gmfg	Gas6	Rpl35a	Pcbp2	Sgk1
Psca	x2700060E02Rik	Rps14	Gnb2l1	Rpl29	Eef2	Lsm4
Junb	Nme2	Rpl11	C3	Igfbp4	Tmem123	Bgn
Myl9	Elane	Ms4a3	Anxa1	Glxr	H2afx	Mki67

**Table S6.** Tabula Muris SHAP gene list (part 2 of 3; next 400 genes).

Park7	Rpl17	Sub1	Ube2i	Erp29	Mcpt8	Icam1
Atp5e	Fxyd3	Rps18	Ndufb9	x3110003A17Rik	Dmkn	Uqcrfs1
Rps25	Ltb	Hnrrnpab	Plac9	Dnaja1	Itm2b	Id1
Rarres2	Csrp2	Mmp3	Calm1	Gnai2	Pfdn5	Sumo2
Atp5j	Cox4i1	Rpsa	Slc25a4	Cct7	Ddx5	Atp5h
Snrpd2	Tagln	Chmp2a	Ndufa4	Ccl5	Nbl1	Rps21
Rpl10	Arpc1a	Rpl10a	Akr1a1	Etfb	Pomp	Srgn
Ft1	Rpl28	Rps27l	Stmn1	Tubb5	H2afy	Hist1h2ae
Ctsg	Top2a	Aes	Rpl21	Rpl3	Reep5	Cct5
Rps4x	Ywhaq	Atp6v1g1	Arl6ip1	Aqp1	Ldhb	Cd36
Cd14	C1qa	C1qb	Ndufa8	Edf1	Hprt	Fkbp1a
Mfap5	Mmp2	Ccl11	Pi16	Col6a1	Ugdh	Dcn
Mt1	Myoc	Smoc2	Pcolce	Cebpd	Serpingle1	Cxcl1
Zfp36l1	Rps29	Tmem134	D8Ert738e	Slc25a5	Smc4	x2410006H16Rik
Hk2	Ahnak	Sdc4	Atp5o	Dynlrb1	Dad1	Aldoa
Hdgf	Uqcrh	Cox6b1	Nme1	Rpl7a	Rps12	Rps7
Polr1d	Cdkn1a	Ywhaz	Rps3	Maff	Ndufb8	Klf6
Rps23	Gnb2	Hspe1	Rpl12	Pgk1	Crlf1	Hist1h1c
Phb2	Arf5	Avp1	Pebp1	Psmb5	Crip2	Ptma
Psmb6	Snrbp	Rpl6	Uba52	Cox6a1	Nap111	Hnrrnpa2b1
Rps3a	Zfand5	Eef1b2	Eif3h	x1110008F13Rik	Vamp8	Xist
H2afj	Tst	Dstn	Dbi	Slc25a3	Pycard	Rnh1
Ppp1r14b	Serb1	x2610528A11Rik	Rpl14	Arf6	Dnajb1	Cstb
Rpl22	Fosl1	Pkp1	Ovol1	Hbegf	Nhp2	Ndufa4l2
Calml3	Them5	Capns2	Gpx2	S100a14	Ptgr1	Lypd3
x2310033E01Rik	Slpi	Spink5	Actg1	Eef1d	Nedd8	Ndufa3
Fau	Ndufb11	Sqstm1	Acta2	Atp5l	Pdia3	Sprint2
Ost4	Rbx1	Ppp1ca	Rps13	Polr21	Actn4	Mgp
Hsp90aa1	Snrpg	Limd2	Pkp3	Srsf3	Slc3a2	Arpp19
Hsp90b1	Sec61b	Glrx3	Rac1	Ccnd3	Ltf	Ngp
Tkt	Gpi1	Chi3l3	Camp	Fcnb	Atpif1	Minos1
Prdx2	Gm11428	Hmox1	Atp5f1	Ccl4	Napsa	Ctss
Alas2	Pglyrp1	Eif3i	Nop10	Clic4	Lgals7	Metap2
Eif3m	Tubb4b	Atp5g3	Gja1	Ezr	Ldha	Hspd1
Gm94	Ube2d3	Uqcrq	Thy1	Tm4sf1	Glul	F3
Snrpe	Anp32b	H2afz	Cltb	Gnb1	Fth1	Lpl
Cyb5	Odc1	Tacstd2	Psma7	Rpl36a	Timp2	Mrpl52
Srsf2	Higd1a	Ndufb5	Tuba4a	Myeov2	Cd8a	Phlda1
Rpl31_ps12	Skp1a	Tmem59	Blvrb	Uqcr10	Psma2	Rps15a
Pcna	Oat	Ncl	Ybx1	Gpx3	x2200002D01Rik	Gsta4
Sparc	Cpe	Fmod	Eif3k	Chad	Prg4	Srsf7
Serpine2	Gcat	Ppp1r2	Rpl39	Cox5a	Tpi1	Rab10
Ndufs6	Uqcr11	Ndufa6	Ucp2	Ndufa13	Pgam1	Id2
Rcan1	Arhgdib	Hnrrnpu	x2810417H13Rik	Krtcap2	Hist1h1e	Rrm2
Timm13	Tspo	Naca	Fam162a	Sfr1	Nrp1	Acsm2
Hpx	Rabac1	Cdo1	Atp6v1f	Acaa1b	Fxyd2	Akr1c21
Hpd	Apoh	Rgn	Serpina1b	Fabp1	Mup2	Ndrg1
Gclc	Col3a1	Dynll1	Hmgb1	Gng5	Ralbp1	Ucma
Comp	Pdzk1ip1	Ndufb7	Calm4	Anxa5	Apoc4	Gm13889
Eif5	Glycam1	Ube2c	Psma3	Rpl24	Rpl38	Eef1g

**Table S7.** Tabula Muris SHAP gene list (part 3 of 3; remaining 288 genes).

Acp5	Rap1b	Hspb8	Col2a1	Il6	Tomm20	Dsp
Malat1	Epsti1	Ccl2	Has1	Neat1	Prelid1	Calr
P4hb	Ppib	Fdps	Mup3	Cxcl14	Cxcl2	x2010107E04Rik
Miox	Cat	Col8a1	Cxcl10	Mgst1	C1qc	Rpl13a
Lcn2	Prtn3	Eif3e	Gas5	Impdh2	Npm1	Tagln2
Hsp90ab1	Tcp1	Procr	Psmb1	Trf	Emp1	x1500015O10Rik
Myl7	Tpm1	Rab11a	Akr1b8	Rpl36	Scgb3a2	Sbp1
Tff2	Ndufa1	Serpib5	Eif3f	Prdx6	Areg	Cldn4
Eln	Tnfrsf12a	Tmem27	Acy3	Aldob	Cyp4b1	Guca2b
Anxa2	Klk1	Tppp3	Psmb2	Calm2	Ttc36	Tcn2
Hilpda	Gstm1	Ttr	Cyp2e1	Scd1	Esd	Sep15
Wfdc15b	Sprrla	x1110032A04Rik	Bpifa1	Mia1	Sftpa1	Fgg
Aldh3a1	Dsg1a	Timp1	Ccl19	Fgb	Sult2b1	Cd63
Rbp4	Fmo5	Sbsn	Snrfp	Cox5b	Scp2	Atp5j2
Cma1	Retnla	Ctnnbip1	Erh	Serpinh1	Fn1	Ywhae
Apoc3	Fga	Cyp3a11	Mup20	Spink3	Mrpl33	Apoa2
Serpina1d	Hn1	Thbs1	Fam25c	Gjb2	Barx2	Krt24
Ube2s	Spp1	Gc	Krtdap	Car3	Gsta3	Ahsg
Serpina1c	Serpina3k	Apoc1	Kdm6b	Dut	Gpx4	Tubb2a
Epcam	Expi	Clu	S100g	Tmem14c	Atp5c1	Col1a2
Sprrlb	Cnfn	Selenbp1	Dapl1	Cst6	Krt13	Krt4
Krt6b	x2310002L13Rik	Ly6g6c	Krt23	Tgm3	Atp5g1	Col1a1
Lmo1	Tesc	Inmt	Psap11	Efhd2	Apod	Calb1
Krt17	Chi3l1	Serpib2	Mfge8	Calca	Reg3g	Selp
Igfbp5	Serpib3a	Elovl4	x2310002J15Rik	Cldn7	Ctsk	Prr9
x2310079G19Rik	Lce3c	Serpina1a	Rn45s	Serpib12	Defb4	Rbp2
Ptx3	Adh7	Gstp1	Sox9	Csn3	Lrrc15	Kap
Atp2a2	Myh6	Ttn	Ada	Lor	Krt76	Slurp1
Darc	Krt36	Acan	Cyt11	Baspl	Krt84	Tchh
Lipf	x3110079O15Rik	G0s2	Bpifb1	Slc14a2	Krt85	Spr2i
Dcpp2	Krt33b	Dcpp3	Krtap3_3	Mfap4	x1600029D21Rik	Car1
Lyg1	Serpina1e	Krtap13_1	Serpib3c	Pf4	Ppbp	Spr3
Krt34	Krt81	Bhmt	Krt31	Dcpp1	Krtap3_1	Krt42
Krtap13	Krtap9_3	Psors1c2	Krt33a	Krt86	Krtap3_2	x2310034C09Rik
Cyp2c69	Hamp	Klk10	Ptms	Cox7a2	Mt4	Pam
Aldh1a1	Capns1	Sod1	Cebpb	Fstl1	Gsn	Ifi205

**Table S8.** Pan Cancer dataset cancer types abbreviation and full name.

Abbreviation	Full Name
LAML	Acute Myeloid Leukemia
ACC	Adrenocortical Cancer
BLCA	Bladder Urothelial Carcinoma
LGG	Brain Lower Grade Glioma
BRCA	Breast Invasive Carcinoma
CESC	Cervical & Endocervical Cancer
CHOL	Cholangiocarcinoma
COAD	Colon Adenocarcinoma
DLBC	Diffuse Large B-cell Lymphoma
ESCA	Esophageal Carcinoma
HNSC	Head & Neck Squamous Cell Carcinoma
KICH	Kidney Chromophobe
KIRC	Kidney Clear Cell Carcinoma
KIRP	Kidney Papillary Cell Carcinoma
LIHC	Liver Hepatocellular Carcinoma
LUAD	Lung Adenocarcinoma
LUSC	Lung Squamous Cell Carcinoma
MESO	Mesothelioma
OV	Ovarian Serous Cystadenocarcinoma
PAAD	Pancreatic Adenocarcinoma
PCPG	Pheochromocytoma & Paraganglioma
PRAD	Prostate Adenocarcinoma
READ	Rectum Adenocarcinoma
SARC	Sarcoma
SKCM	Skin Cutaneous Melanoma
STAD	Stomach Adenocarcinoma
TGCT	Testicular Germ Cell Tumor
THYM	Thymoma
THCA	Thyroid Carcinoma
UCS	Uterine Carcinosarcoma
UCEC	Uterine Corpus Endometrioid Carcinoma
UVM	Uveal Melanoma

**Table S9.** Pan-cancer label key (indices 1–32, in model order).

1	LAML	2	ACC	3	BLCA	4	LGG
5	BRCA	6	CESC	7	CHOL	8	COAD
9	DLBC	10	ESCA	11	HNSC	12	KICH
13	KIRC	14	KIRP	15	LIHC	16	LUAD
17	LUSC	18	MESO	19	OV	20	PAAD
21	PCPG	22	PRAD	23	READ	24	SARC
25	SKCM	26	STAD	27	TGCT	28	THYM
29	THCA	30	UCS	31	UCEC	32	UVM

**Table S10.** Gene list for the pan-cancer SHAP heatmap (part 1 of 2).

CHST4	TRPA1	PRAC	NKX2-3	NOX1	TYR	DLX6	DLX6AS
UGT1A7	KRTDAP	TMPRSS11A	PGC	ISL1	REG4	RSPO3	SCGB2A1
LYPD2	UCA1	CALML3	REG3A	SERPINB4	TSIX	ACTA1	NR0B1
ADAMDEC1	BLK	CD19	TRIM31	LOC100124692	DKK1	XK	NTS
SFTPA1	OSR1	KIAA2022	WISP1	HOXC4	CALB2	GALNT9	HOXA11
PTPN5	C1orf130	CXCL11	CSMD2	TBX1	LGR5	NKX2-5	C1orf168
LIX1	STX19	C1orf161	EMX2OS	LOC440905	NNAT	TH	CHD5
DUSP15	IL1F9	SLURP1	COX6B2	OTX1	SCGB3A2	STK31	B3GNT6
MUC5B	SEMA3A	C20orf114	MMP12	PLUNC	CXCL17	C19orf59	SCEL
LOC100131551	IGFL2	CLEC18C	PRODH2	CCBE1	CLCNKA	ATP6V0A4	LRRTM1
ST6GALNAC5	TMEM61	CXADR	FA2H	ESRRG	HOXC8	HOXC9	HOXD9
AREG	FAM184B	LOC146336	GRAMD2	RASEF	ROR2	LAD1	SHANK2
EN1	HOXD13	MIA	MGC45800	DPF1	TMEM125	ANO9	HAP1
MAPK15	XDH	RSPO4	TP53AIP1	KRT4	SVOPL	MUC13	LCN12
RNF183	MKX	AQP2	DMRT3	LOC440173	ANGPTL1	IGSF10	MAB21L1
DLX1	CACNG4	VTCN1	HMGA2	DLX2	SIX1	EYA4	HAPLN4
KIRREL2	CASQ1	EPYC	SSTR1	FBN3	ZIC5	B3GALT2	GABRG3
COMP	NTNG1	COL11A1	HOXA11AS	AQP9	CCL21	SCTR	C1orf172
GRID1	TMEM35	FOXD3	MLANA	FUT6	NBLA00301	LPPR5	ZNF536
ROPN1B	C2orf54	FOXP2	PDZK1IP1	PLA2G10	LCN2	C6orf222	CYP2B6
MYO1A	RNF186	CCL11	OVOL1	AADAC	CASP14	FABP1	FAM3D
LEMD1	CCL13	HDC	AQP5	PRSS35	GAP43	TNNI2	NEFM
SLC22A6	FAM189A1	PKHD1	ELFN2	PCSK1N	FABP7	ST8SIA6	PDZD3
FCAMR	HAVCR1	SHH	ADCYAP1	ZDHHC8P1	CNTN3	HAS1	MYO3A
PGLYRP3	XIST	EPHX3	KRT80	CSF3	HEPACAM2	LRRC8E	FOXN1
PRSS21	CDHR2	MEP1A	AQP6	CD38	C4orf7	GAL3ST3	AGR3
PADI3	ACTL8	GJB7	HOXC11	HOXA7	RHOD	DARC	WISP3
LRP4	PRKG2	ALK	HCN1	PDIA2	ZG16B	SCGB2A2	SPRR2B
WNT10A	C19orf21	CNGA1	TNFRSF17	COL8A1	FCRLA	C3orf55	FERMT1
PIP5K1B	CLCA4	KCNK1	RIMBP2	HAL	SLCO1B3	AGR2	ITGB6
DACH1	MCHR1	C19orf46	PRKAA2	CES4	TMPRSS3	FOXL2	IL1A
PLA2G2F	CECR2	NTF4	WNT7B	GPR115	SPRR2C	CTSG	EPHA10
HS3ST6	TMSB4Y	OPRK1	FSD1	PPP1R14D	LRRC4C	UGT1A10	TNS4
C3orf72	HOXC13	MEOX1	TMEM171	MT3	SLC38A4	DIRAS2	FBLN1
GREM2	WNK2	VEPH1	CLEC18B	MASP1	CDK5R2	MPPED1	GDPD2
SLC7A3	TCF21	TMEM132D	PCDH8	SLITRK2	CR2	SLC35F3	MOGAT2
PDX1	PHGR1	PRR11	MNX1	GJB3	MUC2	PLA2G4F	TJP3
ALDH3B2	FXYD1	COL4A6	EPN3	ABCA12	ANXA8	MYBPC1	SORCS1
KIAA1755	GALNT13	UNC93A	SLC28A3	CD164L2	FAM178B	ANKRD56	CLUL1
PRSS16	CBLC	PRR15	GGT6	KRT19	ABO	PPP1R1B	NIPAL1
CHST9	SMPDL3B	AKR1C1	CYP4F11	CHRNA4	C8B	ORM2	SERPIN1A
GSG1L	SP5	SGK2	CEACAM7	NAT8L	CLRN3	CDX2	PRSS3
VWA5B2	C1orf106	STYK1	CAPN8	NETO1	ARMC3	PCDHA12	CHST6
KRT7	TRPM3	IL17D	KCNA1	SLC5A1	NALCN	USH1G	LRRN1
MXRA5	TPSAB1	C10orf107	SLC35F1	GSDMC	ODAM	SBSN	DUOXA1
KLK12	EN2	NKAIN1	DLGAP1	PCDH10	C13orf33	PABPC1L2B	CCDC135
LPAR3	GABRB3	KLK7	SLC7A9	TYRP1	IRX4	ATP2B3	HSD17B2
MMP1	CD70	PITX1	CGREF1	SYT7	CMTM5	ITIH5L	IGSF9B
C2	ENPP6	SCN2B	LRFN5	TDRD9	MAT1A	ADARB2	PRIMA1
GPR172B	GJB5	LOC643763	FAM196B	LOC283174	TNNT1	GBP6	GPR109A
KCNH6	TMEM90B	NLGN4Y	NPY6R	PDPN	MAMDC2	POU2F3	UGT1A6
CST1	LOC100190940	FOXA1	PVRL4	SERTAD4	ARHGDIG	MALL	TBX18
OVOL2	KRT78	AKR1B15	RPTN	ASPG	IGFL1	ADAM33	SYT14
TPO	CYP26A1	HOXA13	ARL14	CCL15	DEFB1	ANO5	ENAM
KRT6C	ZIC2	ATP2C2	AGTR1	EGFL6	SH3RF2	SLC44A5	C1orf210
GSTA1	STRA6	CPA4	GPX2	AK5	C1orf95	FAM167A	C5orf46
FOXI1	CNTN1	DRP2	BEST3	SPAG17	HOXA10	SLITRK3	CYP2C9
PIP	HTR1D	ALPP	LOC100130933	BTNL3	DLX3	FAM5B	KRT31
IL20RA	CNGA3	DSCAM	PRR18	A2ML1	WFDC5	MAGEA9B	WNT3A

**Table S11.** Gene list for the pan-cancer SHAP heatmap (part 2 of 2).

IGFBP1	CYP3A4	TCEAL2	CDH16	SLC12A1	ITIH1	KNG1	ACMSD
ERMN	SLC22A11	KCNJ16	PKLR	DMGDH	POU3F3	SLC17A4	FAM151A
SLC2A2	ESYT3	DSG3	TMEM132C	SYT1	MSX2	CD1A	GFRA3
PSORS1C2	TNNC2	LOC286002	MUM1L1	TRIM15	TMEM139	LGI1	MFAP5
CPA6	ST18	TMEM100	CCDC160	LOC723809	TNNI1	SCRG1	VSIG1
CAMK2A	CNTFR	KRT1	CXCL6	BHMT	USP9Y	DDX3Y	PRKY
CAPN13	IGF2AS	UTY	C10orf82	ACTC1	NUDT10	CRABP1	RGS22
CIDEC	DLK1	NMU	SCARA5	AURKB	KRT16	MYO3B	SLC45A2
PRUNE2	TDO2	FGFBP1	MDGA2	ZFY	TAGLN3	BEND4	MSI1
CA9	PKDCC	DLK2	RHCG	ARSF	CA10	CRTAC1	CPEB1
SYTL1	ABCC6P1	SPRR2G	BCL2L14	TMEFF2	MKRN3	ADCY8	FCN1
SPEF1	TSPAN12	HOXB8	TPSB2	C1orf186	CDC20B	TBC1D3G	HTR3A
FLRT3	HPD	GPR37L1	PCDHA13	ENTPD8	PLN	PROM2	C15orf48
TTBK1	SLC4A10	PRLR	WNT2	BIRC7	CYP17A1	INHA	CD161
CXCL13	ACPP	PDZRN4	TUBBP5	CTSL2	KRT15	STC1	DCDC2
CLDN9	PLA2G2D	BAAT	HRG	CACNA1E	GNG4	CPLX3	ISX
TCN1	LOC100131726	EHF	OR51E2	EDIL3	GYLTL1B	CACNA2D1	FGF14
SOX9	FAM133A	SLC26A3	LEP	SLC6A11	STK33	HKDC1	NKX2-2
IL6	MAGEA11	FGA	RIMS1	CPA3	SDR42E1	BTBD17	KRT75
DQX1	LUZP2	GJB6	MAGEA4	C1orf64	GLYATL2	SLC38A11	ANKRD30A
KLHDC7A	LRAT	APOH	CYP2C18	ABCG8	AHSG	SLC6A1	C4BPB
CPB2	CRP	CFHR2	CFHR5	APOA4	PLA2G12B	THPO	UGT2B15
TM4SF4	CD5L	APOC3	HAO1	UPB1	CREB3L3	ALB	SERPINA7
G6PC	PHF21B	PLCXD3	SYT9	PTCHD1	NRSN1	RPRM	CHST8
C11orf87	C13orf30	DAZ1	SERPINA4	ANXA13	GPR128	CADM2	PARM1
PCSK1	KSR2	SIGLEC8	GABBR2	LRRTM4	COL28A1	SRRM4	ADRA1B
TMEM59L	CYP11A1	ENPP3	ST8SIA2	TRDN	CYP4F12	FAT3	ILDR1
ADAM22	TDGF1	PCDHA10	SNORD116-4	TMEM82	USH1C	P2RX6	MGAT5B
PLA2G4D	MAGEA12	MAGEA3	OMG	CPNE6	GAD1	PCDHAC2	ARG1
MYEOV	CHGA	DBH	SCG2	SLC7A14	ACSM5	SLC6A19	CYP4Z2P
TGM5	NPAS3	CNDP1	LOC647309	CA12	FEV	PCSK2	CALY
TMEM145	TMEM151A	GPR39	GDAP1L1	ANKRD30B	C7orf52	KIAA0125	RIMS4
SLC5A8	PKNOX2	GSTT1	HOXB6	GP2	SERPINA6	C6orf218	FAM181A
PEBP4	UGT3A1	A2BP1	TMEM195	PCDHGC4	PCDHGC5	GPR17	CAPSL
SLC6A3	FBXO2	KCNB1	SULT4A1	CDH22	MUCL1	IP6K3	SEZ6
KLK5	BCMO1	CDH20	ELAVL3	SNCG	LOC255167	TIMD4	DAO
HGD	LRRTM3	ACTL6B	SPHKAP	VWA3A	AMBP	SYT3	HAO2
ACSM2A	SLC17A3	DNAI1	FLG	GABRA3	C3orf15	AKR1B10	CACNG7
B4GALNT4	MGAT4C	ADH4	SLC8A3	IGDCC3	ACTN2	UGT1A3	GRIK2
SLC10A1	CLCNKB	MT1A	GFAP	CHIT1	TMEM150B	SERPINA10	CYP4F2
GRM5	EPHB6	SOD3	C6orf174	KCNQ2	ACSM2B	SLC30A10	KLB
NKX2-1	NCRNA00185	STMN4	FAM57B	CAMKV	SLC28A1	GAL3ST1	TNFSF12-TNFSF1
UMOD	DRD2	OLIG2	QRFPR	GPC3	ADH1B	PPP4R4	AF2
WIT1	DPEP1	HPR	DCT	GRIA4	SLC13A1	GATA4	CNTN6
SH3GL3	FAM135B	ACCN4	MMD2	HEPN1	ZFP57	PCDHA1	PIWIL1
CCKBR	SLN	GTSF1	PVALB	GRM4	HSD11B1	SLC5A12	C14orf73
NPR3	DIO1	ABCC6P2	CTAG1B	FIGF	NEB	GC	RNF128
SMYD1	C6orf142	ST8SIA3	UGT2B10	MTTP	AFP	GLYAT	NAT8
THRSP	CYP8B1	MOGAT3	CP	VGF	HEPACAM	PAQR9	ENPP1
PRSS33	HPCAL4	LRRC19	L1TD1	MAGEA1	TFPI2	MYT1L	NXF2
TCL1A	TBX15	CHRN B2	MAGEA2	SULT2A1	FADS6	LOC100271831	CA3
AMDHD1	TKTL1	BICC1	SHD	SLC26A7	FAM131C	LHFPL4	SLC30A2
ZG16	LIPG	RBM24	BTBD16	MYO18B	RHBG	TRPM8	ZNHIT2
HBA1	SCN4A	MAGEC2	DNAH11	LCN10	ADRA2C	CRYM	SCRT1
LOC84856	MGAM	OIT3	C19orf77	EPS8L3	VNN3	MT1H	CYP4A11
INHBE	F7	C10orf108	NR1I2	OGN	KLK3	ASPDH	FGG
S100A14	PDE1A	RIC3	CHL1	CHRDL1	CNTD2	CPE	52/65 KGS7BP
DDX25	MMP13	ATP13A4	THSD7B	GRP	CDSN	ELMOD1	LOC154822
FAM123A	KIAA1045	SLC5A10					WDR49

**Table S12.** Prostate gene dendrogram key (bottom-to-top order).

1: SEMG2	2: RPS27	3: RPS29	4: A1BG	5: APOC1	6: PLG	7: SERPING1
9: C4B	10: TSPAN8	11: ATP5F1A	12: RPL23	13: FTL	14: APCS	15: APOA2
17: FABP1	18: SEMG1	19: RPS18	20: RGS2	21: NDUFA1	22: SEC61G	23: DAPL1
25: RPL7	26: HNRNPA2B1	27: LUM	28: ATP5MF	29: XBP1	30: LMAN2	31: PDCD4
33: PRDX1	34: UBA52	35: NAP1L1	36: RPS26	37: NDUFC2	38: PDIA4	39: EIF3E
41: SSR2	42: IFITM3	43: MYL12A	44: NFKBIA	45: NME2	46: HSPE1	47: ANXA2
49: HEXB	50: PDIA3	51: NDUFB10	52: TFF3	53: H4C4	54: MT1E	55: ATP6V0C
57: MZT2A	58: SELENOW	59: MDK	60: OLFM4	61: SERHL2	62: CCN1	63: DHCR24
65: F3	66: HLA_DMB	67: CFL1	68: HSP90AB1	69: ST6GAL1	70: RARRES2	71: SELENOH
73: RPL37A	74: RPL19	75: TLE5	76: COMT	77: APOA1	78: STEAP2	79: TIMP1
81: PRRC2A	82: FGG	83: C1S	84: CALM2	85: RPL35	86: RPS27A	87: CPE
89: TF	90: RPL39	91: HSD17B6	92: RPS10	93: FADS2	94: S100A10	95: DYNLL1
97: RPS3	98: COX6C	99: RPL27	100: ACTG1	101: GADD45G	102: SLC25A39	103: CHCHD2
105: LDHA	106: AMBP	107: RHOC	108: BCAP31	109: RBP4	110: REXO2	111: SRSF5
113: KRT19	114: RPL18A	115: PEX10	116: RPS16	117: HP	118: SRSF2	119: FABP5
121: HNRNPA1	122: LTBP4	123: S100A8	124: FMOD	125: RPS17	126: SLPI	127: MT1F
129: ATP6V0E2	130: CD74	131: LUC7L2	132: ATP5PD	133: CUTA	134: ACTN4	135: HLA_B
137: MIEN1	138: RPL18	139: PIEZO1	140: NCAPD3	141: SELENOP	142: GFUS	143: SERP1
145: A2M	146: APOD	147: TSTD1	148: DLK1	149: NDUFA13	150: NPC2	151: TPD52
153: PLPP1	154: DDT	155: DUS1L	156: NDUFA2	157: APOC3	158: EIF4A2	159: SUMO2
161: HINT1	162: ITIH4	163: TTR	164: CFB	165: RPL14	166: EEF1A1	167: ATP5MG
169: COX7B	170: HMGN2	171: RPS23	172: WFDC2	173: KRT18	174: NOP53	175: KLK3
177: TUBB	178: NEFH	179: RAN	180: YBX1	181: BANF1	182: SKP1	183: NDUFB9
185: COX8A	186: EIF4A1	187: NRP1	188: C4A	189: EIF3C	190: PPDFF	191: NUPR1
193: CSRP1	194: HMGB2	195: TMEM256	196: EIF3H	197: P4HB	198: DES	199: MYL9
201: MYH11	202: PRKDC	203: CST2	204: ANPEP	205: STEAP4	206: ACTA2	207: BCAM
209: LTF	210: C1orf43	211: TMSB10	212: ATP5MC1	213: CST3	214: PTGDS	215: FLNA
217: SERPINA1	218: RPL7A	219: SRRM2	220: AMD1	221: NPDC1	222: TPM1	223: EIF3L
225: KRT8	226: CD81	227: KRT5	228: ARPC3	229: RPLP0	230: TAF1	231: ANG
233: ITIH1	234: AHSG	235: RPL29	236: VTN	237: FGA	238: IGLL5	239: FGL1
241: RPS12	242: MYL12B	243: RPL32	244: UBB	245: TOMM7	246: FXYD3	247: MICOS10
249: ORM2	250: SRP14	251: ATP6V1G1	252: UBC	253: PSMD2	254: RPL4	255: RPS6
257: TMEM59	258: APEX1	259: CSNK1E	260: COL4A2	261: PKM	262: BGN	263: SON
265: MESP1	266: COL9A2	267: SLC25A6	268: RPL23A	269: VIM	270: ANXA5	271: C1QB
273: HSPA5	274: TMED3	275: ST13	276: ZG16B	277: CAPNS1	278: CTSZ	279: RPS19
281: SERPINH1	282: CD9	283: PLXND1	284: RPL10	285: RPL24	286: PARK7	287: ATP5MC2
289: ATP6V0E1	290: RPL13A	291: RPS14	292: GPX1	293: SLC44A4	294: EIF5A	295: STMN1
297: TPT1	298: PRSS8	299: TSPAN1	300: DSTN	301: ATF4	302: THY1	

## A Clustering Metrics

To assess the quality of the embedding spaces learned by each model, we used a set of standard clustering metrics that compare the learned clusters to the known biological labels. The adjusted Rand index (ARI) measures how often pairs of samples are grouped together or separated in the same way as the ground-truth labels, while correcting for random agreement. Normalized mutual information (NMI) quantifies how much information about the true labels is preserved by the clustering, and is insensitive to the absolute number of clusters.

We further report homogeneity and completeness to characterize the purity of clusters from two complementary perspectives. Homogeneity measures whether each predicted cluster contains samples from only a single true class, whereas completeness measures whether all samples from a given class are assigned to the same cluster. The V-measure is the harmonic mean of homogeneity and completeness, and it summarizes the trade-off between these two properties.

Finally, we compute the silhouette coefficient directly in the embedding space. This metric compares the average distance of each sample to points in the same cluster versus points in the nearest different cluster. High silhouette scores indicate compact, well-separated clusters in the underlying feature space, independent of the label information. Taken together, these metrics allow us to evaluate both label alignment (ARI, NMI, homogeneity, completeness, V-measure) and geometric separation (silhouette) of the learned embeddings.

Let  $\mathcal{U} = \{U_1, \dots, U_R\}$  be the ground-truth partition of  $N$  samples and  $\mathcal{V} = \{V_1, \dots, V_C\}$  be the clustering obtained from an embedding (e.g. Graph2Image or a GNN). Define the contingency table

$$n_{ij} = |U_i \cap V_j|, \quad a_i = \sum_j n_{ij}, \quad b_j = \sum_i n_{ij}, \quad N = \sum_{i,j} n_{ij},$$

and denote the binomial coefficient by  $\binom{n}{2} = \frac{n(n-1)}{2}$ .

### Adjusted Rand Index (ARI)

The Rand index measures the agreement between two partitions in terms of pairwise co-assignment. The adjusted Rand index corrects this quantity for chance:

$$\text{ARI}(\mathcal{U}, \mathcal{V}) = \frac{\sum_{i,j} \binom{n_{ij}}{2} - \frac{\left(\sum_i \binom{a_i}{2}\right) \left(\sum_j \binom{b_j}{2}\right)}{\binom{N}{2}}}{\frac{1}{2} \left[ \sum_i \binom{a_i}{2} + \sum_j \binom{b_j}{2} \right] - \frac{\left(\sum_i \binom{a_i}{2}\right) \left(\sum_j \binom{b_j}{2}\right)}{\binom{N}{2}}}. \quad (9)$$

ARI = 1 indicates perfect agreement and ARI  $\approx 0$  corresponds to random labeling (negative values are possible when the agreement is worse than random).

### Normalized Mutual Information (NMI)

The mutual information between  $\mathcal{U}$  and  $\mathcal{V}$  is

$$I(\mathcal{U}; \mathcal{V}) = \sum_{i=1}^R \sum_{j=1}^C \frac{n_{ij}}{N} \log \left( \frac{n_{ij}/N}{(a_i/N)(b_j/N)} \right), \quad (10)$$

with entropies

$$H(\mathcal{U}) = - \sum_{i=1}^R \frac{a_i}{N} \log \frac{a_i}{N}, \quad H(\mathcal{V}) = - \sum_{j=1}^C \frac{b_j}{N} \log \frac{b_j}{N}. \quad (11)$$

We use the arithmetic-mean normalized mutual information (as in `sklearn`):

$$\text{NMI}(\mathcal{U}, \mathcal{V}) = \frac{2I(\mathcal{U}; \mathcal{V})}{H(\mathcal{U}) + H(\mathcal{V})}. \quad (12)$$

NMI ranges in  $[0, 1]$ , where 1 indicates that the two partitions carry identical label information.

## Homogeneity and Completeness

Homogeneity measures whether each estimated cluster contains only members of a single ground-truth class. It is defined via the conditional entropy of  $\mathcal{U}$  given  $\mathcal{V}$ :

$$H(\mathcal{U} | \mathcal{V}) = - \sum_{j=1}^C \sum_{i=1}^R \frac{n_{ij}}{N} \log \frac{n_{ij}}{b_j}, \quad (13)$$

and

$$\text{homogeneity} = 1 - \frac{H(\mathcal{U} | \mathcal{V})}{H(\mathcal{U})}. \quad (14)$$

Completeness measures whether all members of a given class are assigned to the same cluster. Using the conditional entropy of  $\mathcal{V}$  given  $\mathcal{U}$ ,

$$H(\mathcal{V} | \mathcal{U}) = - \sum_{i=1}^R \sum_{j=1}^C \frac{n_{ij}}{N} \log \frac{n_{ij}}{a_i}, \quad (15)$$

we define

$$\text{completeness} = 1 - \frac{H(\mathcal{V} | \mathcal{U})}{H(\mathcal{V})}. \quad (16)$$

Both scores lie in  $[0, 1]$ ; higher values indicate purer and more coherent clusters, respectively.

## V-measure

The V-measure is the harmonic mean of homogeneity  $h$  and completeness  $c$ :

$$\text{V-measure} = \frac{2hc}{h+c}, \quad (17)$$

with V-measure = 1 if and only if both  $h = 1$  and  $c = 1$ .

## Silhouette Coefficient

Let  $d(\mathbf{x}_p, \mathbf{x}_q)$  be a distance between embedded points (e.g. Euclidean distance). For a point  $i$  assigned to the cluster  $C(i)$ , define

$$a(i) = \frac{1}{|C(i)|-1} \sum_{\substack{j \in C(i) \\ j \neq i}} d(\mathbf{x}_i, \mathbf{x}_j), \quad (18)$$

$$b(i) = \min_{C' \neq C(i)} \frac{1}{|C'|} \sum_{j \in C'} d(\mathbf{x}_i, \mathbf{x}_j), \quad (19)$$

where  $a(i)$  is the average distance to points in the same cluster and  $b(i)$  is the minimum average distance to points in any other cluster. The silhouette of point  $i$  is

$$s(i) = \frac{b(i) - a(i)}{\max\{a(i), b(i)\}}, \quad (20)$$

and the overall silhouette coefficient is the mean over all points:

$$\text{Silhouette} = \frac{1}{N} \sum_{i=1}^N s(i). \quad (21)$$

The silhouette lies in  $[-1, 1]$ , with values close to 1 indicating well-separated, compact clusters.

**Table S13.** Clustering quality of embedding spaces learned by Graph2Image (CNN-based) and graph neural networks (GNNs) on five datasets. Higher is better for all metrics.

Dataset	Model	ARI	NMI	Homogeneity	Completeness	V-measure	Silhouette
PP-Pathways	GCN	0.032	0.137	0.146	0.129	0.137	0.115
	GAT	0.020	0.104	0.111	0.097	0.104	0.094
	GIN	0.009	0.037	0.022	0.113	0.037	<b>0.850</b>
	Graph2Image	<b>0.176</b>	<b>0.497</b>	<b>0.527</b>	<b>0.470</b>	<b>0.497</b>	0.054
HuRI	GCN	0.092	0.184	0.176	0.193	0.184	0.145
	GAT	0.016	0.035	0.035	0.035	0.035	0.156
	GIN	0.035	0.018	0.015	0.022	0.018	<b>0.523</b>
	Graph2Image	<b>0.281</b>	<b>0.475</b>	<b>0.480</b>	<b>0.469</b>	<b>0.475</b>	0.140
Pan	GCN	0.642	0.805	0.810	0.800	0.805	0.617
	GAT	0.626	0.768	0.776	0.760	0.768	0.425
	GIN	0.394	0.684	0.655	0.717	0.684	0.586
	Graph2Image	<b>0.867</b>	<b>0.926</b>	<b>0.935</b>	<b>0.917</b>	<b>0.926</b>	0.504
TM	GCN	<b>0.635</b>	0.775	0.811	0.741	0.775	0.364
	GAT	<b>0.634</b>	0.786	0.812	0.761	0.786	0.320
	GIN	0.455	0.613	0.547	0.698	0.613	0.435
	Graph2Image	0.519	<b>0.828</b>	<b>0.911</b>	<b>0.752</b>	<b>0.824</b>	0.270
Prostate Cancer	GCN	0.057	0.075	0.044	0.251	0.075	0.733
	GAT	-0.008	0.000	0.000	0.000	0.000	0.483
	GIN	0.051	0.050	0.053	0.047	0.050	0.614
	Graph2Image	<b>0.669</b>	<b>0.606</b>	<b>0.561</b>	<b>0.655</b>	<b>0.604</b>	<b>0.926</b>

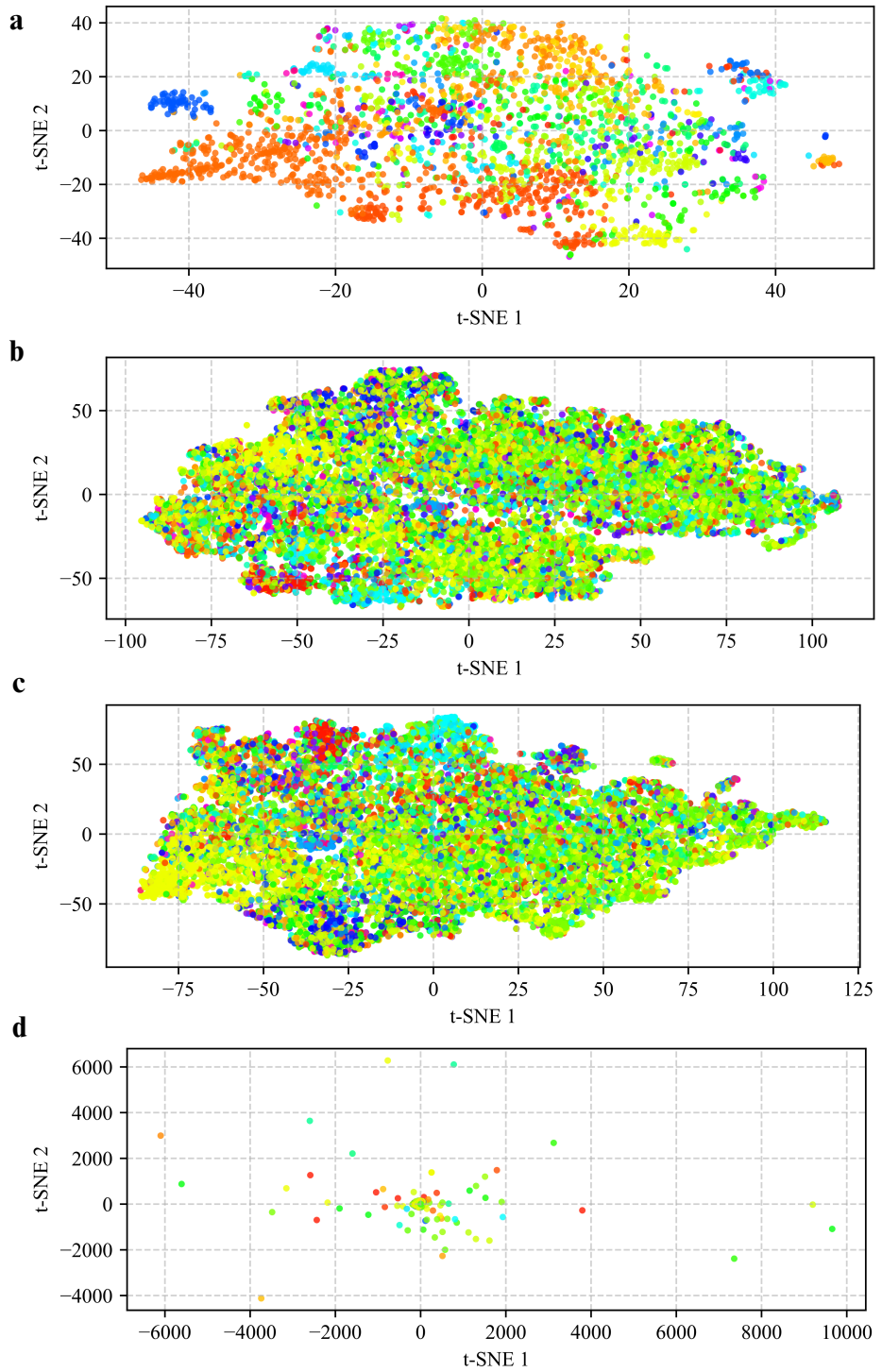


**Figure S21.** t-SNE visualisation of embedding spaces learned by Graph2Image and graph neural network (GNN) baselines on the PP-Pathways interactome. Two-dimensional t-SNE projections of (a) Graph2Image (CNN-based) embedding, (b) GAT, (c) GCN and (d) GIN, coloured by GTEx tissue label. Graph2Image yields a markedly more structured and compact embedding space with discernible grouping of related tissues, whereas GNN baselines produce diffuse or overlapping manifolds with weaker separation. These differences indicate that Graph2Image captures tissue-specific expression patterns more coherently in the PP-Pathway protein–protein interaction network. The legend is provided in Figure S22.



**Figure S22.** Legend for t-SNE visualisation of embedding spaces learned by Graph2Image and graph neural network for the PP-Pathways dataset.

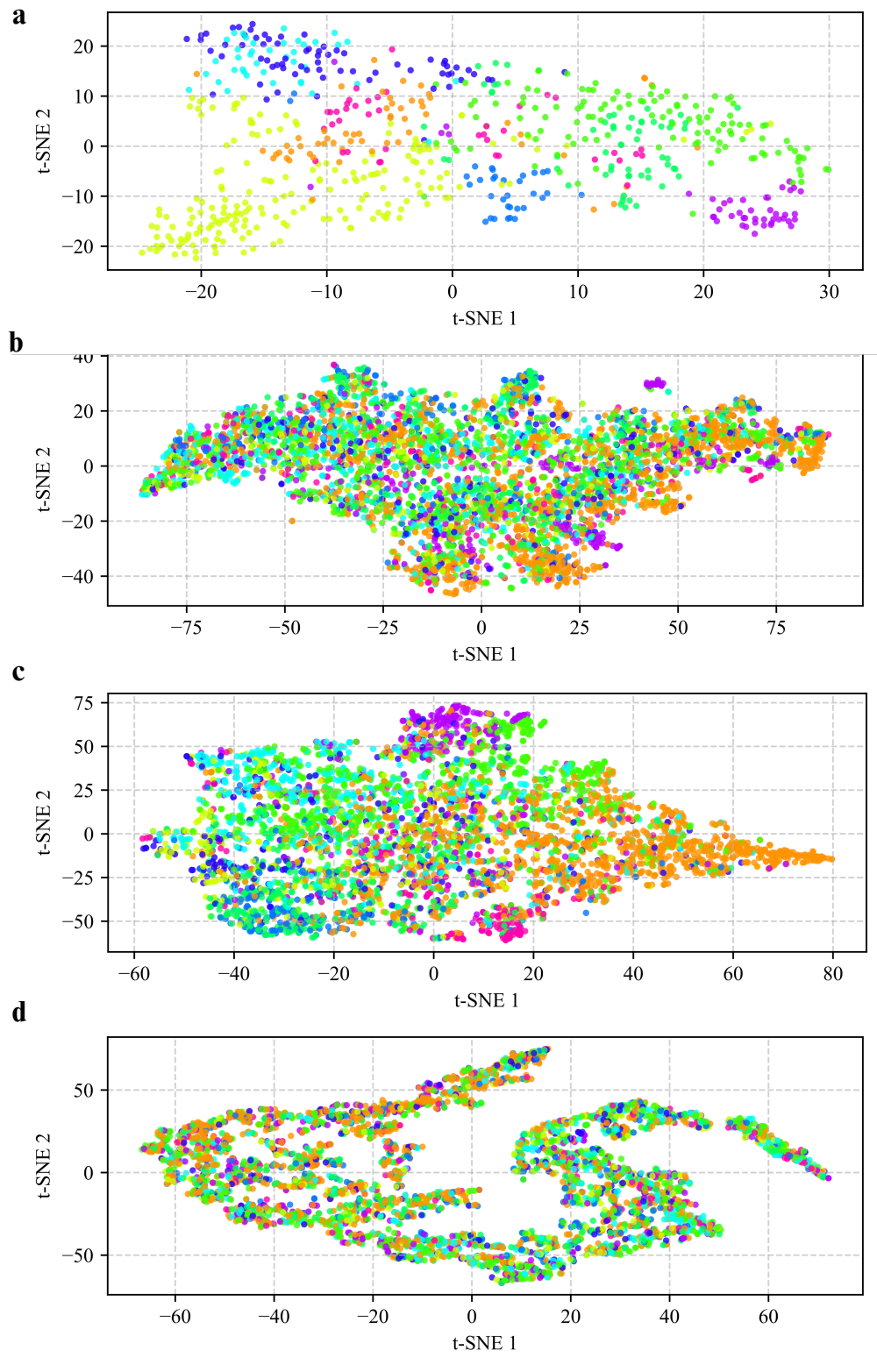


**Figure S23.** t-SNE visualisation of embedding spaces learned by Graph2Image and graph neural network (GNN) baselines on the HuRI tissue dataset. Two-dimensional t-SNE projections of (a) Graph2Image (CNN-based) embedding, (b) GAT, (c) GCN and (d) GIN, coloured by GTEx tissue label. Graph2Image produces a substantially more organised and tissue-coherent embedding space, with smoother manifolds and clearer separation between major GTEx tissue groups. In contrast, the GNN baselines generate diffuse, intermingled, or fragmented structures, suggesting weaker preservation of tissue-specific transcriptomic signatures within the HuRI protein–protein network. The legend is provided in Figure S23.

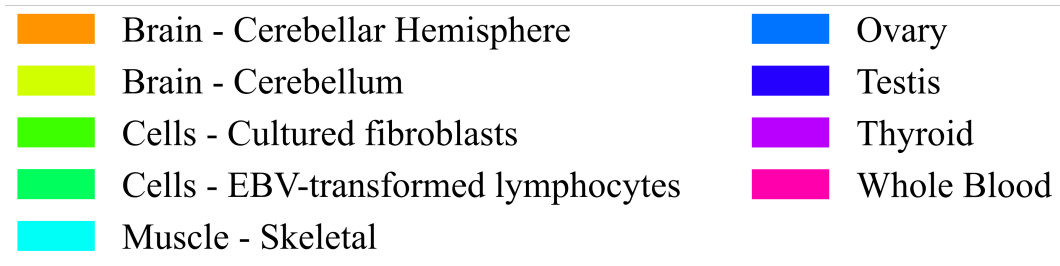


**Figure S24.** Legend for t-SNE visualisation of embedding spaces learned by Graph2Image and graph neural network for the HuRI dataset.

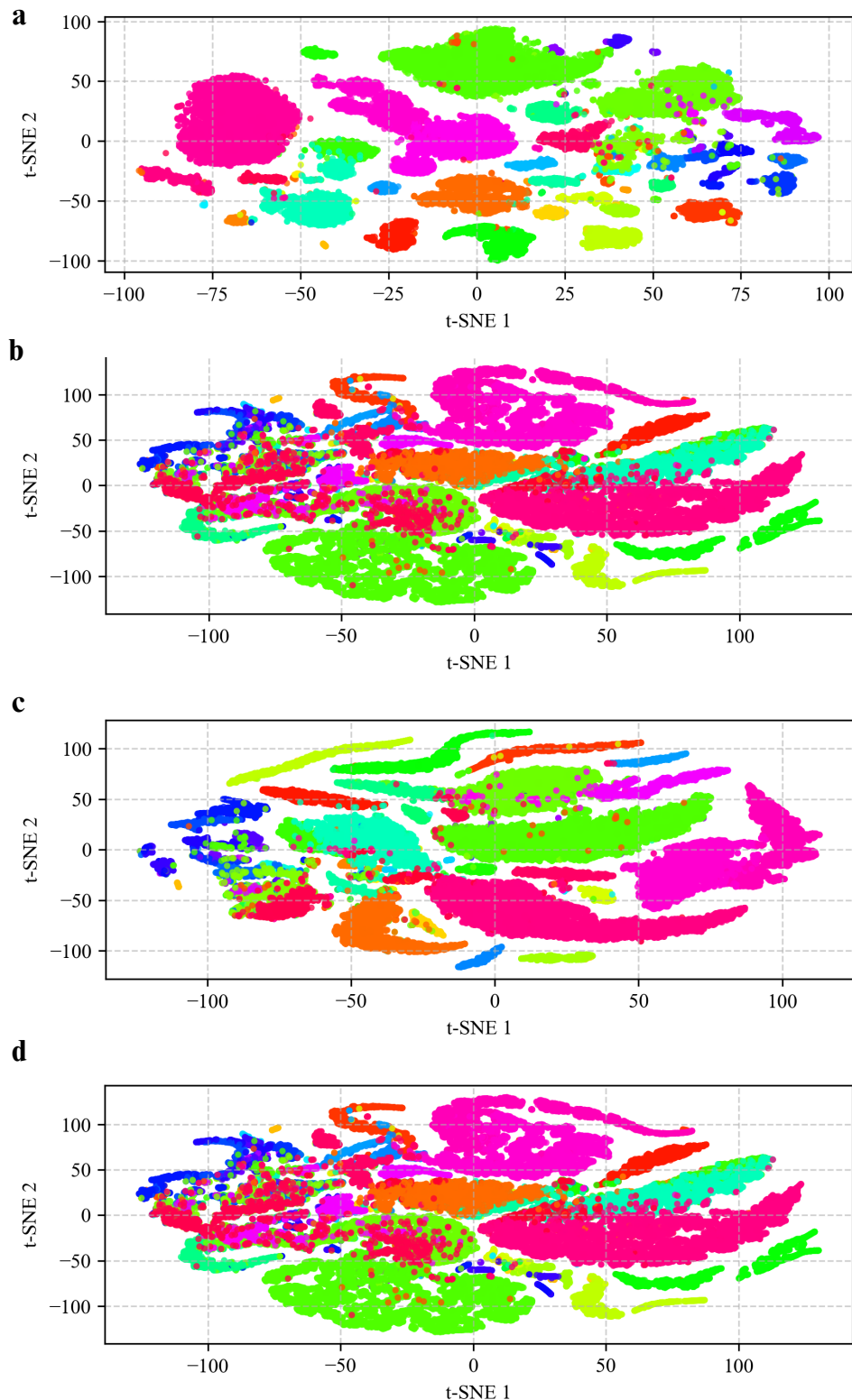


**Figure S25.** t-SNE visualisation of embedding spaces learned by Graph2Image and graph neural network (GNN) baselines on the TM single-cell dataset. Two-dimensional t-SNE projections of (a) Graph2Image (CNN-based) embedding, (b) GAT, (c) GCN and (d) GIN, coloured by annotated cell type. Graph2Image produces compact, well-separated clusters that closely follow the biological annotations, whereas GNN embeddings often form elongated or partially overlapping manifolds, indicating a less label-consistent feature space. The legend is in Figure S26

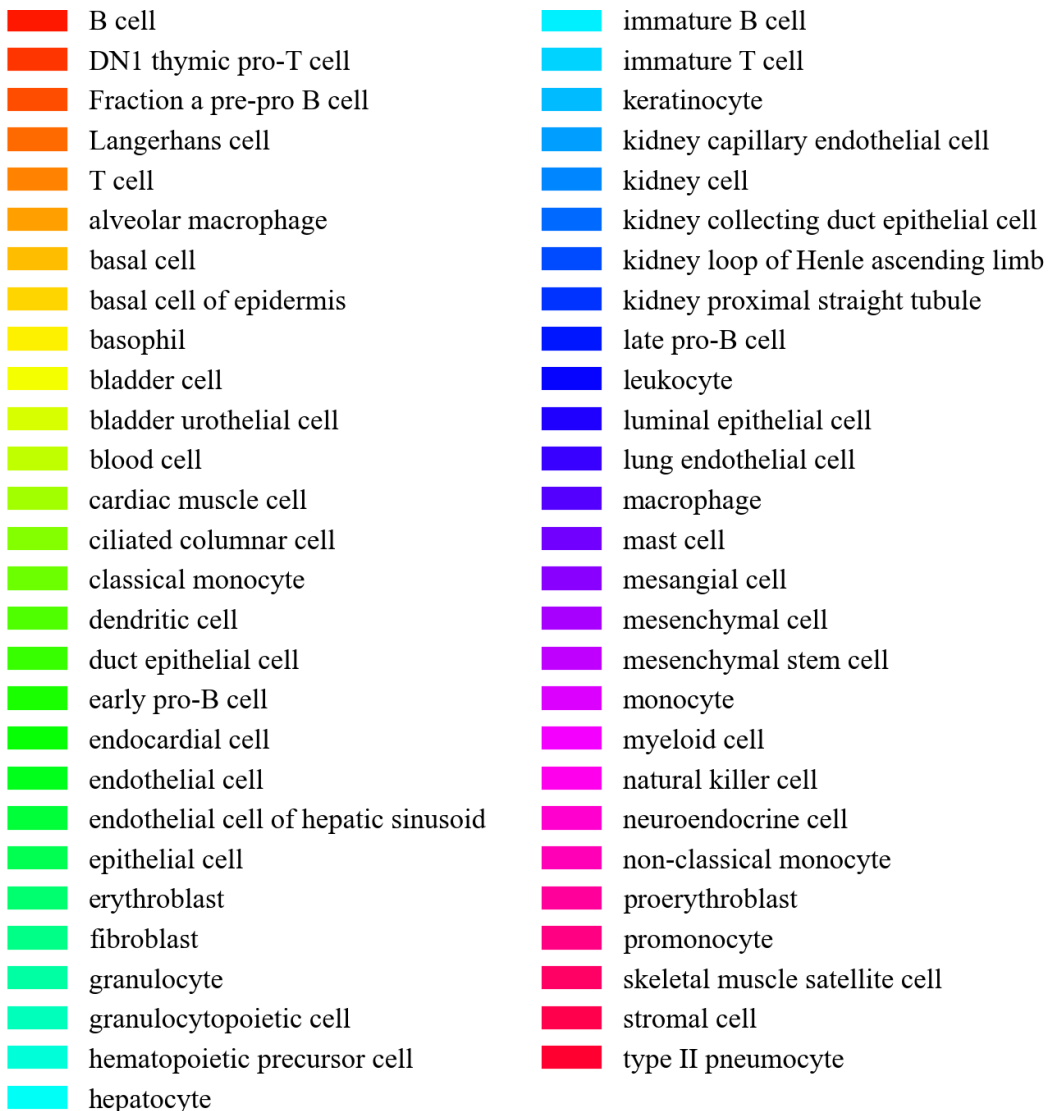


**Figure S26.** Legend for t-SNE visualisation of embedding spaces learned by Graph2Image and graph neural network for the TM dataset.

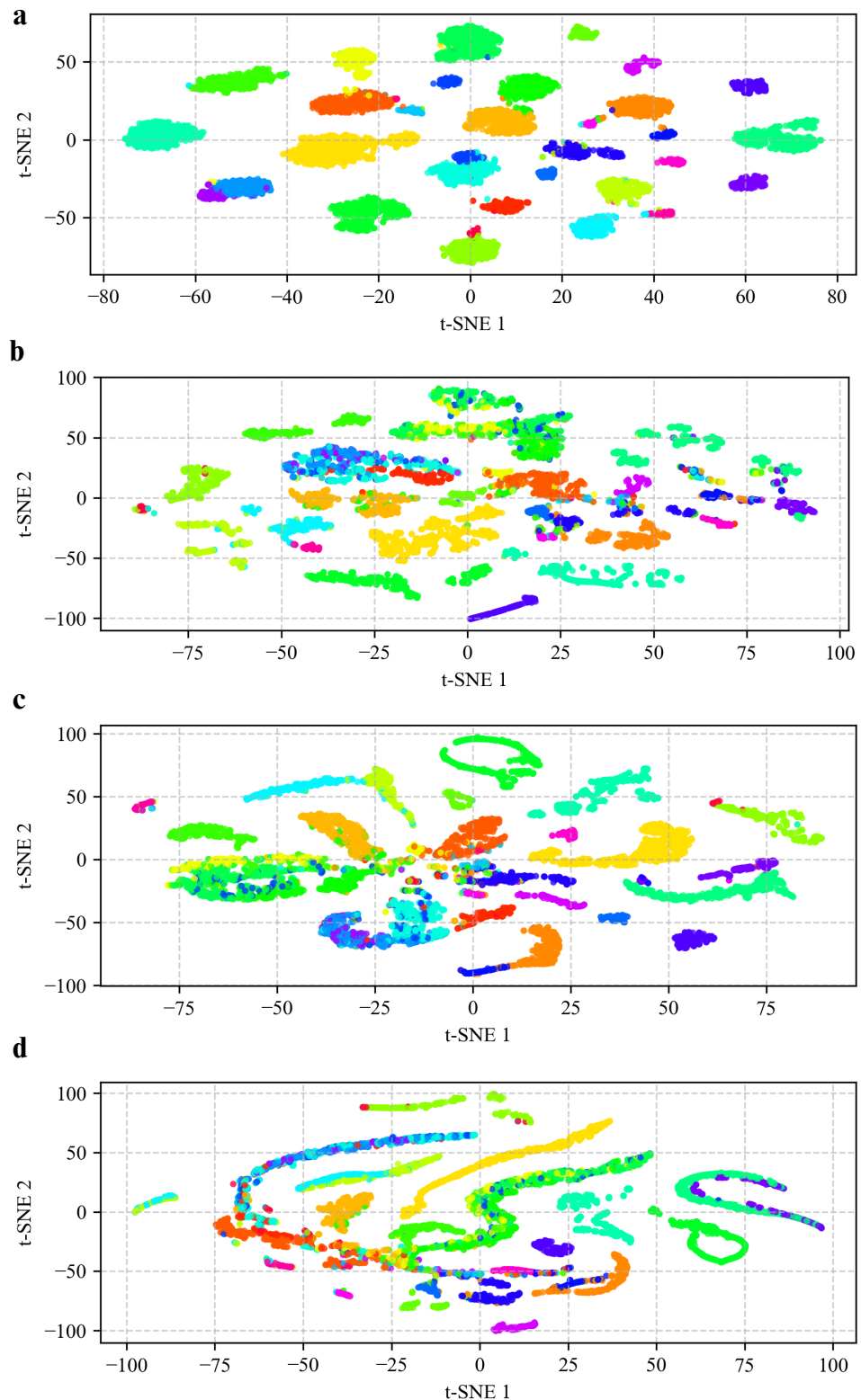


**Figure S27.** t-SNE visualisation of embedding spaces learned by Graph2Image and graph neural network (GNN) baselines on the Pan-cancer (Pan) cohort. Two-dimensional t-SNE projections of (a) Graph2Image (CNN-based) embedding, (b) GAT, (c) GCN and (d) GIN, coloured by tumour type. Graph2Image yields discrete, well-separated clusters for individual cancer types, while GNN embeddings exhibit stretched or interwoven manifolds with substantial overlap between tumours, consistent with reduced clustering purity. The legend is in Figure S28

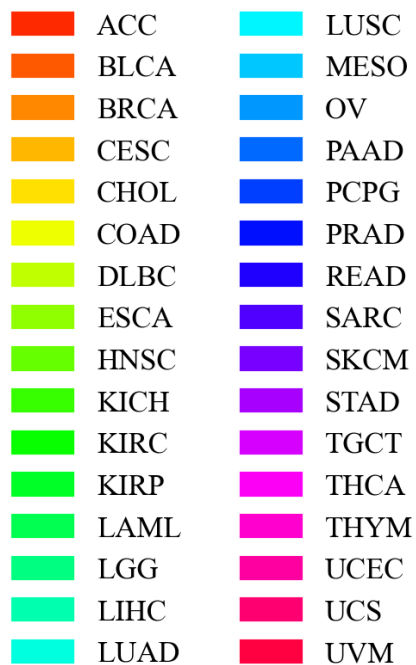


**Figure S28.** Legend for t-SNE visualisation of embedding spaces learned by Graph2Image and graph neural network for the Pan Cancer dataset.

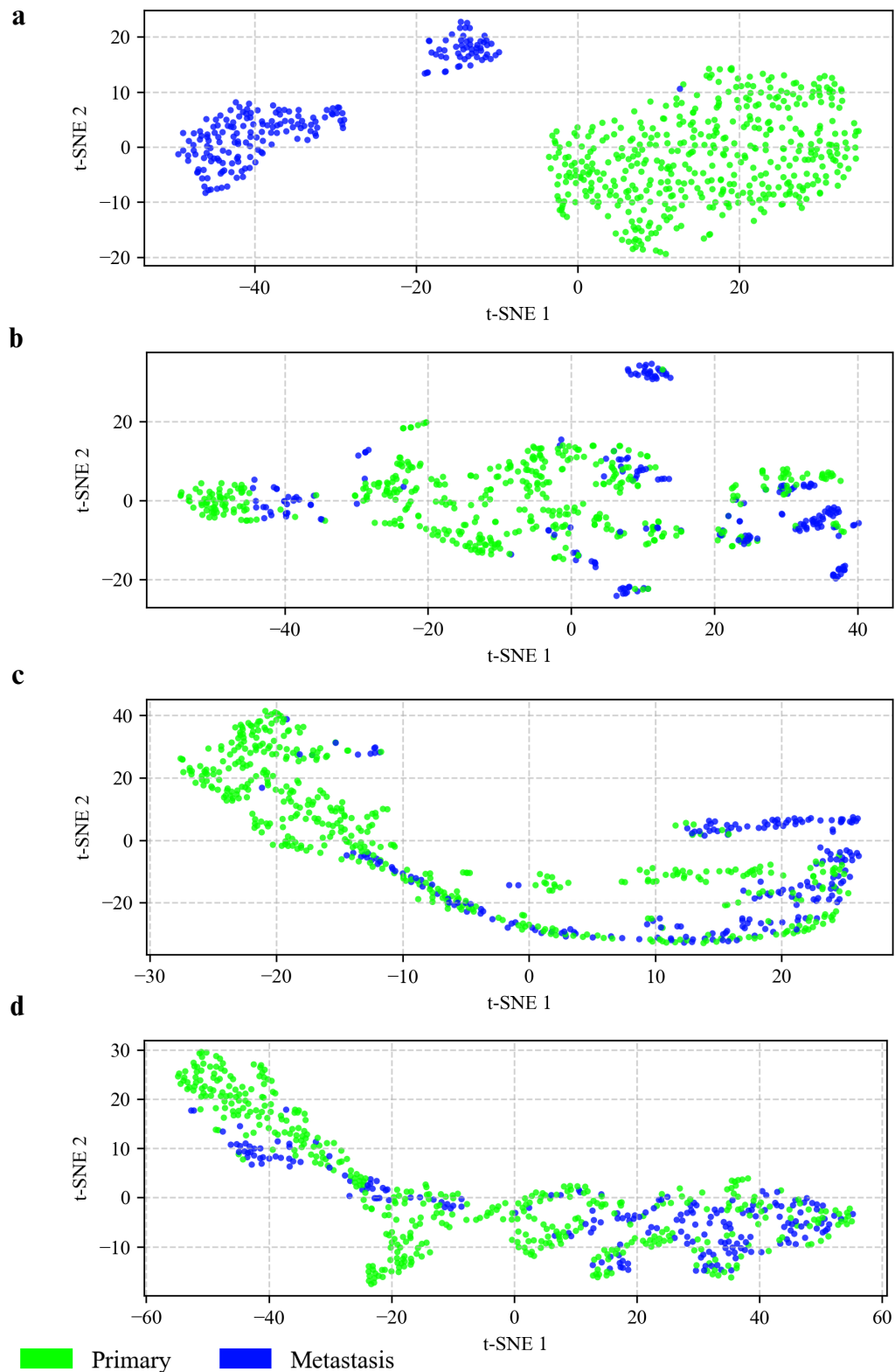


**Figure S29.** t-SNE visualisation of embedding spaces learned by Graph2Image and graph neural network (GNN) baselines on the Prostate Cancer primary–metastasis cohort. Two-dimensional t-SNE projections of (a) Graph2Image (CNN-based) embedding, (b) GAT, (c) GCN and (d) GIN, coloured by clinical label (Primary vs. Metastasis). Graph2Image clearly separates primary tumours and metastatic lesions into disjoint clusters, whereas GNN embeddings show substantial mixing of the two labels and fragmented manifolds, indicating weaker alignment between the learned feature space and clinical outcomes.